Spring 1-1-2014

The Seasonality of the Loop Current

Cody Alan Hall
University of Colorado Boulder, codyalanhall@gmail.com

THE SEASONALITY OF THE LOOP CURRENT

by

CODY ALAN HALL

B.S., University of Colorado, 2009

M.S., University of Colorado, 2011

A thesis submitted to the

Faculty of the Graduate School of the

University of Colorado in partial fulfillment

of the requirement for the degree of

Doctor of Philosophy

Department of Aerospace Engineering Sciences

2014

This thesis entitled:
The Seasonality of the Loop Current
written by Cody Alan Hall
has been approved for the Department of Aerospace Engineering Sciences

(Robert R. Leben)

(George H. Born)

(William J. Emery)

(Karl E. Gustafson)

(Benjamin D. Hamlington)

(Jeffrey P. Thayer)

Date_____

The final copy of this thesis has been examined by the signatories, and we
Find that both the content and the form meet acceptable presentation standards
Of scholarly work in the above mentioned discipline.

Hall, Cody Alan (Ph.D., Aerospace Engineering Sciences)

The Seasonality of the Loop Current

Thesis directed by Research Professor Robert R. Leben

A total of 20 Loop Current eddy separation event dates were derived from Seasat and ERS-1 satellite altimetry, Coastal Zone Color Scanner chlorophyll-a images, Advanced Very High Resolution Radiometer sea surface temperature images, Horizon Marine, Inc. EddyWatch™ reports, and Climatology and Simulation of Eddies Eddy Joint Industry Project Gulf Eddy Model analyses spanning mid-1978 – 1992. There were many inconsistencies between the new "pre-altimetry" reanalysis dates derived from mostly non-altimeter data and dates published in past literature based on earlier versions of the pre-altimetry record. The reanalysis dates were derived from a larger compilation of data types and, consequently, were not as affected by intermittent and seasonal data outages common with past records. Therefore, the reanalysis dates are likely more accurate. About 30 Loop Current eddy separation dates were derived from altimetry data spanning 1993 – 2012. The pre-altimetry and altimetry *reanalysis* dates along with similar altimetry dates published in other literature exhibit statistically significant seasonality. Eddy separation events are more likely in the months March, August, and September, and less likely in December. Reanalysis event dates were objectively divided into "spring" and "fall" seasons using a k-means clustering algorithm. The estimated spring and fall season centers are March 2nd and August 23rd, respectively, with seasonal boundaries on May 22nd and December 3rd. The altimetry data suggest that Loop Current intrusion/retreat is dominantly an annual process. Loop Current metrics such as maximum northern boundary latitude and area are relatively high from January through about July and low in September and October. February metrics are statistically different than metrics in either October or November or both. This annual process is primarily driven by and dynamically linked to geostrophic currents seaward of the Campeche Bank shelf break forced by Kelvin waves generated on the southeast United States and Gulf of Mexico continental shelves. The dominant mode of an altimetric coastal empirical orthogonal function analysis of the southeast United States and Gulf of Mexico continental shelves indicates that the primary coastal signal covaries with the Loop Current and accounts for 65% and 85% of the annual variance in Loop Current northern latitude and area, respectively.

ACKNOWLEDGEMENTS

I thank Cortis Cooper, George Forristall, and CASE/JIP for encouraging the initial studies of the Loop Current in 2009 and Michael Shannon for processing data so critical to this research. I appreciate the financial support provided by Bureau of Ocean Energy Management contract number M08PC2043 to Leidos Corporation, which made the research I performed for this dissertation possible. I thank Bob Leben, the Colorado Center for Astrodynamics Research, and God for seeing me through and giving me the opportunity to earn my diploma. Lastly, I thank my wife Kelsey who supports me with whatever I decide to do and has eagerly awaited with me our lives after my school. And I thank my little girl Laramie for being that pleasant distraction through all the hard days, though she may never remember that I was working on this dissertation for the first two years of her life.

CONTENTS

TABLES

Table

FIGURES

Figure

CHAPTER I

INTRODUCTION

The Loop Current (LC) is the primary oceanic mesoscale feature of the eastern Gulf of Mexico (GOM) beginning in the Yucatan Channel, turning anticyclonically, and then flowing out through the Florida Straits. Its extent varies greatly and changes frequently. At times, the LC can intrude farther west than 92°W and farther north than 27°N once beyond the Campeche Bank. At others, the LC may retreat farther south than 24.5°N and remain entirely east of the Campeche Bank. The LC often assumes less extreme configurations but typically follows a basic pattern of variation. 1) The LC intrudes north and sometimes west into the GOM from a (somewhat) retreated position. 2) The LC reaches an unstable configuration, which ultimately results in separation of a Loop Current eddy (LCE), a cohesive piece of anticyclonic circulation, from the LC. 3) The LC retreats rapidly south as a result of volume loss and begins to intrude again from there. Once completely separated from the LC, LCEs usually propagate away from the LC into the western GOM and do not interact with the LC again. However, there is often a time period during separation that a LCE will detach from and reattach to the LC multiple times causing peripheral losses of LC and LCE mass. Oceanographers hypothesized decades ago that this LC cycle is regular and predictable according to season. The earliest studies of LC intrusion and LCE separation were based on upper-ocean temperature sections along shipboard survey cruise transects (Leipper, 1970; Maul 1977; Behringer et al, 1977). Most of these observations were made during the spring, summer, and fall. In those studies an annual cycle of LC intrusion was hypothesized based on early observations of an annual cycle in the Yucatan Current inflow, with maximum northward current velocities in May and June and minimum in October and November (Cochrane, 1965). Leipper (1970) proposed an annual cycle of LC intrusion in the spring followed by either a deeply intruded LC or a separated LCE and retreated LC in the fall. That study was based on in situ data collected primarily during 1965 and 1966. Maul (1977) found a similar cycle in 1972 and 1973, and was able to track the frontal position of the LC over 14 months. This past-proposed annual cycle is similar to the mean annual cycle described later in

this dissertation. Unfortunately, as time went on, the notion of a LC annual cycle was cast into doubt.

In situ measurements taken in the 1970's suggested that if the LC did exhibit a mean annual cycle, there were significant deviations due to highly variable LCE separation events. Behringer et al. (1977) noted separation periods (period between two LCE separations) ranging from as short as 8 months to as long as 17 months, which demonstrated that LCE separation did not consistently happen every 12 months. Legeckis (1976) reported the first wintertime deep intrusion and eddy separation determined from direct observations during the winter of 1974 and 1975. Satellite remote sensing also contributed to the changing viewpoint in the GOM. Maul (1975) demonstrated that satellite imagery could be used to detect the western margin of the LC during winter. Then shortly after, Molinari et al. (1977) used both satellite and in situ data to identify intrusions of the LC north of 26°N from 1974 through 1977 and LCE separation events in both winter and spring. Since earlier observational data were limited during the wintertime, it was not clear whether winter intrusions occurred before the mid-1970s. However, these authors provided the first evidence that eddy separation could occur in any season.

In the early 1980s, Hurlburt and Thompson (1980) challenged the hypothesis that the LC sheds eddies in response to annual variations in the inflow through the Yucatan Channel by numerical simulation of LC intrusion and eddy shedding. The authors found that a modeled LC could penetrate into the GOM, bend westward, and shed realistic LCEs at a quasi-annual natural shedding frequency with *steady* inflow. The quasi-annual (natural) period was about 290 days. This was the first numerical model of the GOM that was integrated to statistical equilibrium and simulated the basic repetitive features of the LC eddy separation cycle (Hurlburt and Thomson, 1982). The authors also found that realistic time-varying upper layer inflow could significantly influence eddy separation. Nevertheless, the eddy shedding was dominated by the natural period, not the period of forcing in the model experiments. At about the same time, Sturges and Evans (1983) speculated that there were wind-forced annual variations in the north-south position of the LC. With hydrographic data, the authors found an annual signal in the northernmost position of

the LC. However, given that the observed annual signal amplitude was only 1.7 degrees (Sturges and Evans, 1983), it seemed plausible that the annual signal detected in observations was just an artifact of undersampling and averaging over the observed highly variable LC eddy shedding cycles.

As time went on, developing technologies in operational satellite monitoring allowed tracking of the LC and LCEs in new ways and at higher temporal and spatial resolutions. These developments included the first successful tests of satellite-tracked drifting buoys, satellite altimetry, and satellite ocean color radiometry. Satellite-tracked drifting ocean buoys were developed using data collected by the NASA Nimbus-6 satellite, which carried a Tracking and Data Relay experiment that was used to determine drifting buoy positions using Doppler tracking (Kirwan et al., 1976). Nimbus-6 was launched on June 12, 1975 and operated until March 29, 1983. This research mission led to the development of the Argos system, which collects, processes, and disseminates data from fixed and mobile platforms using polar orbiting NOAA satellites to the present day. Kirwan et al. (1984) documented the first use of satellite-based tracking of drifting buoys within a LCE. Three satellite-tracked drifting buoys were air-deployed in November 1980 by the NOAA Data Buoy Center into a fall-separated LCE and allowed satellite tracking of the LCE into the western Gulf well into spring 1981. In the late 1970s the first ocean altimetry and ocean color satellite missions were flown by NASA. Seasat, launched in June 27, 1978, carried the first satellite altimeter capable of measuring ocean surface topography with the accuracy required to resolve ocean mesoscale signals (Cheney et al., 1983). The first instrument devoted to the measurement of ocean color, the Coastal Zone Color Scanner (CZCS), was launched aboard the Nimbus-7 satellite on October 24, 1978. These were experimental missions, and little of these data made it into the general user community for use in operational ocean monitoring or into the published LCE separation censuses (Fred Vukovich, personal communication). In fact, none of these technologies had as great of an impact on LC perception as satellite sea surface temperature (SST).

Satellite SST radiometry advancements in the 1970s and 1980s revolutionized oceanographic measurement. Imagery taken by the very high-resolution radiometer (VHRR) instruments onboard polar orbiting NOAA satellites became available at sufficient resolution and precision to make synoptic-scale and mesoscale SST frontal analyses of the GOM (Vukovich et al., 1979). These analyses were typically based only on a few clear sky SST images and could not be made throughout the year. In May, when the warm seasonal ocean surface mixed layer developed in the GOM, imagery sometimes required intense enhancement to make fronts visible, and the accuracy of some frontal features was questionable. From June through October, the LC and LCE fronts were often indistinguishable (Fred Vukovich, personal communication; Vukovich, 2012). AVHRR instruments eventually superseded VHRRs and provided more consistent and usable imagery. Infrared images from the geostationary operational environmental satellite (GOES) were also used for LC monitoring. Imagery processed by the NOAA Miami Satellite Field Services Station was geo-registered using photographic techniques and used to map daily locations of the LC front (Maul et al., 1978). The 24-hour coverage provided by GOES geostationary sampling reduced data outages associated with cloud cover, and oceanic fronts in the Gulf Stream system could be mapped about half of the days (Maul et al., 1984). Even so, GOES data still had limited use when the GOM surface waters reached a near-uniform temperature in the summer. LC cycle and LCE separation period analyses published in the late 1980s and early 1990s relied heavily on SST imagery (Vukovich, 1988; Maul and Vukovich, 1993; Sturges, 1992; 1993; 1994) and were therefore biased by sampling inconsistencies caused by SST data outages due to seasonal heating of the mixed layer. Pairing SST imagery with other data types such as satellite altimetry and ocean color would have allowed better observation of the LC intrusion and eddy separation cycle. For instance, Müller-Karger et al. (1991) demonstrated that the combined use of CZCS ocean color and AVHRR SST images permits year-round monitoring of LC intrusion and eddy separation. Unfortunately, altimetry and ocean color data were in limited use at the time. As a result most publications from the 1980s and

1990s showed little or no evidence of a true annual LC cycle, tacitly, confirming the model studies of Hurlburt and Thompson.

Late in the 1990s and into the new century, satellite altimetric and industry monitoring made tracking of the LC and its associated eddies fully operational. Multi-satellite altimetric mapping of the ocean mesoscale afforded by the ERS-1 and TOPEX/Poseidon missions and then later follow-on missions provided the satellite sampling required to achieve continuous LC monitoring, which has remained to the present day. The hypothesis of seasonality in the LC and in LCE separation has only been revitalized recently since the GOM altimetric record has become long enough to resolve the seasonal signal independent of the earlier historical and published records. Alvera-Azcárate et al. (2009) found 21 LCEs in a survey of altimetry data from October 1992 into February 2006, 12 of which separated in the months of July, August, or September. In the same year, Forristall Ocean Engineering (2009a; 2009b) discussed a statistical model with built-in seasonality for the LC and eddies, though the results were proprietary. Leben and Hall (2010) presented monthly-binned histograms of pre-altimetry and CCAR altimetry LCE separation dates as additional observational evidence that separation timing has a seasonal preference. Chang and Oey (2012) similarly suggested that pre-altimetry separation dates in past literature combined with altimetry dates derived from an AVISO product also support seasonality. Then finally, Lindo-Atichati et al. (2013) calculated the mean annual cycle of the northern boundary of the LC with error bars and concluded that northern penetration at some times of the year is statistically different than at other times.

This dissertation revisits and presents more rigorous statistical evidence supporting the idea of LC seasonality using a variety of different observational data types, both in situ and satellite-derived. In the following chapters, the LC observational period from 1978 through 2012 is split into two separate records for ease and clarity of analysis: the "pre-altimetry" record from 1978 through 1992 and the altimetry record from 1993 through 2012. The "pre-altimetry" record is a combination of satellite SST and CZCS data, industry analyses and in situ data, and a small amount of satellite altimetry data since little altimetry data were collected prior to 1993. The

altimetry record is comprised only of satellite altimetry. Since the characteristics of both records are markedly different, seasonal analyses will be handled differently for each record. In the context of this dissertation, the word "seasonality" refers to a LC event or configuration characteristic of a certain season or time of year. Note that the terms "annual" and "seasonal" are not used synonymously. However, an annual cycle is necessarily seasonal. Chapter II describes the reanalysis of the pre-altimetric LC record; comparisons of the pre-altimetry reanalysis with previously published separation dates follow in Chapter III; the 20-year long altimetric LC record is described in Chapter IV. Note that Chapters II, III, and IV are mainly "data" chapters, though Chapter IV also illustrates the effects of different data processing methods on derived LC and LCE metrics used later to demonstrate seasonality. In Chapter V I present a detailed statistical analysis of LC (LCE) seasonality; in Chapter VI I present an investigation of the dynamics contributing to LC seasonality and identify the dominant signal contributing to the observed LC annual cycle. Chapter VII provides conclusions, and Chapter VIII discusses future work.

CHAPTER II

REANALYSIS OF THE "PRE-ALTIMETRIC" LOOP CURRENT RECORD

Continuous multi-satellite altimetric sampling required for accurate mapping of the SSH associated with mesoscale circulation in the GOM and monitoring of the LC and LCEs did not exist prior to late 1992. For this "pre-altimetric" time period, NASA Seasat altimetry, NASA Coastal Zone Color Scanner (CZCS) ocean color, Advanced Very High Resolution Radiometer (AVHRR) sea surface temperature (SST), and ESA ERS-1 satellite altimetry data were used to perform a reanalysis of the separation events observed before 1993. LC and LCE positions determined from Horizon Marine Inc. (HMI) EddyWatch^{TM} reports and the Climatology and Simulation of Eddies Eddy Joint Industry Project (CASE/EJIP) Gulf Eddy Model (GEM) analyses were used to supplement the satellite observations. Table 1 lists the dates of all 20 identified separation events in the record along with HMI industry names (if available), separation periods, and retreat latitudes. The separation period is the length of time between separation events. Retreat latitude is the maximum latitude of the LC immediately following separation of a LCE (Leben, 2005). The mean separation period in Table 1 is 270.5 days, and the mean retreat latitude is 25.7°.

Table 1. Loop Current eddy separation events with the corresponding retreat latitudes and separation periods from July 1978 through December 1992.

No.	Year-Letter	Industry Name	Separation Date	Best Available Imagery/Chart	Retreat Latitude (°N)	Separation Period (days)
1	1978	-	15 Jul 1978	SSH[a,b]	24.7[c]	-
2	1980a	-	18 Feb 1980	Chlorophyll-a[a]	26.2	583
3	1980b	-	16 May 1980	Chlorophyll-a[a]	26.4	88
4	1980c	-	04 Aug 1980	Chlorophyll-a[a]	26.0	80
5	1981a	-	04 Jul 1981	Chlorophyll-a	25.5	334
6	1981b	-	24 Oct 1981	Chlorophyll-a[a]	26.4	112
7	1982	-	21 Aug 1982	Chlorophyll-a[a]	26.0	301
8	1983a	-	08 Mar 1983	SST[a]	26.8	199
9	1983b	-	23 Aug 1983	SST[a,b]	26.0	168
10	1984a	-	25 Jan 1984	SST[a]	25.8	155
11	1984b	Arnold	28 Aug 1984	Chlorophyll-a	25.6	216
12	1985	Fast	18 Jul 1985	EddyWatch™ [a,b]	25.6	324
13	1986a	Hot Core	18 Jan 1986	SST	25.7	184
14	1986b	Instant	12 Sep 1986	SST[a,b]	25.7	237
15	1987	Kathleen	08 Nov 1987	SST	25.6	422
16	1988	Murphy	25 Apr 1988	SST[a]	24.5	169
17	1989	Nelson	01 Sep 1989	EddyWatch™ [a,b]	25.3	494
18	1990	Quiet	14 Sep 1990	EddyWatch™ [a,b]	25.0	378
19	1991	Triton	01 Nov 1991	SST[a]	26.4	413
20	1992	Unchained	10 Aug 1992	SSH	24.7[c]	283
				Mean	25.7	270.5

[a] GEM P&C analyses (Evans-Hamilton, 1992) were available to verify separation date estimate.
[b] GEM P&C analyses determined separation date estimate.
[c] An offset of 0.36° must be added to SSH-derived retreat latitudes to make them consistent with values estimated from satellite SST and ocean color frontal analyses. The offset was applied when calculating the mean.

Seasat along-track altimetry data are available from July through October 1978 from the NASA Ocean Altimeter Pathfinder program (Koblinsky et al., 1998). The data were processed as non-repeat track data similar to the processing described for ERS-1 geodetic mission data in Leben et al. (2002). CZCS data are available from November 1978 into June 1986 from the NASA Goddard Space Flight Center Ocean Color webpage. Level-3 chlorophyll-a concentration 8-day composite images at 4-km resolution were used in the reanalysis (downloaded 10 Jul 2008). AVHRR data, described in Casey et al. (2010), are available from the National Ocean Data Center (NODC) Pathfinder SST Program website. The Sept. 1981 through Jan. 1985 Pathfinder SST data were first released on April 13, 2009 by NODC, which was the first time that this data had been available in the nearly 20-year history of the AVHRR Pathfinder program. The weekly-averaged 4-km resolution SST product Version 5.1 was used (downloaded in May and September of 2009 and February of 2010). Example images of the LC from CZCS ocean color and AVHRR SST images in the time period before industry analyses from HMI became available in 1984 are shown in Fig. 1. The CZCS ocean color image shown is an 8-day composite from Aug. 13–20, 1979. The AVHRR SST image is the weekly mean from Feb. 19-25, 1982. Along-track 35-day repeat ERS-1 altimeter data from the multidisciplinary mission phase (Apr. 14, 1992 through Dec. 21, 1993) were extracted from the Radar Altimeter Database System (RADS) and were processed as described in Leben et al. (2002).

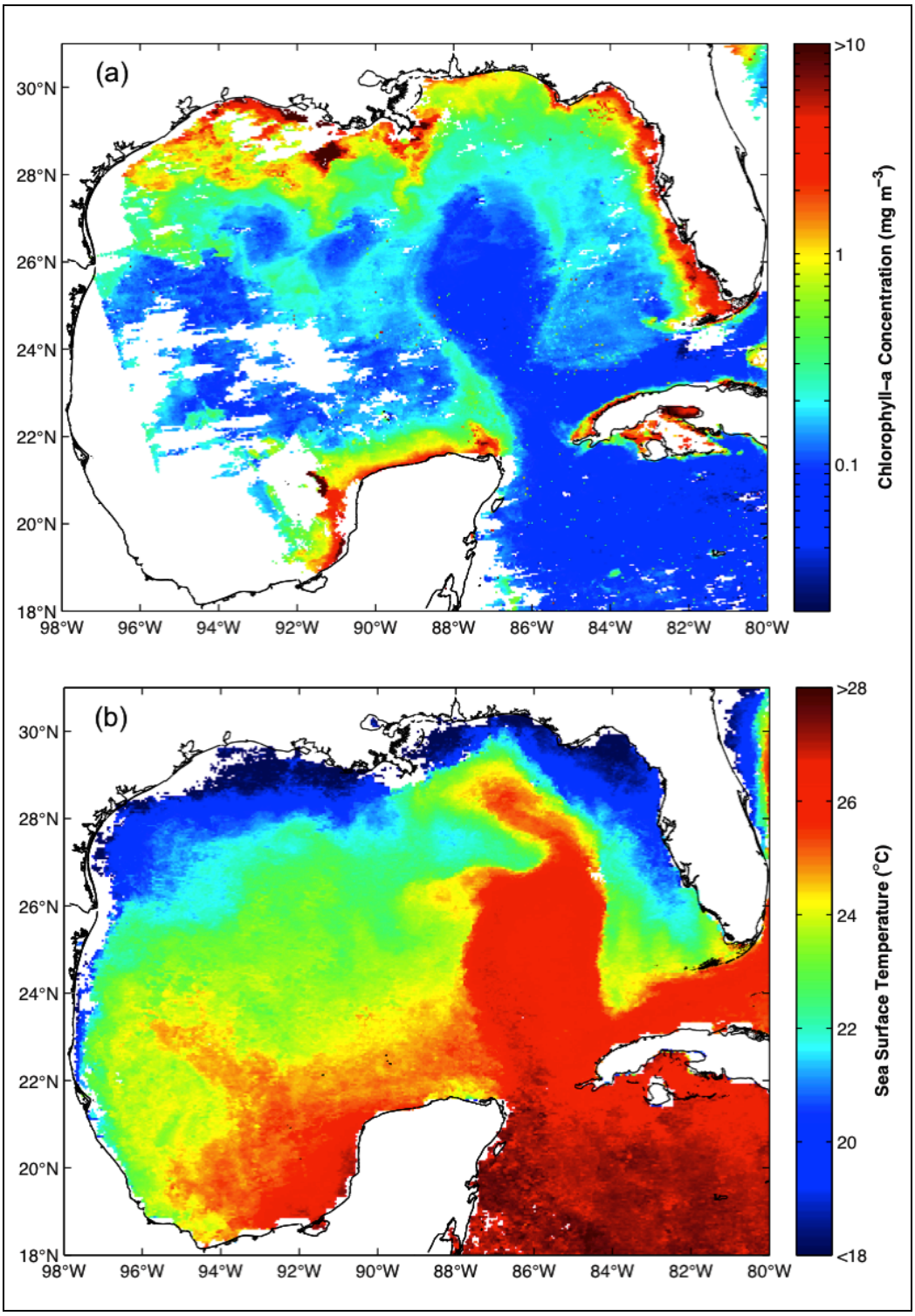

Fig. 1. Examples of the "best" Loop Current images from (a) Coastal Zone Color Scanner ocean color and (b) Advanced Very High Resolution Radiometer sea surface temperature data in the time period before EddyWatch™ analyses from Horizon Marine, Inc. became available in 1984 (see Fig. 2). The Coastal Zone Color Scanner ocean color image is an 8-day composite from August 13–20, 1979. The Advanced Very High Resolution Radiometer sea surface temperature image is a weekly mean from February 19–25, 1982.

The HMI EddyWatch™ reports used in the reanalysis to help identify both LCE separation and LC retreat latitude span the time period from Sep. 4, 1984 through Dec. 31, 1992. There were several time spans, however, when the weekly reports were not published: Aug. 30, 1986 through Feb. 5, 1987, Aug. 15, 1987 through Mar. 30, 1988, Nov. 12, 1988 through Feb. 16, 1989, and Apr. 1, 1992 through Sept. 3, 1992. The available reports were digitized from hardcopies provided by CASE/EJIP for the development of a statistical LC hindcast model (Forristall et al., 2010). An EddyWatch™ chart is shown in Fig. 2 for LCE "Hot Core", which separated from the LC on Jan. 18, 1986. This is a representative example of the type of information provided in the EddyWatch™ reports used in the reanalysis to help identify both LCE separation and LC retreat latitude. Although the GEOSAT Geodetic and Exact Repeat Missions spanned many of the time periods when EddyWatch™ reports were not published, GEOSAT altimeter data were not used in the reanalysis because of the frequent data outages in the eastern GOM during this mission. These outages occurred whenever the passive gravity gradient stabilization system allowed the satellite to point too far off nadir, which caused the on-board tracker to fail to regain lock on the returned waveform over the ocean when coming off of land (Sandwell and McAdoo, 1988). Continuous satellite altimetry from 35-day repeat sampling during the ERS-1 multidisciplinary phase, however, provided altimetric coverage during the time period in 1992 when EddyWatch™ reports were not published. This was fortunate because no ocean color data were available during the summer of 1992 for monitoring of the LC and LCE fronts.

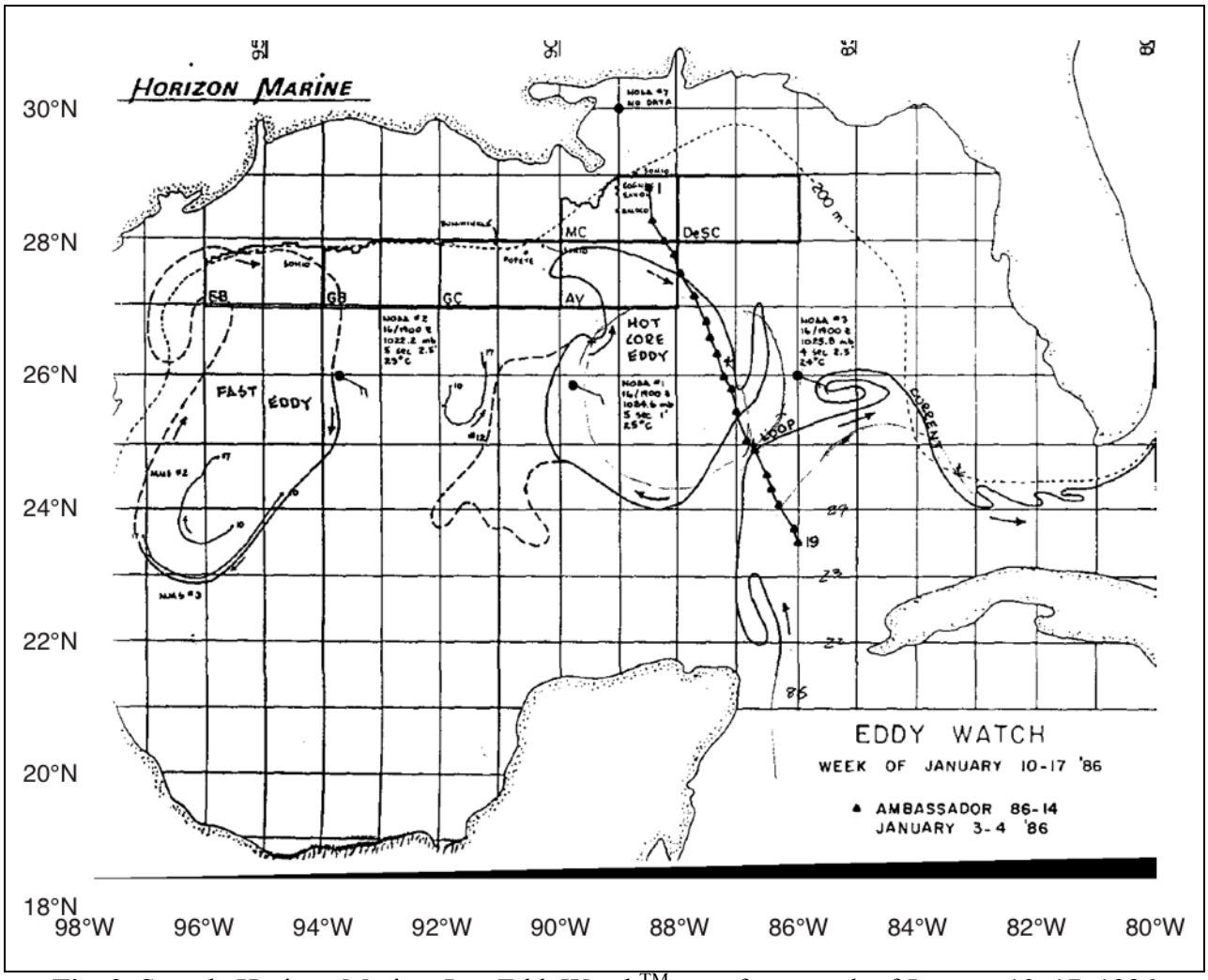

Fig. 2. Sample Horizon Marine, Inc. EddyWatch™ map from week of January 10–17, 1986 showing frontal analysis of "Fast Eddy", "Hot Core Eddy", and the Loop Current based on satellite-tracked drifters, sea surface temperature data, and a ship of opportunity transect.

GEM Path and Configuration (P&C) daily analyses (Evans-Hamilton, 1992) were also used in the reanalysis to help determine LCE separation dates. GEM is both a model and a database and is an industry tool for hindcasting LC and LCE currents. GOM metocean engineering designs rely on hindcasts from the model to provide a database for the location of the LC and LCEs and the associated currents (Forristall et al., 2010). GEM is based on the feature model developed by Glenn et al. (1990) to support exploratory deepwater drilling operations off the U.S. east coast. The model fits an idealized isolated translating elliptic paraboloid with a swirl velocity to surface fronts in satellite imagery, to expendable

bathythermograph survey data, and to satellite-tracked drifting buoy data associated with anticyclonic recirculation embedded within the intruding LC and LCEs both separating from and propagating away from the LC. GEM eddy tracks from 1966 to 1991, including the initial portion of the track that corresponds to LCEs embedded in the intruding LC, are shown in Fig. 3 of Kantha et al. (2005).

Animations of the combined time series of color maps, SST images, HMI EddyWatch™ charts, and GEM P&C analyses were used to identify LCE separation and LC retreat following separation, supplemented with satellite altimetry maps from Seasat and ERS-1. CZCS images and GEM analyses showed conclusively that there were no LCE separation events from November 1978 through 1979. The one separation event reported in the literature during this time period, in April 1979 (Vukovich, 1988; Vukovich, 2012), was identified in the reanalysis as an eddy detachment, not an eddy separation. The first LCE separation event was identified using GEM analyses and occurred in July 1978, after which a continuous record of separation events and LC retreats following separation could be derived using the satellite and industry data records. Remarkably, the short-lived NASA Seasat Mission sampled this initial LCE separation event with both the Seasat satellite altimeter and the Seasat Synthetic-Aperture Radar (SAR) (Fu and Holt, 1982), confirming the industry observations of a separation event. Figure 3 shows GOM SSH calculated by adding Seasat SSH anomaly to the CUPOM model mean (Nowlin et al., 2001; see Chapter IV). The Seasat altimetric sampling allows an estimate of the LC retreat latitude, which was one of the most southern retreats observed in the historical record. Consistent with the far southern retreat of the LC after the first LCE separation, the second LCE separation event was detected in color images in February 1980, approximately 19 months later, which is the longest LCE separation period observed in the entire 35-year record from 1978 through 2012.

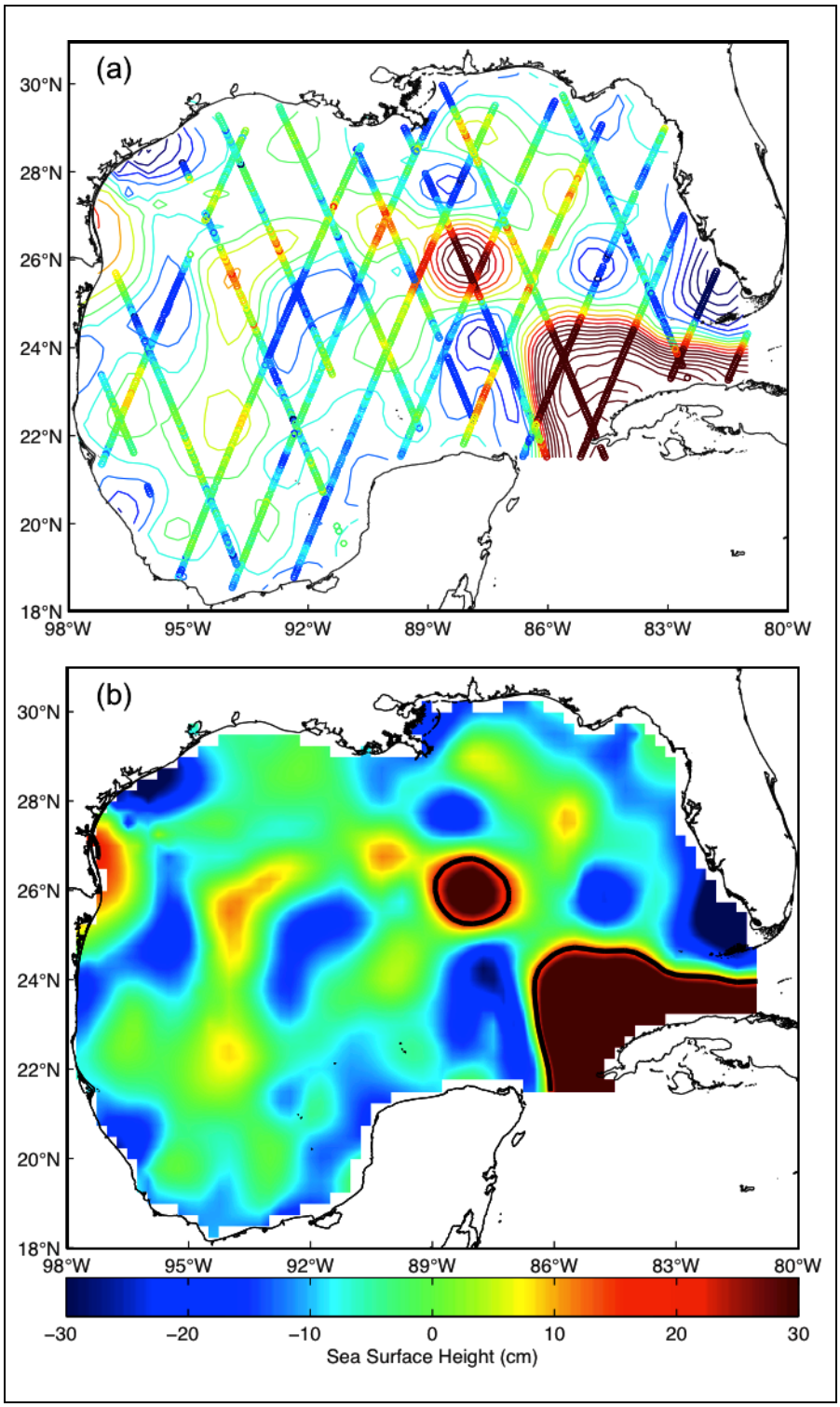

Fig. 3. Loop Current eddy 1978 as observed by Seasat approximately 2 weeks after eddy separation. Shown (a) as color-mapped along-track data overlaid on a contour plot of the objectively-mapped sea surface height (contour increment = 5 cm), and (b) as a sea surface height color image with the 17-cm Loop Current tracking contour overlaid. Along-track data are from July 16 through August 9, 1978. The analysis date of the mapped data is July 28, 1978.

The retreat latitudes of the LC following LCE separation derived from SSH are not equivalent to retreat latitudes derived from SST or ocean color fronts. In Forristall et al. (2010) the edge of the LC, as defined by the 17-cm SSH tracking contour used to track the LC in the CCAR mesoscale SSH data products, was estimated to lie inside of the surface thermal or ocean color front by about 40 km. Along the northern edge of the LC front this offset is 0.36°, which must be added to each SSH-derived retreat latitude value to allow consistent analyses of the LC retreat latitudes when combining the altimetric estimates with non-altimetric estimates. The two retreat latitudes derived from altimetry during the pre-altimetry time period, shown in Table 1, do not incorporate the offset; however, the offset was applied before calculation of the mean.

Figures 4, 5, and 6 show imagery of all pre-altimetric eddies with exception of the two SSH-derived events shown in Figs. 3 and 7, respectively, that were detected using Seasat and ERS-1 altimetry. The black dashed lines show the derived LC retreat latitudes. Each eddy in Table 1 has been given a year or year-letter designation since multiple LCEs were shed in some years. Note that the EddyWatch™ chart in Fig. 6q shows a deeply retreated Loop Current, although the SST data for the respective date suggest that the LC maximum latitude was further north. Two eddy separation events, LCE 1984b (#11, 28 Aug 1984) and LCE 1986b (#14, 12 Sep 1986), do not fall within the date range of the corresponding image/chart. For those events, I have provided images where the LC and LCE can be most clearly seen, although the movie sequences of satellite imagery and GEM P&C analyses suggest that separation happened a week to a month before the images shown in Fig. 5j and Fig. 6m. Table 2 gives the data type and date range for the data used to create each image in Figs. 4,5, and 6. For the most part, the dataset used to create each image was also used to determine the respective separation date. The exceptions used GEM P&C analyses to set the separation date and are marked with a superscript "b" in Table 2, These include two SST images, #9 and 14, and all three EddyWatch™ maps, #12, 17, and 18. Otherwise, for the event dates derived from composite chlorophyll-a images, the first date of the corresponding image date range was selected as the separation date. The date of the earliest image swath within the composite providing evidence of LCE separation was not identified, so the first date in the date range used to form the composite image was used for convenience. The separation dates derived from weekly SST images were set to mid-week.

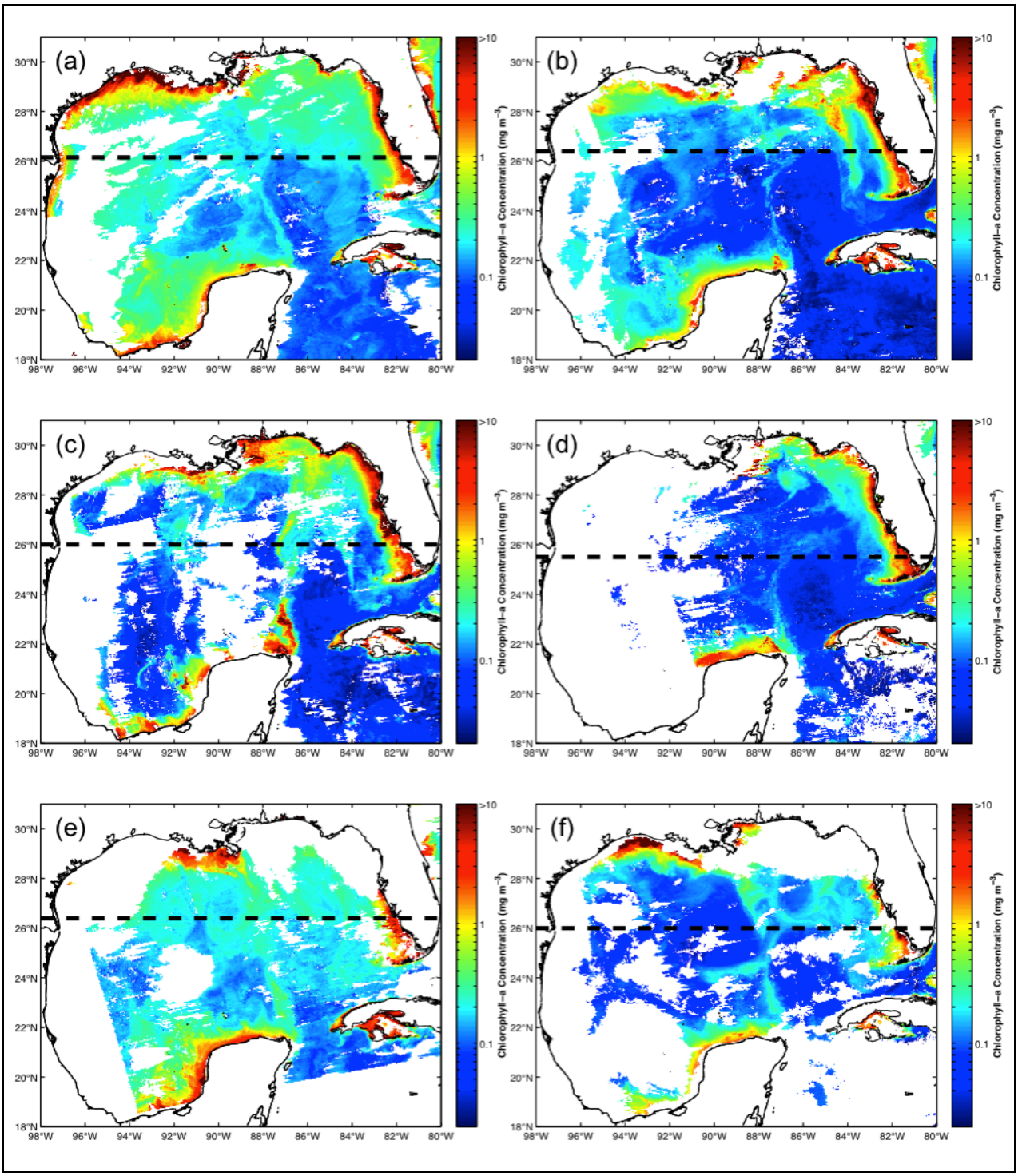

Fig. 4. Loop Current eddy separation events with Loop Current retreat latitude following separation shown by dashed black lines. Date ranges for which the plots are valid are given in Table 2. Loop Current eddy separation date: (a) 18 Feb 1980; (b) 16 May 1980; (c) 04 Aug 1980; (d) 04 Jul 1981; (e) 24 Oct 1981; (f) 21 Aug 1982.

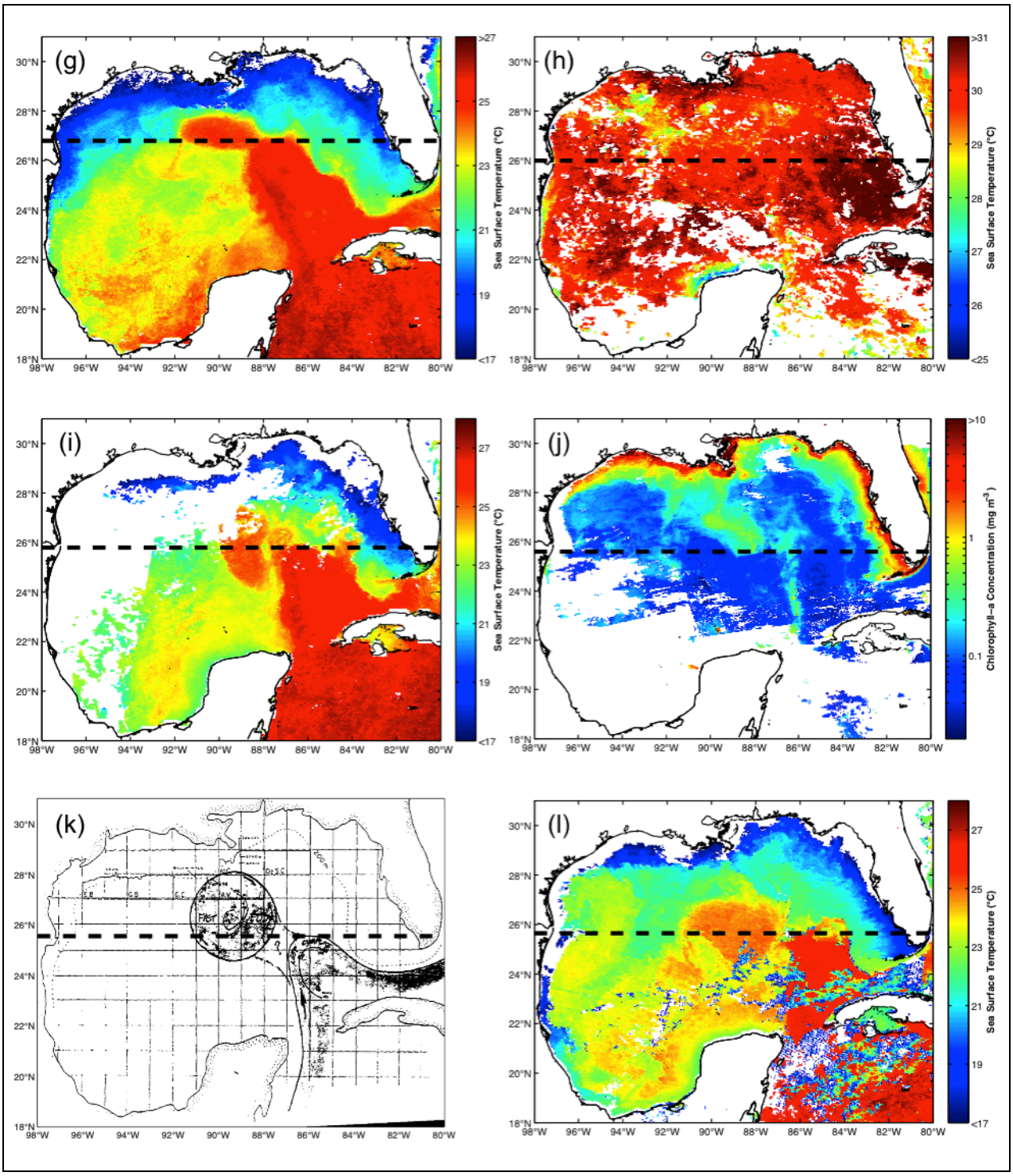

Fig. 5. Loop Current eddy separation events with Loop Current retreat latitude following separation shown by dashed black lines. Date ranges for which the plots are valid are given in Table 2. Loop Current eddy separation date: (g) 08 Mar 1983; (h) 23 Aug 1983; (i) 25 Jan 1984; (j) 28 Aug 1984; (k) 18 Jul 1985; (l) 18 Jan 1986.

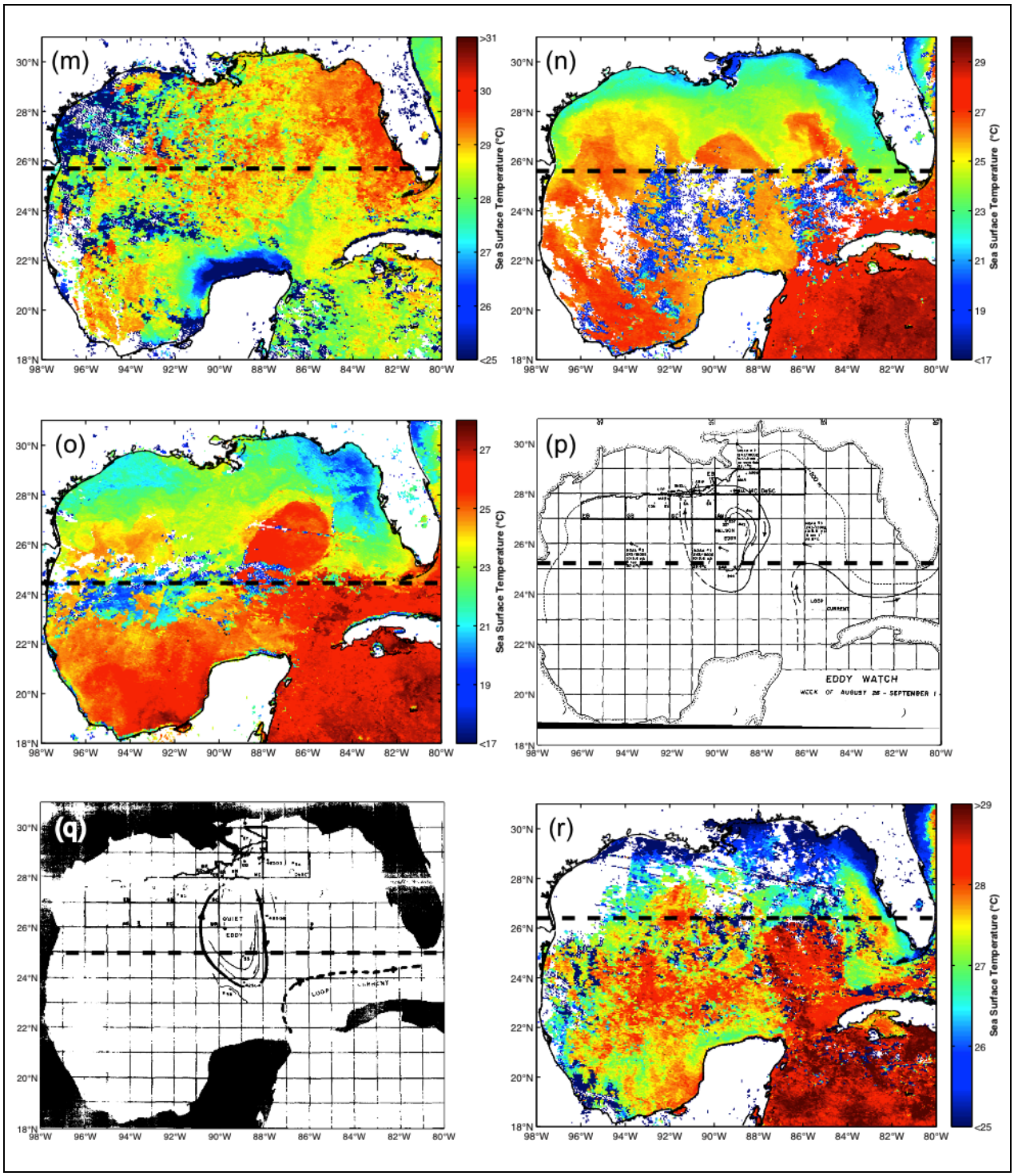

Fig. 6. Loop Current eddy separation events with Loop Current retreat latitude following separation shown by dashed black lines. Date ranges for which the plots are valid are given in Table 2. Loop Current eddy separation date: (m) 12 Sep 1986; (n) 08 Nov 1987; (o) 25 Apr 1988; (p) 01 Sep 1989; (q) 14 Sep 1990; (r) 01 Nov 1991.

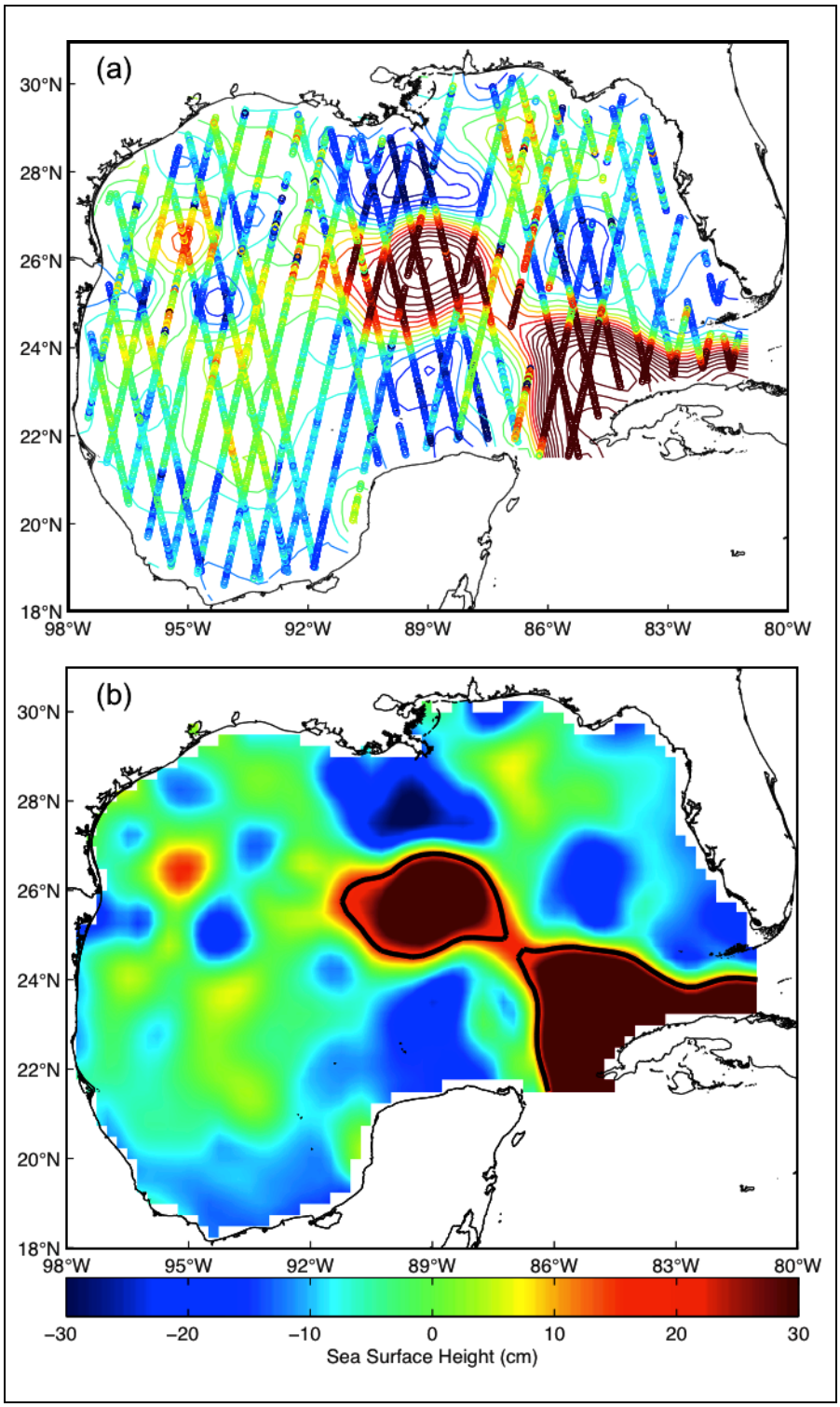

Fig. 7. Loop Current eddy 1992 "Unchained" as observed by ERS-1 on the date of separation, August 10, 1992. Shown (a) as color-mapped along-track data overlaid on a contour plot of the objectively-mapped sea surface height (contour increment = 5 cm), and (b) as a sea surface height color image with the 17-cm Loop Current tracking contour overlaid. Along-track data are from July 24 through August 27, 1992.

Table 2. Valid date ranges for Loop Current eddy separation events shown in Figs. 4,5, and 6.

No.	Fig. No.	Separation Date	Best Available Imagery/Chart	Date Range for Data in the Image/Chart
2	4a	18 Feb 1980	Chlorophyll-a[a]	18 Feb 1980 – 25 Feb 1980
3	4b	16 May 1980	Chlorophyll-a[a]	16 May 1980 – 23 May 1980
4	4c	04 Aug 1980	Chlorophyll-a[a]	04 Aug 1980 – 11 Aug 1980
5	4d	04 Jul 1981	Chlorophyll-a	04 Jul 1981 – 11 Jul 1981
6	4e	24 Oct 1981	Chlorophyll-a[a]	24 Oct 1981 – 31 Oct 1981
7	4f	21 Aug 1982	Chlorophyll-a[a]	21 Aug 1982 – 28 Aug 1982
8	5g	08 Mar 1983	SST[a]	05 Mar 1983 – 11 Mar 1983
9	5h	23 Aug 1983	SST[a,b]	20 Aug 1983 – 26 Aug 1983
10	5i	25 Jan 1984	SST[a]	22 Jan 1984 – 28 Jan 1984
11	5j	28 Aug 1984	Chlorophyll-a	05 Sep 1984 – 12 Sep 1984[c]
12	5k	18 Jul 1985	EddyWatch™ [a,b]	12 Jul 1985 – 19 Jul 1985
13	5l	18 Jan 1986	SST	15 Jan 1986 – 21 Jan 1986
14	6m	12 Sep 1986	SST[a,b]	01 Oct 1986 – 07 Oct 1986[c]
15	6n	08 Nov 1987	SST	05 Nov 1987 – 11 Nov 1987
16	6o	25 Apr 1988	SST[a]	22 Apr 1988 – 28 Apr 1988
17	6p	01 Sep 1989	EddyWatch™ [a,b]	26 Aug 1989 – 01 Sep 1989
18	6q	14 Sep 1990	EddyWatch™ [a,b]	07 Sep 1990 – 14 Sep 1990
19	6r	01 Nov 1991	SST[a]	29 Oct 1991 – 04 Nov 1991

[a] GEM P&C analyses (Evans-Hamilton, 1992) were available to verify separation date estimate.
[b] GEM P&C analyses determined separation date estimate.
[c] Images shown in Fig. 5j and Fig. 6m do not depict the official separation dates but do show the Loop Current eddy more clearly separated than the corresponding images.

The goal of the reanalysis was to derive a pre-altimetric LC record as consistent as possible with the LCE separation record derived from satellite altimetry using an automated LC tracking procedure based on tracking the 17-cm LC contour in CCAR SSH maps (Leben, 2005). Since altimetry well-resolves only the dominate GOM mesoscale ocean circulation, small anticyclonic eddies generated near the periphery of the LC are typically not detected at the 17-cm level in the gridded CCAR SSH data products. SST imagery, however, may show warm surface features on the periphery of the LC that are not LCEs per se because the subsurface waters below these features are not warm Caribbean water comprising the LC and LCEs. These features are usually smaller in diameter and exhibit a weaker surface thermal expression than LCEs. They may also be associated with cyclonic circulation that can be identified by the time evolution of the SST pattern. Nevertheless, SST signatures of some of the smallest LCEs in the

20-year altimetry record (i.e. Zapp, Walker, Brazos, etc.) were compared with the signatures of the pre-altimetry eddies to ensure that all eddies identified in the pre-altimetric record were large enough to be counted as LCEs. Since all of the LCEs in the altimetry record are "verified" – that is, all LCEs appearing in the SST during the altimetry time period have been confirmed by the corresponding altimetry – eddies in the pre-altimetry record are considered LCEs as long as their surface areas or surface thermal signatures are comparable or larger than the smallest LCEs observed during the altimetry period. All the pre-altimetry LCEs identified in the reanalysis meet this criterion. Neither was a minimum lifetime nor minimum separation interval required of the LCEs counted in the reanalysis. Beyond these caveats, the guidelines used for counting events were necessarily subjective: cohesive masses of water separating from the LC and causing significant change in LC area were deemed to be LCEs provided they did not reattach to the LC at a later date.

Each LCE in the *altimetry* record was assigned a discrete date marking the completion of the eddy separation process, objectively derived using the continuous sampling afforded by the multi-satellite altimetry and the breaking of the LC tracking contour**.** Yet, eddy separation is a slow, continuous process that happens over the entire depth of the LC water column and can take months to complete. The estimated uncertainty in objective altimetric estimates when compared with coincident subjective estimates is +/-1 month (Leben, 2005). SST and ocean color sampling, however, are frequently interrupted by cloud-cover, often preventing clear views of ongoing separation processes. Therefore, LC and LCE signatures in SST and ocean color imagery can be difficult to identify. Complex surface flows may obscure the northern boundary of the LC and the connectivity of the LC with a separating LCE. GEM analyses also may show large changes in LCE diameters and large variations in LCE positions. These uncertainties impact retreat latitude and separation date estimates in the pre-altimetric record. As such, the separation dates derived in the reanalysis are probably accurate to only +/-1.5 months, and the retreat latitudes to only +/-0.25° at best.

CHAPTER III

COMPARISONS OF PREVIOUSLY PUBLISHED PRE-ALTIMETRY SEPARATION DATES WITH THE REANALYSIS

Various versions of the LCE separation record over the pre-altimetry time period have been published and republished in the peer-reviewed literature (Vukovich 1988; Sturges 1993; Sturges 1994; Sturges and Leben 2000; Leben 2005) with the most recent being Vukovich (2012). Present comparisons and discussion focus on Vukovich (2012), since that work replicates and extends the pre-1988 separation record published in Vukovich (1988) and provides more information on the sampling available during the pre-altimetry time period. The other studies cited above and other recent publications (Chang and Oey 2012; Chang and Oey 2013a&b) relied on the record published in Vukovich (1988). Therefore, it is important to review these early records of LCE separation and compare them with the reanalysis included in this dissertation.

Table 3 shows the LCE separation dates from the reanalysis (Table 1) and corresponding dates in Vukovich (2012). For the pre-altimetry time period (1978-1992), Vukovich (2012) employed NASA CZCS ocean color (or chlorophyll-a) data from 1979 through 1985, "ship-of-opportunity" data, and SST data to identify LCE separations. SST came primarily from NOAA AVHRR instruments, though SST data from NOAA VHRR, the Geostationary Operational Environmental Satellite (GOES), Seasat, and the Heat Capacity Mapping Mission (HCMM) were also used. (Vukovich (2012) relied heavily on NOAA VHRR SST to derive dates from 1972 through 1978.) Unfortunately, Vukovich (2012) does not specify which SST data source was used to identify specific separation events. The last usable VHRR data were collected on Mar. 1, 1979 (NOAA 5 satellite), before the second LCE separation event in early 1980 (Table 3). AVHRR coverage began with the launch of the first four-channel AVHRR instrument (TIROS-N satellite) on Oct. 13, 1978. The AVHRR instrument was later enhanced to include five channels and was then put into operational use onboard NOAA 7 on Jun. 23, 1981 (Casey et al., 2010; Kramer, 2002; Schnapf, 1981). AVHRR coverage lasted through the end of the pre-

altimetry time period and beyond. VHRR LC monthly frontal analyses including copies of the original SST maps over the time period from 1972 through 1977 are found in Vukovich et al. (1978) and Vukovich et al. (1979). Other AVHRR SST monthly frontal analyses and imagery are found in Vukovich and Maul (1985), Vukovich (1986), Vukovich and Crissman (1986), Vukovich (1988), Vukovich (2007), and Vukovich (2012). GOES SST may have been used for any number of events, but were minimally used according to the description in Vukovich (2012). Seasat recorded both microwave and infrared SST, although these data were only available from July to October 1978, after the first and before the second Vukovich (2012) LCE separation found in Table 3. No separation events could have been directly observed with the Seasat data, given the identified separation dates. Additionally, Table 5 of Vukovich (2012) indicates that no usable data were available in the GOM during the entire lifetime of Seasat. The HCMM satellite was launched in April 1978 and was decommissioned in August 1980, so it could only have been used to help identify the first three of the Vukovich (2012) separation events listed in Table 3 (Kramer, 2002). Table 4 of Vukovich (2012) indicates which data type – ocean color, SST, or ship-of-opportunity – was used to derive each of the LCE separation dates.

Table 3. Comparison of reanalysis Loop Current eddy separation dates with those from Vukovich (2012).

No.	Year-Letter	Industry Name	Reanalysis	Vukovich (2012)[a]	Difference (days)[b]
1	1978	-	15 Jul 1978	Jun 1978	30
-	-	-	-	Apr 1979	-
2	1980a	-	18 Feb 1980	Jan 1980	34
3	1980b	-	16 May 1980	-	-
4	1980c	-	04 Aug 1980	-	-
5	1981a	-	04 Jul 1981	Mar 1981	111
6	1981b	-	24 Oct 1981	-	-
7	1982	-	21 Aug 1982	May 1982	98
8	1983a	-	08 Mar 1983	Mar 1983	-7
9	1983b	-	23 Aug 1983	-	-
10	1984a	-	25 Jan 1984	Feb 1984	-21
11	1984b	Arnold	28 Aug 1984	-	-
12	1985	Fast	18 Jul 1985	Jul 1985	3
13	1986a	Hot Core	18 Jan 1986	Jan 1986	3
14	1986b	Instant	12 Sep 1986	Oct 1986	-33
15	1987	Kathleen	08 Nov 1987	Nov 1987	-7
16	1988	Murphy	25 Apr 1988	May 1988	-20
17	1989	Nelson	01 Sep 1989	May 1989	109
18	1990	Quiet	14 Sep 1990	Sep 1990	-1
19	1991	Triton	01 Nov 1991	Sep 1991	47
20	1992	Unchained	10 Aug 1992	Jul 1992	26
				Mean	24.8
				rms	52.1
				Mean without #5, 7, and 17	4.5
				rms without #5, 7, and 17	24.1

[a] Dates for Loop Current eddy separation events that occurred in the 1970s and after 1992 are listed in Vukovich (2012).

[b] Differences assumed that all Vukovich (2012) separation events occurred on the 15th of the given month.

All available information on ocean features were integrated into monthly frontal analysis maps indicating the location of LC and LCE fronts (e.g. Vukovich (2012), Fig. 1). As noted in the preceding discussion, satellite SST data played a major role in the development of these analyses. In the time periods 1972 through 1978 and 1986 through 1991, only satellite SST data were available to develop the frontal analyses. (Details in Vukovich (2012) describing events preceding 1978 are largely omitted from this dissertation since online data archives do not exist

for satellite data from that time period.) Information provided in Table 5 of Vukovich (2012) indicates that satellite data were insufficient to map LC and LCE fronts during June through October every year from 1978 through 1983 and for two to five months every summer and fall for the years 1984 through 1991. This is because the LC and LCE fronts could not be detected in SST imagery when the warm seasonal mixed layer masked the surface thermal signature of the fronts. According to Vukovich (1988) there were generally only five to nine clear-sky images during the months from November through May, and only occasionally were images in late October and early June usable. When SST frontal analyses were insufficient for LC tracking, Vukovich (2012) used ship-of-opportunity data. Specifically, ship-of-opportunity data were used to identify LCE separations #1, 12, 18, 19, and 20 in Table 3 (ship-of-opportunity data were used exclusively to derive #18, 19, and 20). According to Table 5 of Vukovich (2012), there were no data available during the time periods when LCE separation events #1, 12, 14, 18, and 19 occurred, and LCE #20 was ambiguously reported to have "missing" data. Five of these six LCE separation events were derived with ship-of-opportunity data. The ship-of-opportunity data may not have provided much useful information, however, since there were either missing or no data at the actual times of separation for the five events. The six total events with missing or no satellite data must have been estimated using procedures that are not described in the literature. Therefore, it is difficult to evaluate the efficacy of the LC or LCE monitoring during these time periods or to reproduce the results reported.

The criteria met by each LCE separation listed in Vukovich (2012) are the following: only LCE separation events shedding eddies with a diameter of "about" 300 km or greater at the time of separation that persisted for five months or more and propagated into the western GOM were counted. There are significant differences between the reanalysis dates and the Vukovich (2012) dates in Table 3. Vukovich (2012) identified one separation event in April 1979 that GEM analyses and CZCS imagery showed was an eddy detachment since the eddy later reattached to the LC. As a result, that event was ignored in the reanalysis. Five eddies detected in the reanalysis do not appear in Vukovich (2012) (#3, 4, 6, 9, and 11 in Table 3), four of which

relied primarily on chlorophyll-a data. Three of the five eddies (#4, 6, and 9) separated in time periods when Vukovich (2012) reported no data were available. This includes the event that was identified using SST imagery (#9). The other two (#3 and 11) may have been undetected in the chlorophyll-a or failed to meet LCE diameter criteria. Diameter approximation using chlorophyll-a or SST imagery is a subjective process since cloud cover, meanders, surface layer masking, and peripheral cyclones frequently conceal full eddy areal coverage. Vukovich (2012) may have estimated that the diameters of these two LCEs were less than 300 km, or these eddies may have been ignored because they could not be tracked for five months into the western GOM. In the reanalysis, LCEs were often impossible to track systematically beyond about three months after separation unless trajectory information from GEM P&C analyses was available. In SST and chlorophyll-a images LCE surface signatures typically fade into the background less than five months after eddy separation. If the five-month eddy lifetime requirement had been strictly enforced in the reanalysis, many of the early LCE events including eddy #3 and #11 would have been eliminated. It is noteworthy that Kirwan et al. (1984) documented the fall-separated LCE #4, which was followed using three NOAA satellite-tracked drifting buoys. This appears to be the only mention of this LCE separation event reported in the peer-reviewed literature. The event does not appear in published LCE separation event censuses (Vukovich, 1988; Sturges, 1994) or their republications (Sturges and Leben, 2000; Leben 2005; Vukovich, 2012).

Beyond differences in the number of LCE separations listed in Table 3, there are also some differences between the separation dates in the reanalysis and those in Vukovich (2012) for the events that were identified in both studies. Assuming that each date in Vukovich (2012) corresponds to the 15th day of the respective month, nine separation dates differ by one month or less (#1, 8, 10, 12, 13, 15, 16, 18, and 20) and three events (#2, 14, and 19) differ by between one and two months. These 12 events show good agreement (mean = 4.5 days, rms = 24.1 days), comparable to uncertainty estimates of LCE separation dates found between subjective tracking by an expert and automated altimetric tracking in Leben (2005) (mean = 3 days, rms = 28 days). The three other events, however, differ by more than three months (#5, 7, and 17) and degrade

uncertainty estimates substantially (mean = 24.8 days, rms = 52.1 days). The reanalysis separation dates for these separation events fell in summer, when Vukovich (2012) reported that no satellite data were available. Instead, Vukovich (2012) reported that all of these summer separation dates were in the late winter or spring.

Satellite data and industry analyses used in the reanalysis were significantly different than the data used in Vukovich (2012). Pathfinder AVHRR SST data (August 1981-1992) were employed extensively in the reanalysis. The Pathfinder SST program began in the early 1990s and is a NASA/NOAA/NODC joint effort to produce a long, accurate, and consistent AVHRR data record. Newly reprocessed SST data from 1985 through 2001 were released by NODC in April 2003, and reprocessed SST data from 1981 through 1984 were released in April 2009 (Casey et al., 2010). Since Vukovich (2012) agrees entirely with all pre-1988 separation dates presented in Vukovich (1988) and makes no mention of Pathfinder, it is very likely that none of the improved information provided in the pre-1988 Pathfinder SST reprocessing had any impact on Vukovich (2012). AVHRR data prior to August 1981, VHRR, Seasat, HCMM, and GOES SST were not used at all in the reanalysis, and were only minimally used by Vukovich (2012). CZCS ocean color data were employed considerably more in the reanalysis. Table 4 in Vukovich (2012) shows that in no instance during the pre-altimetry time period was a separation event identified using exclusively ocean color data, and there were only two instances (#7 and 12) that ocean color was used at all. Conversely, the reanalysis used CZCS to derive seven event dates (#2, 3, 4, 5, 6, 7, and 11), two of them exclusively (#5 and 11). See Table 1. In the reanalysis, CZCS chlorophyll-a images were reliable from May through August and also at times during the months of February, March, April, September, and October. Missing frontal analyses during the summer and fall of 1978 through 1985 listed in Table 5 of Vukovich (2012) indicate little or no reliance on CZCS ocean color data for LC tracking. This may be an artifact of the CZCS data processing available at the time that the original published analyses in Vukovich (1988) were performed. The reanalysis reported here benefited greatly from the comprehensive reprocessing of the CZCS archive by NOAA and NASA (Gregg et al., 2002). Ship-of-opportunity data were

not used in the reanalysis; however, 15 of the 20 pre-altimetry separation dates were covered by GEM analyses (see Table 1) that incorporate ship survey data and offer additional kinematic information about LCE separation from satellite-tracked drifting buoy trajectories. EddyWatch™ reports were also available, providing frontal analyses as well as ship surveys and satellite-tracked drifting buoy tracks used by the offshore industry for operational monitoring of the LC. Seasat altimetry data were used to map SSH in the GOM just after the separation of the first event counted in the reanalysis (LCE 1978). ERS-1 altimetry was used to derive event #20, LCE 1992 "Unchained".

In summary, there were time periods noted both in the reanalysis and by Vukovich (2012) when satellite data quality was poor, with the eastern GOM obscured by clouds or the LC masked by seasonal warming of the mixed layer, making identification of LC and LCE fronts and LCE separation events during the summer and fall difficult without ancillary information such as that provided from ship-board surveys and satellite-tracked drifting buoys. Nevertheless, in the reanalysis more satellite coverage was found than was described in Vukovich (2012). Compared to the datasets used to estimate the separation dates in Vukovich (2012), the reanalysis included more satellite data during summer and late fall and had access to supplementary information provided by the EddyWatch™ and GEM analyses. Thus, the separation dates in the reanalysis are likely more accurate and less affected by seasonal data outages than those reported in Vukovich (2012). Regardless of the reasons for the inconsistencies between the reanalysis and the published record of Vukovich (2012), misreporting, overreporting, or underreporting of LCE separation events can substantially affect separation statistics. Discussion of whether date discrepancies like those found in the data comparison shown in Table 3 prevented identification of a seasonal LC signal will be pursued in Chapter V of this dissertation.

CHAPTER IV

ALTIMETRIC LOOP CURRENT RECORD

Since the pre-altimetry data record is inhomogeneous and inconsistent in quality, consisting of many different data types processed in different ways, it was impractical to make extensive LC "measurements" beyond LCE separation dates (Chapters II and III). Pre-altimetry LC and LCE boundaries are frequently unclear and vary greatly from one data type to another. Conversely, the altimetry record consists of only one continuous data type, free of intermittent or seasonal data outages. As such, I was able to perform various sensitivity tests to find if LC seasonality is consistently evident regardless of data processing methods. Processing methods can sometimes advance or delay LCE separation dates and change size and shape characteristics of the LC itself in the data, which may mask or accentuate seasonality. While statistical discussion of LC seasonality will be given in Chapters V and VI, the purpose of the present chapter is to introduce some of the common data processing techniques currently in use and their ultimate effect on LCE separation dates and LC characteristics. I begin with a description of altimetry products.

CCAR, AVISO, and AVISO-CUPOM Basic Altimetry Product Description

The 20-year multi-satellite altimeter data record was used to investigate LC intrusion and LCE separation events over the time period from January 1993 through December 2012. Analyzed altimetry datasets included daily CCAR and AVISO SSH and a hybrid daily SSH based on AVISO SSHA added to the CUPOM model mean (AVISO-CUPOM). CUPOM is a model SSH estimation of the GOM mean dynamic topography (MDT) computed for the time period 1993 through 1999 from a data assimilation hindcast experiment performed by Drs. Lakshmi Kantha and Jei Choi for the MMS Deepwater Physical Oceanography Reanalysis and Synthesis Program (Nowlin et al., 2001). A MDT estimate of some kind is needed to convert SSHA to SSH. CUPOM is the model mean used when creating the CCAR SSH product, whereas the AVISO product incorporates a different MDT estimate, CNES/CLS 2009 Mean Dynamic Topography (Rio and Larnicol, 2010). The daily AVISO and AVISO-CUPOM datasets were created from the delayed-time weekly ¼° AVISO SSH (absolute dynamic topography) dataset, linearly interpolated to daily maps. AVISO and AVISO-CUPOM datasets were both demeaned in the deepwater by subtracting the daily-averaged values of SSH in water deeper than 200 m in the GOM to remove the steric signal associated with seasonal heating of the mixed layer. The steric signal appears approximately as an annual sine wave with 5.8 cm amplitude in AVISO SSH, with the peak near Sept. 15 and the trough near Mar. 16. The demeaning procedure was not applied to the CCAR SSH because the along-track altimeter data are detrended before gridding of the CCAR SSH fields, which effectively removes the steric signal. Satellite altimeter missions that provided sampling used in the CCAR SSH product are shown in Fig. 8. Tandem or better satellite coverage was available during nearly the entire record, except for three months in early 1994 when ERS-1 was placed into a 3-day exact repeat orbit for ice sheet mapping and only TOPEX/Poseidon altimeter data were available. Additional information about the CCAR SSH product is provided in Leben et al. (2002). Specifics of satellite coverage used in the AVISO (and AVISO-CUPOM) dataset are not documented, but are likely comparable to that used in the CCAR dataset.

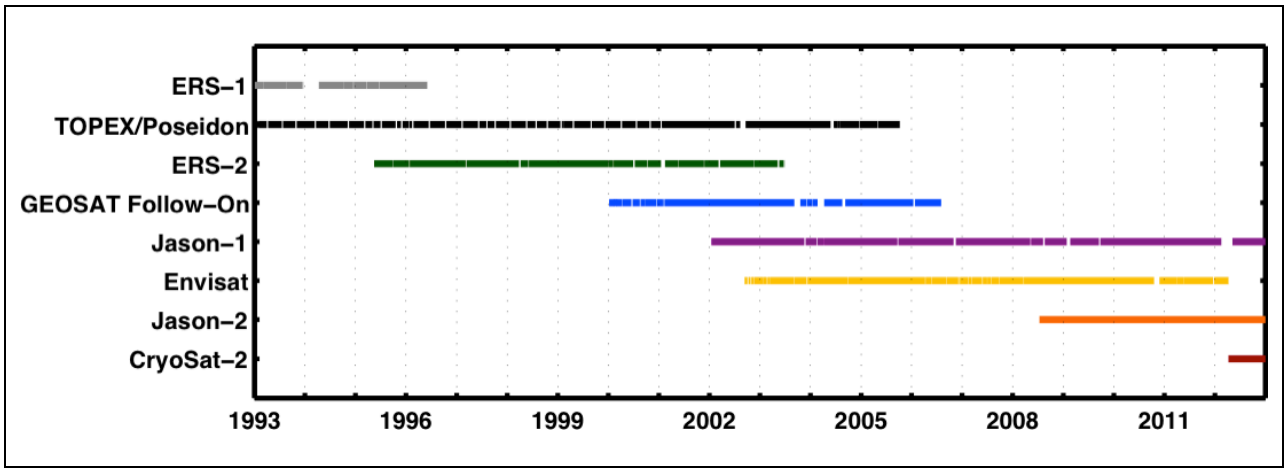

Fig. 8. Satellite usage in the CCAR gridded altimeter dataset during the time period from 1993 through 2012.

Loop Current Eddy Separation and Detachment Dates and Their Relation to Altimetry Product Mean Dynamic Topographies

LCE separation dates and LC metrics (Leben, 2005) were derived using a MATLAB® toolbox developed at CCAR called the Loop Current Toolbox (LCT). The LCT automatically identifies and tracks the LC and LCEs in gridded SSH datasets. LC and LCE boundaries are defined by the location and breaking of the 17-cm tracking contour. CCAR separation dates are given in Table 4 along with the corresponding retreat latitudes and separation periods. Retreat latitude is defined as the maximum latitude of the LC immediately following separation of a LCE (Leben, 2005). In the LCT, the retreat latitude is equal to the minimum value of the maximum latitude of the LC tracking contour observed in SSH maps during the first five days after LCE separation. In the CCAR SSH dataset, the mean separation period is 243.3 days, and the mean retreat latitude is 26.2° (with offset; see Chapter II). Table 5 compares the CCAR LCE separation dates with the corresponding dates derived from the AVISO and AVISO-CUPOM SSH datasets.

Table 4. Loop Current eddy separation event dates with the corresponding retreat latitudes and separation periods from January 1993 through December 2012, derived from CCAR SSH dataset. The HMI industry name of each event is listed also.

No.	Year-Letter	Industry Name[a]	Separation Date	Confirmation Dataset	Retreat Latitude (°)	Separation Period (days)
21	1993a	Whopper	10 Jul 1993	SSH	27.1	334
22	1993b	Xtra	11 Sep 1993	SSH	26.5	63
23	1994	Yucatan	26 Aug 1994	SSH	26.2	349
24	1995a	Zapp	19 Apr 1995	SSH	26.8	236
25	1995b	Aggie	07 Sep 1995	SSH	25.5	141
26	1996a	Biloxi	15 Mar 1996	SSH	26.2	190
27	1996b	Creole	25 Oct 1996	SSH	24.6	224
28	1997	El Dorado	30 Sep 1997	SSH	25.2	340
29	1998	Fourchon	22 Mar 1998	SSH	24.7	173
30	1999	Juggernaut	28 Sep 1999	SSH	25.2	555
31	2001	Millennium	10 Apr 2001	SSH	25.7	560
32	2002a	Pelagic	28 Feb 2002	SSH	27.3	324
33	2002b	Quick	13 Mar 2002	SSH	24.7	13
34	2003	Sargassum	05 Aug 2003	SSH	26.6	510
35	2004a	Titanic	08 Feb 2004	SSH	25.8	187
36	2004b	Ulysses	26 Aug 2004	SSH	25.0	200
37	2005	Vortex	13 Sep 2005	SSH	26.8	383
38	2006a	Walker	08 Feb 2006	SSH	27.3	148
39	2006b	Xtreme	04 Mar 2006	SSH	26.0	24
40	2006c	Yankee	26 Sep 2006	SSH	25.8	206
41	2007a	Zorro	07 Jun 2007	SSH	26.1	254
42	2007b	Albert	16 Nov 2007	SSH	26.2	162
43	2008a	Brazos	06 Mar 2008	SSH	26.3	111
44	2008b	Cameron	01 Jul 2008	SSH	26.0	117
45	2009a	Darwin	24 Feb 2009	SSH	25.4	238
46	2009b	Ekman	29 Aug 2009	SSH	24.9	186
47	2010	Franklin	01 Oct 2010	SSH	25.0	398
48	2011	Hadal	14 Aug 2011	SSH	25.9	317
49	2012a	Icarus	03 Feb 2012	SSH	25.9	173
50	2012b	Jumbo	04 Aug 2012	SSH	24.3	183
				Mean	26.2[b]	243.3

[a] Using an earlier version of the CCAR SSH dataset, Leben (2005) identified HMI eddy Odessa/Nansen as a minor eddy. In the current CCAR SSH dataset Odessa/Nansen was completely insignificant and was excluded from further analysis.

[b] An offset of 0.36° must be added to SSH-derived retreat latitudes to make them consistent with the pre-altimetry retreat latitude values in Chapter II estimated from satellite SST and ocean color frontal analyses. The offset was not added to the retreat latitudes listed in the table, but was applied when calculating the mean. The mean of the values listed in the table is 25.8°.

Table 5. Comparison of Loop Current eddy separation event dates derived from CCAR, AVISO, and AVISO-CUPOM SSH datasets from January 1993 through December 2012.

No.	Industry Name	CCAR	AVISO	AVISO-CUPOM
21	Whopper	10 Jul 1993	08 Jul 1993	08 Jul 1993
22	Xtra	11 Sep 1993	04 Sep 1993	06 Sep 1993
23	Yucatan	26 Aug 1994	19 Aug 1994	24 Aug 1994
24	Zapp	19 Apr 1995	17 Apr 1995	15 Apr 1995
25	Aggie	07 Sep 1995	01 Sep 1995	08 Sep 1995
26	Biloxi	15 Mar 1996	08 Mar 1996	15 Mar 1996
27	Creole	25 Oct 1996	20 Jul 1996	17 Aug 1996
28	El Dorado	30 Sep 1997	25 Sep 1997	29 Sep 1997
29	Fourchon	22 Mar 1998	12 Feb 1998	20 Feb 1998
30	Juggernaut	28 Sep 1999	28 Sep 1999	05 Oct 1999
31	Millennium	10 Apr 2001	29 Mar 2001	07 Apr 2001
32	Pelagic	28 Feb 2002	24 Feb 2002	26 Feb 2002
33	Quick	13 Mar 2002	[a]	02 Mar 2002
34	Sargassum	05 Aug 2003	11 Aug 2003	11 Aug 2003
35	Titanic	08 Feb 2004	20 Dec 2003	24 Dec 2003
36	Ulysses	26 Aug 2004	19 Aug 2004	21 Aug 2004
37	Vortex	13 Sep 2005	11 Sep 2005	10 Sep 2005
38	Walker	08 Feb 2006	06 Feb 2006	03 Feb 2006
39	Xtreme	04 Mar 2006	12 Feb 2006	02 Mar 2006
40	Yankee	26 Sep 2006	15 Sep 2006	18 Sep 2006
41	Zorro	07 Jun 2007	[b]	09 Jun 2007
42	Albert	16 Nov 2007	21 Oct 2007	15 Nov 2007
43	Brazos	06 Mar 2008	02 Mar 2008	04 Mar 2008
44	Cameron	01 Jul 2008	27 Jun 2008	30 Jun 2008
45	Darwin	24 Feb 2009	14 Feb 2009	23 Feb 2009
46	Ekman	29 Aug 2009	22 Jun 2009	03 Jul 2009
47	Franklin	01 Oct 2010	27 Jun 2010	04 Jun 2010
48	Hadal	14 Aug 2011	22 Jul 2011	28 Jul 2011
49	Icarus	03 Feb 2012	05 Nov 2011	11 Nov 2011
50	Jumbo	04 Aug 2012	28 May 2012	16 Jun 2012

[a] In the AVISO product, eddies Pelagic and Quick separate from the Loop Current as one eddy, though they split from each other only days after separation.
[b] Loop Current eddy Zorro appears as a detachment event in the AVISO product.

Tables 4 and 5 contain two anomalous events, LCEs Zorro and Franklin, which were large anticyclonic eddies that formed after deep LC intrusions and yet exhibited little or no westward propagation away from the LC during their lifetimes. Zorro separated from the northwestern edge of the LC in June 2007 and dissipated in 10 weeks without any significant westward propagation. Satellite tracked drifting buoys deployed in Zorro at the time of separation showed that the entire recirculation of the separated anticyclonic eddy was entrained along the outer edge of the LC and advected out of the GOM (Coholan et al., 2008). This was the first time that the rapid and total dissipation of a major anticyclonic eddy in the GOM had been observed. LCE Franklin was a relatively large eddy when it initially detached from the LC in June 2010; however, the eddy became progressively smaller as repeated reattachment and detachment cycles reduced the size and intensity of the recirculation. The weakening of the eddy circulation resulted in little or no β-induced westward propagation, since the induced velocity is a function of eddy amplitude (Nof, 1981). As a result, the eddy remained near the LC and continued to interact with the LC until early 2011.

Counting Zorro and Franklin, the number of LCE separation events identified in the CCAR, AVISO, and AVISO-CUPOM datasets over the 20-year satellite altimeter record totaled 30, 28, and 30 events, respectively. The difference in the totals is because LCEs Quick and Zorro were not distinct events in the AVISO SSH record. According to the AVISO SSH maps, LCEs Pelagic and Quick were connected and appeared as one eddy at the 17-cm contour level when they separated from the LC and then later split into the two eddies observed. In the CCAR and AVISO-CUPOM SSH maps, LCE Pelagic separates first from a deeply intruded LC followed quickly by the separation of LCE Quick, hence the name. The difference in the order of eddy separation versus splitting in the two scenarios is a consequence of the means used to estimate the total SSH. The CCAR and AVISO-CUPOM products use the CUPOM mean (Nowlin et al., 2001), whereas the AVISO product uses the CNES/CLS 2009 Mean Dynamic Topography (Rio and Larnicol, 2010).

CUPOM and CNES/CLS 2009 are both estimates of the MDT, but there are considerable differences in amplitude and spatial structure of the two estimates. To evaluate which of the two is the better estimate, I was able to compare CCAR SSH and AVISO SSH products to in situ data collected over the time period from 03 May 2009 through 23 Oct 2011 by an array of inverted echo sounders with pressure (PIES). The PIES were deployed as part of the Bureau of Ocean Energy Management "Observations and Dynamics of the Loop Current" study program (Hamilton et al., 2014). Their data were the most accurate available measure of SSH and MDT, though the PIES array study region did not encompass the entire surface area of LC territory. The better of the two altimetry products should more closely match the PIES SSH within the PIES study region over the PIES data time period than the other. The better altimetry product in this respect should also have the better MDT estimate. To perform the comparison, I first accounted for the different reference levels used in each of the altimetry SSH datasets. I elected to reference each of the SSH fields so that the 17-cm contour would be consistent between the three datasets. This was done using the regressions shown in Fig. 9. First, I estimated the 17-cm tracking contour in the PIES dataset from the regression of the PIES daily spatial mean SSH values onto the CCAR daily spatial mean SSH values in the PIES study region (Fig. 9a). From this regression, I estimated that the CCAR 17-cm tracking contour corresponds to the 259.6-cm PIES contour. I then estimated that the 259.6-cm PIES contour corresponds to the 12.1-cm AVISO SSH contour using the regression of the PIES *weekly* spatial mean SSH values onto the AVISO *weekly* (daily used for all other portions of Chapter IV) spatial mean SSH values in the PIES study region (Fig. 9b). Offsets were calculated to make the corresponding Loop Current tracking contours in all mean surfaces equivalent. This allowed direct comparison of the two altimetric temporal SSH means to the PIES temporal SSH mean during the study program, which is shown in Fig. 10.

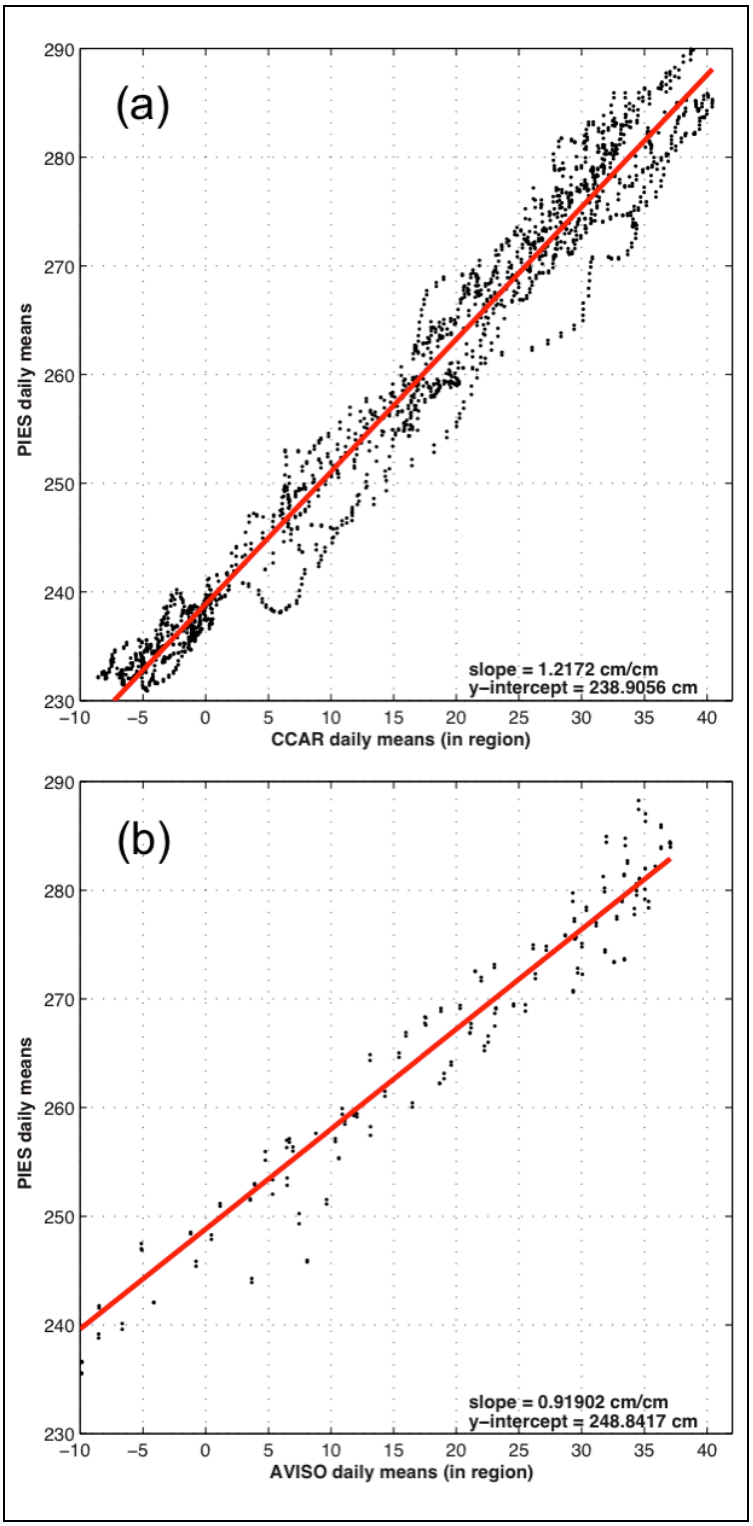

Fig. 9. Regression of the daily means of the PIES (inverted echo sounder with pressure) mapped sea surface height onto the means of the (a) CCAR mapped sea surface height and (b) AVISO mapped sea surface height in the PIES study region, over the PIES study time period (03 May 2009 through 23 Oct 2011). Daily and weekly sampling were used to derive the CCAR and AVISO regressions, respectively.

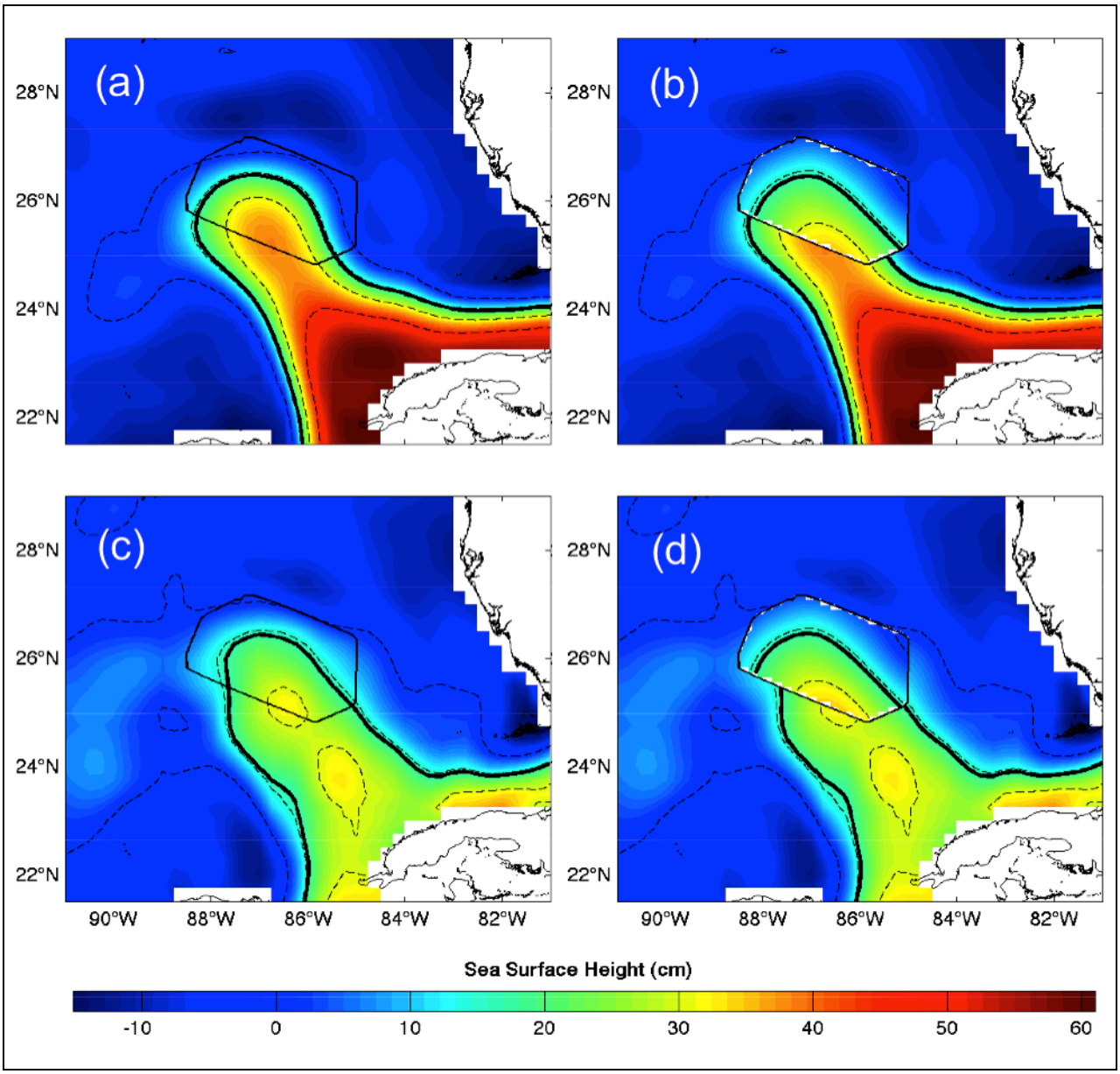

Fig. 10. CCAR mean sea surface height map both (a) without and (b) with PIES (inverted echo sounder with pressure) mean sea surface height overlaid in PIES study region along with AVISO mean sea surface height map (c) without and (d) with PIES mean sea surface height overlaid in PIES study region, over the PIES study time period (03 May 2009 through 23 Oct 2011). Thick black lines show the PIES study region boundary and the equivalent 17-cm Loop Current tracking contour. The dashed lines are at 15 cm increments.

The CCAR SSH mean over the PIES study time period is shown in Fig. 10a, with the PIES study region outlined at the northern tip of the LC. The same CCAR mean is shown again in Fig. 10b, only with the PIES SSH mean plotted in the study region. The CCAR mean 17-cm

tracking contour very nearly connects with the PIES mean tracking contour on the left side of the study region, but not as much so on the right. However the 30 cm dashed contour connects exactly on the right, but not as well on the left. Figure 10c and 10d show the AVISO SSH mean and PIES mean. Tracking contour matching is very poor between AVISO and PIES on the left side of the study region, but is nearly perfect on the right. The 30 cm PIES contour is bigger than the AVISO 30 cm contour and does not match up with the AVISO contour at all. These results indicate that magnitude values of the AVISO MDT estimate, CNES/CLS 2009, are too low within the LC. As additional support of this statement, the SSH in the AVISO product has been observed to be sufficiently low at times to allow LC streamlines to intersect the northern coast of Cuba, a physical impossibility. As such, the CCAR MDT, CUPOM, is likely superior. Unfortunately, no additional PIES data are available beyond the PIES study region shown in the Fig. 10 plots, and so a Gulf-wide comparison cannot be performed. However, subjectively, correspondence between the available PIES mean SSH is better with the CCAR mean SSH than with the AVISO mean.

Figure 11 shows the CCAR (a) and AVISO (b) mean SSH maps in the same reference frame over the PIES study time period along with the difference of the two (c). Figure 11c shows that the CCAR product MDT estimate, CUPOM, may be as much as 15 cm higher than the AVISO MDT estimate, CNES/CLS 2009, in the central eastern GOM where the LC tracking contour tends to break during LCE separation. Consequently, the CUPOM mean contributes SSH signal in the CCAR and AVISO-CUPOM SSH products that keeps LCE Quick attached until after the separation of LCE Pelagic, as was determined by HMI at the time these events occurred. This is not the case for CNES/CLS 2009. In the case of Zorro, AVISO SSH shows a reattachment of the eddy to the LC at the 17-cm contour level that is not detected in the CCAR or AVISO-CUPOM datasets, which may also be attributed to the differences in the mean. In most cases, the separation dates of the CCAR and AVISO-CUPOM datasets are more similar, as is the case of LCEs Xtreme (two days apart) and Albert (1 day apart) – and both of them dissimilar to the corresponding AVISO product dates. For example, the separation dates of

Xtreme and Albert are different by 20 and 18 days and 26 and 25 days, respectively, from the LCE separation dates determined from the CCAR and AVISO-CUPOM datasets, respectively.

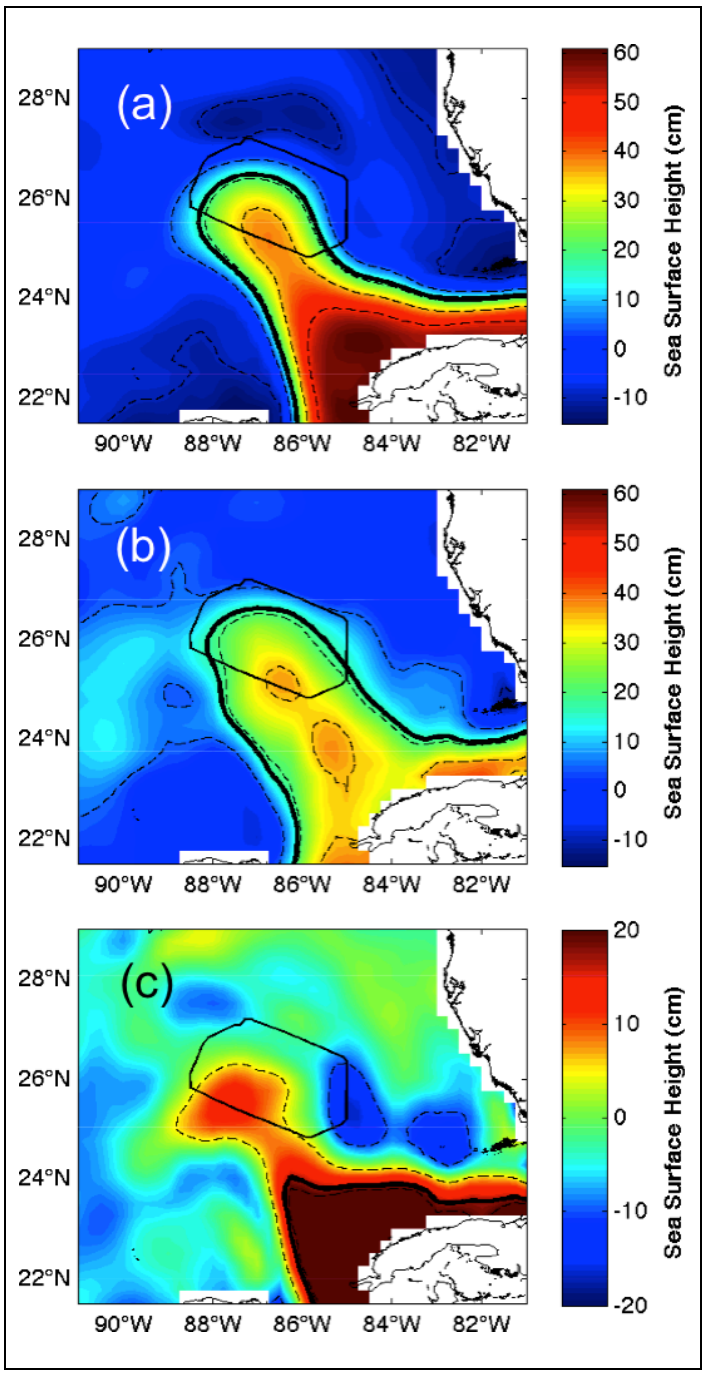

Fig. 11. Comparison of (a) the CCAR mean sea surface height map, (b) the AVISO mean sea surface height map in the CCAR reference frame, and (c) the difference of CCAR and AVISO maps over the PIES (inverted echo sounder with pressure) study time period (03 May 2009 through 23 Oct 2011). Thick black lines show the PIES study region boundary and the 17-cm Loop Current tracking contour. The dashed lines are at 15 cm increments.

Direct comparison of the LCE separation dates derived from each of the datasets shows that separation occurs later in the CCAR SSH dataset than the other two datasets for the majority of the events, sometimes even months later. Of the 28 LCE separation events identified in all three datasets at the 17-cm level, a total of 24 separation dates were later in the CCAR dataset versus those derived from the datasets based on AVISO SSHA. Thus, the "delay" is likely caused by differences in smoothing applied during objective analysis of the CCAR and AVISO SSHA datasets rather than differences in mean SSH used to produce the synthetic SSH. Several specific examples implicating the smoothing are the CCAR separation dates for LCEs Titanic, Franklin, and Icarus, which are one month, three months, and two months later, respectively, than the corresponding AVISO and AVISO-CUPOM dates even though the CCAR and AVISO-CUPOM datasets are both based on the CUPOM model mean.

In addition to LCE separation detection, the LCT uses the breaking of the 17-cm LC tracking contour for detachment detection and continuously tracks each detached LCE contour until reattachment to the LC. Dates of LCE detachment detected in the CCAR, AVISO, and AVISO-CUPOM datasets are listed in Table 6. Although separation events can be matched up relatively well between the three datasets, finding correspondence between detachment events is more difficult since the eddy typically remains detached from the LC for less than one month. The number of detachment events detected in the CCAR, AVISO, and AVISO-CUPOM datasets totaled 30, 27, and 13, respectively. The CCAR and AVISO datasets have approximately the same number of detachment events as separation events. The detachment event count for AVISO-CUPOM, however, is significantly less, indicating that when the smoother, higher amplitude AVISO SSHA is combined with the higher amplitude mean SSH field from CUPOM fewer detachments occur.

Table 6. Comparison of Loop Current eddy detachment event dates derived from CCAR, AVISO, and AVISO-CUPOM SSH datasets from January 1993 through December 2012. The HMI industry name of the LCE separation event following each date is listed also.

No.	Impending Event/ Industry Name	CCAR	AVISO	AVISO-CUPOM
1	Whopper	28 May 1993	24 May 1993	27 May 1993
2	Xtra		15 Aug 1993	22 Aug 1993
3	Zapp	11 Mar 1995	06 Mar 1995	12 Mar 1995
4	Biloxi		25 Jan 1996	04 Feb 1996
5	Creole	20 Aug 1996		
6	Creole	12 Sep 1996		
7	Creole	14 Oct 1996		
8	El Dorado		26 Jul 1997	
9	Fourchon	30 Sep 1997[a]		
10	Fourchon	02 Mar 1998		
11	Juggernaut	28 May 1999	20 Jun 1999	19 Jun 1999
12	Millennium		20 Jan 2000	
13	Millennium		27 Oct 2000	
14	Millennium	24 Jan 2001	27 Jan 2001	
15	Pelagic	10 Sep 2001		
16	Pelagic		26 Nov 2001	10 Dec 2001
17	Sargassum		26 May 2003	
18	Sargassum	14 Jul 2003	08 Jul 2003	12 Jul 2003
19	Titanic	26 Sep 2003	19 Sep 2003	25 Sep 2003
20	Titanic	31 Dec 2003		
21	Ulysses		24 May 2004	
22	Vortex	25 Feb 2005	20 Feb 2005	28 Feb 2005
23	Vortex	22 Jun 2005	17 Jun 2005	
24	Vortex	04 Aug 2005		23 Jul 2005
25	Walker		24 Sep 2005	
26	Yankee		12 Feb 2006[a]	
27	Yankee	11 Jul 2006	08 Jul 2006	16 Jul 2006
28	Yankee		19 Aug 2006	
29	Zorro	10 Apr 2007	02 Apr 2007	08 Apr 2007
30	Albert		06 Jun 2007	
31	Albert/Brazos[b]	27 Sep 2007	21 Oct 2007[a]	
32	Brazos		30 Jan 2008	
33	Cameron		21 May 2008	
34	Darwin		06 Nov 2008	29 Nov 2008
35	Ekman	05 Jul 2009		
36	Ekman	10 Aug 2009		
37	Franklin	07 Jun 2010	23 May 2010	

38	Franklin	11 Jul 2010		
39	Franklin	18 Aug 2010		
40	Hadal	27 Jul 2011		
41	Icarus	07 Nov 2011		
42	Icarus	23 Nov 2011		
43	Icarus	25 Dec 2011		
44	Jumbo	20 Jun 2012		
45	Jumbo	13 Jul 2012		

[a] Detachment occurred on same date as a separation event. See Table 5. Detachment event was associated with the following separation event, not the separation event occurring on the same day.
[b] CCAR detachment date is associated with Loop Current eddy Albert. AVISO detachment date is associated with Loop Current eddy Brazos.

Detachment events were matched up by assuming that LCE detachments detected in the datasets correspond to the same event when the dates differ by less than one month. The number of detachment events separated by less than one month occurred 12 times in the CCAR and AVISO datasets, nine times in the CCAR and AVISO-CUPOM datasets, and 12 times in the AVISO and AVISO-CUPOM datasets. There were eight times that all three datasets showed detachment events separated by less than one month. AVISO and AVISO-CUPOM show the best agreement since all but one of the AVISO-CUPOM dates were within one month of an AVISO-derived date. Even so, AVISO-CUPOM did not match AVISO 15 times. Overall the results for LCE detachment events agree less than LCE separation events indicating that detachment is sensitive to both differences in the smoothing and differences in the mean between the three data datasets.

Monthly histograms of LCE separation and detachment dates from Tables 5 and 6 are shown in Fig. 12. The histograms from all three datasets show peaks in the February/March and August/September time periods. The CCAR dataset histogram peaks are the most sharply defined, while AVISO-CUPOM peaks are least distinct. Seasonality of LCE separation will be discussed in greater detail in Chapter V. The seasonal distribution of detachment events is inconsistent among the datasets. CCAR detachments peak strongly in July – September. AVISO dates show two small peaks, one in January and one in May. The AVISO-CUPOM annual

monthly distribution is close to uniform, with a minor peak in July. Detachment events are complex processes that merit further exploration in future studies.

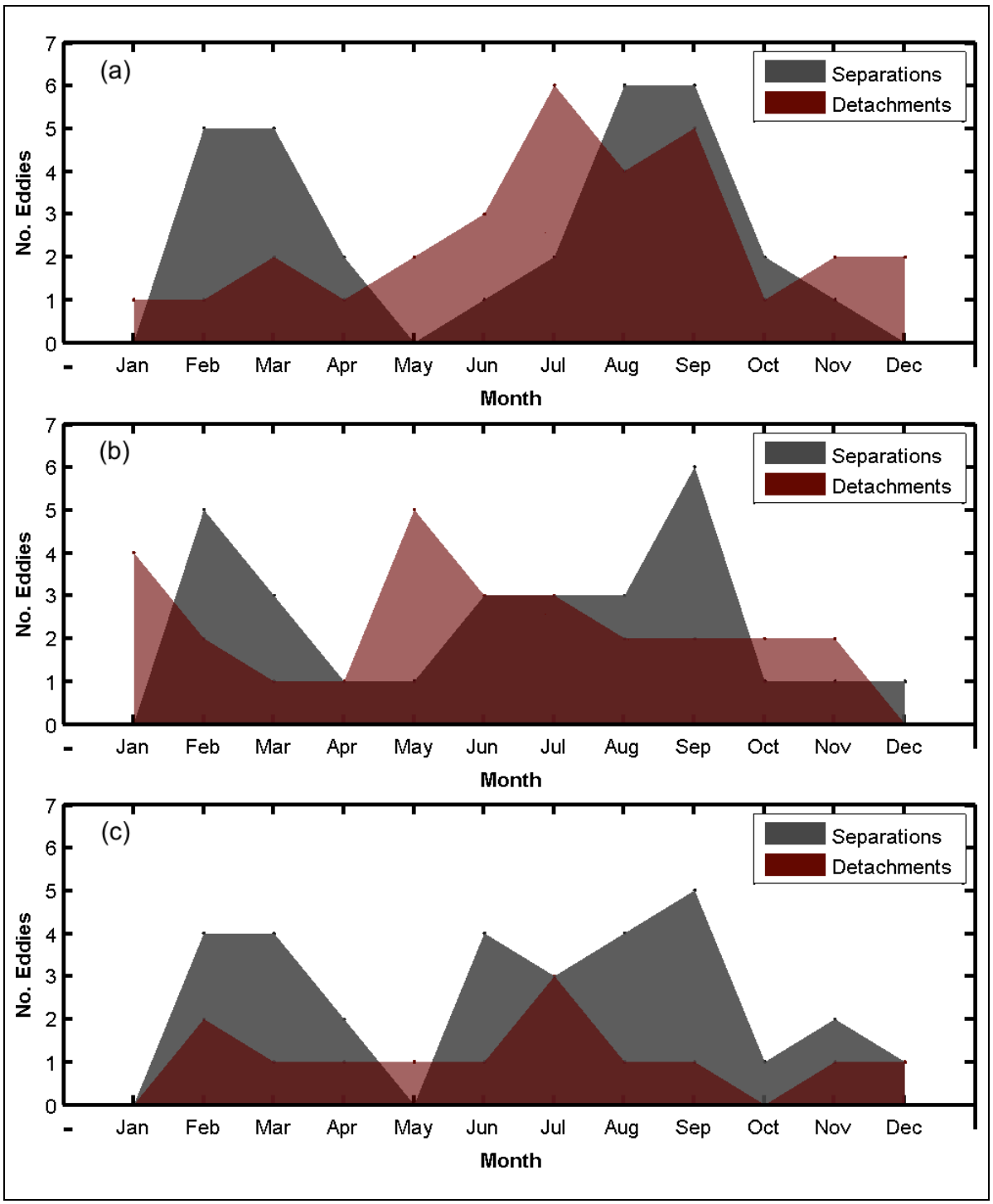

Fig. 12. Monthly histograms of separation and detachment dates (Tables 5 and 6) determined from the (a) CCAR, (b) AVISO, and (c) AVISO-CUPOM sea surface height altimetry datasets (1993-2012) by automated tracking of the 17-cm sea surface height contour.

Composite Annual Cycles of Loop Current Metrics

Figure 13 shows LC metrics computed from the CCAR dataset: area, volume, anticyclonic circulation, maximum western longitude, and maximum northern latitude. The metrics are shown both as time series and as histogram distributions over the 20-year record. Red dashed lines on the time series plots identify separation events. Identical statistics were computed for AVISO and AVISO-CUPOM datasets. Figure 14 shows monthly composite annual cycles (CACs) calculated from all three datasets for each of the metrics given above. The CAC of LC area plus the area of detached LCEs is also shown. The 95% confidence intervals (N = 20, t-score = 2.093) show that monthly means in February are statistically different than means in either October or November or both for all three data types and all six metrics. The metrics from all three datasets largely follow the same trends: a maximum in February (there are a few exceptions) and a minimum in October or November. AVISO data show the lowest values per month for all metrics with the exception of latitude; latitude CACs are similar among all three datasets. Though the AVISO dataset mean, CNES/CLS 2009, is weaker than CUPOM overall, it is comparable to the CUPOM mean on the northern boundary of the LC. CCAR data show the highest magnitudes for area, area including detachments, volume, and longitude metrics. AVISO-CUPOM has the highest in anticyclonic circulation, indicating that the AVISO SSHA objective analyses have higher geostrophic speeds parallel to the 17 cm contour when combined with the CUPOM model mean SSH.

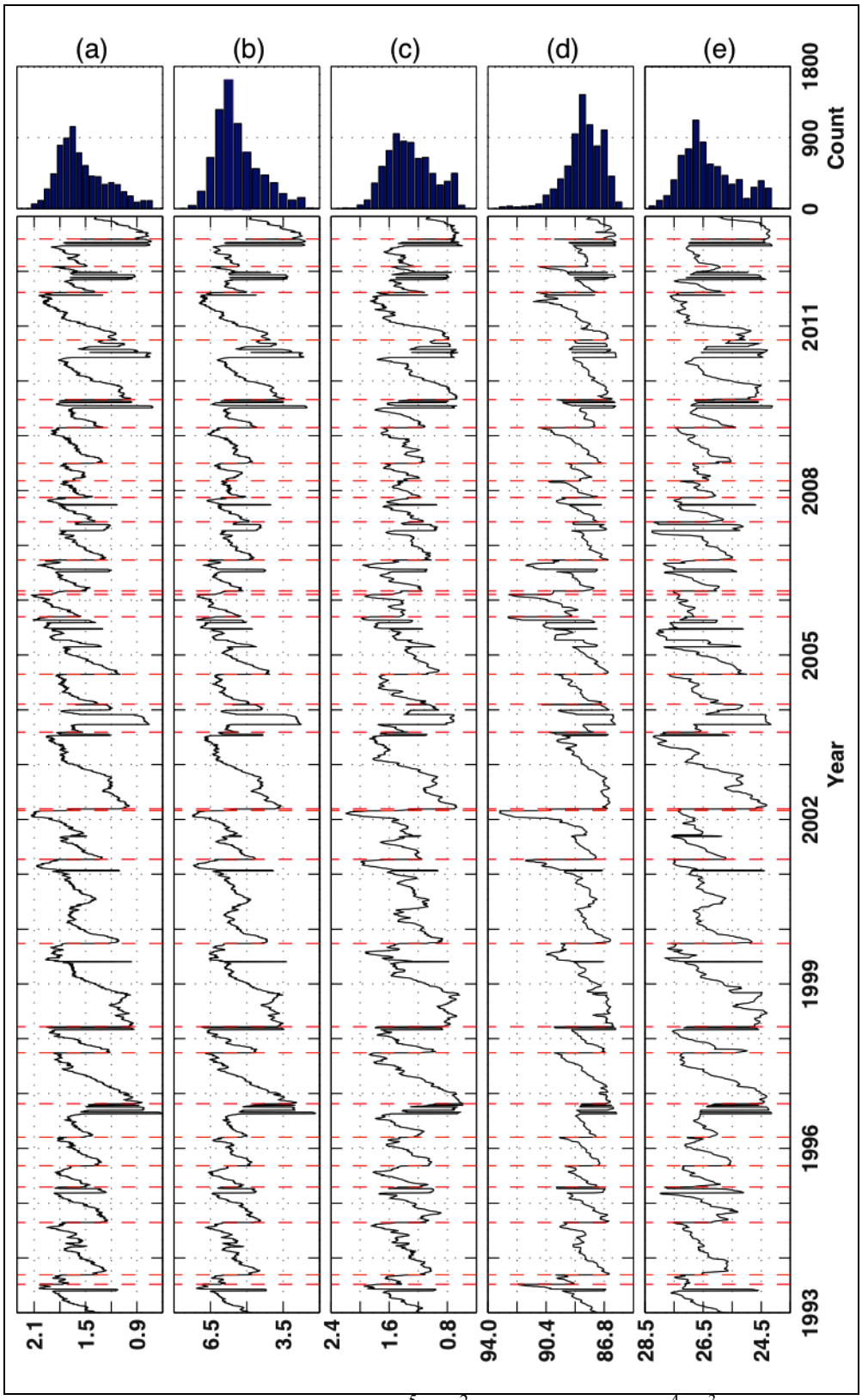

Fig. 13. Daily Loop Current (a) area (x10^5 km^2), (b) volume (x10^4 m^3), (c) anticyclonic circulation (x10^6 m^2s^{-1}), (d) westernmost longitude (°W), and (e) northernmost latitude (°N) time series and corresponding histograms, derived from CCAR sea surface height data.

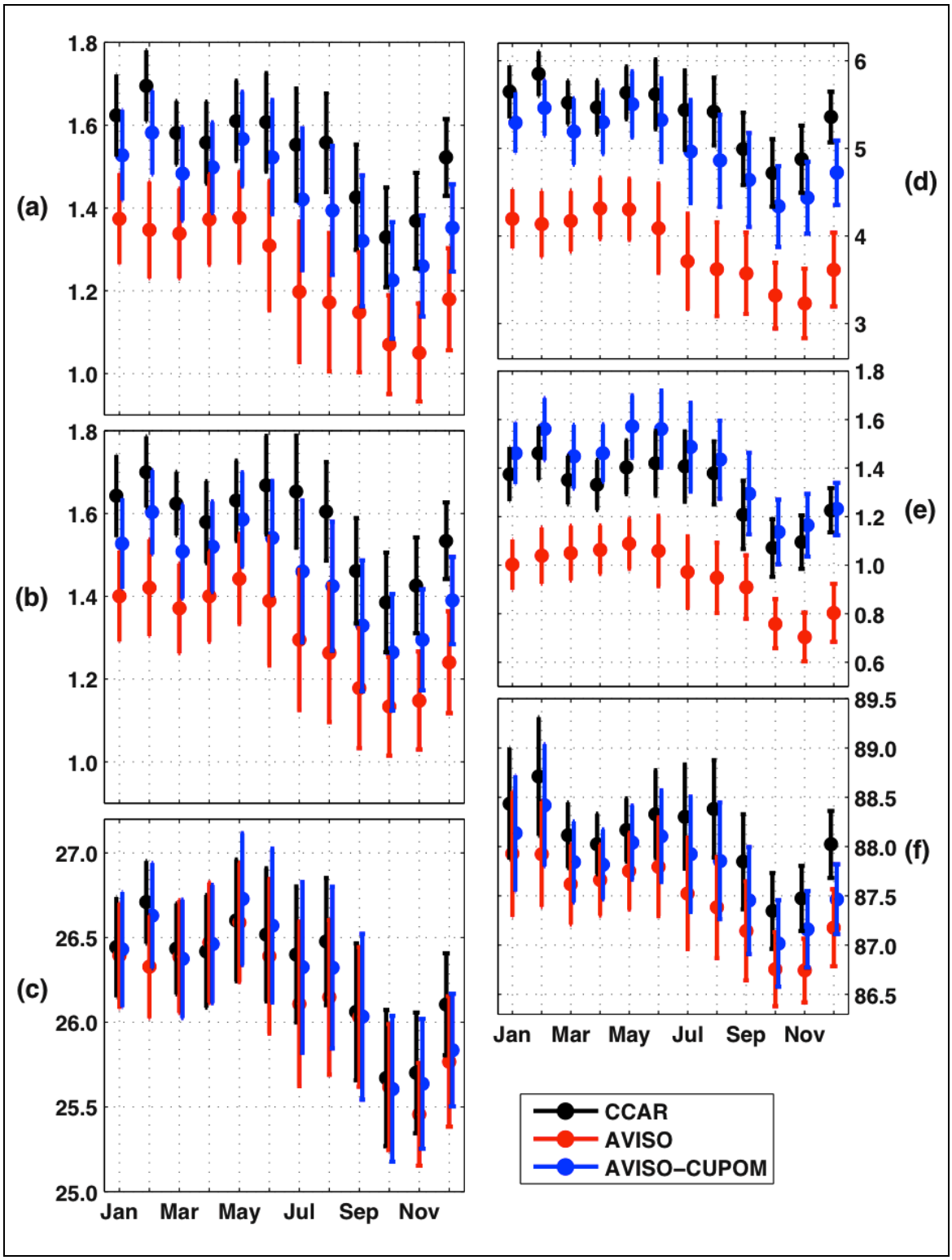

Fig. 14. Composite annual cycle plots with monthly 95% confidence intervals (N = 20, t-score = 2.093) of Loop Current (a) area (x10^5 km^2), (b) area including detachments (x10^5 km^2), (c) northernmost latitude (°N), (d) volume (x10^4 m^3), (e) anticyclonic circulation (x10^6 m^{2}s^{-1}), and (f) westernmost longitude (°W) statistics, derived from the CCAR, AVISO, and AVISO-CUPOM sea surface height datasets.

The CCAR altimetry northern boundary CAC was compared to the northern boundary CAC given in Fig. 4 of Sturges and Evans (1983), derived from in situ data. Both CACs are plotted in Fig. 15 with monthly 95% confidence intervals. Note that Sturges and Evans did not provide the 95% confidence intervals shown in Fig. 15. Instead, we computed those intervals (N = 12, t-score = 2.201 August only; N = 13, t-score = 2.179 all other months) from the monthly data points in Fig. 3 of Sturges and Evans (1983). Since the monthly data points were not true oceanographic measurements but were data interpolations, the monthly intervals on the Sturges and Evans (1983) in situ line in Fig. 15 are only estimates. Though the in situ CAC is more sinusoidal than the altimetry, both CACs are relatively high in period from March through May and low in October and November. The months of October and November are statistically different than May for both CACs.

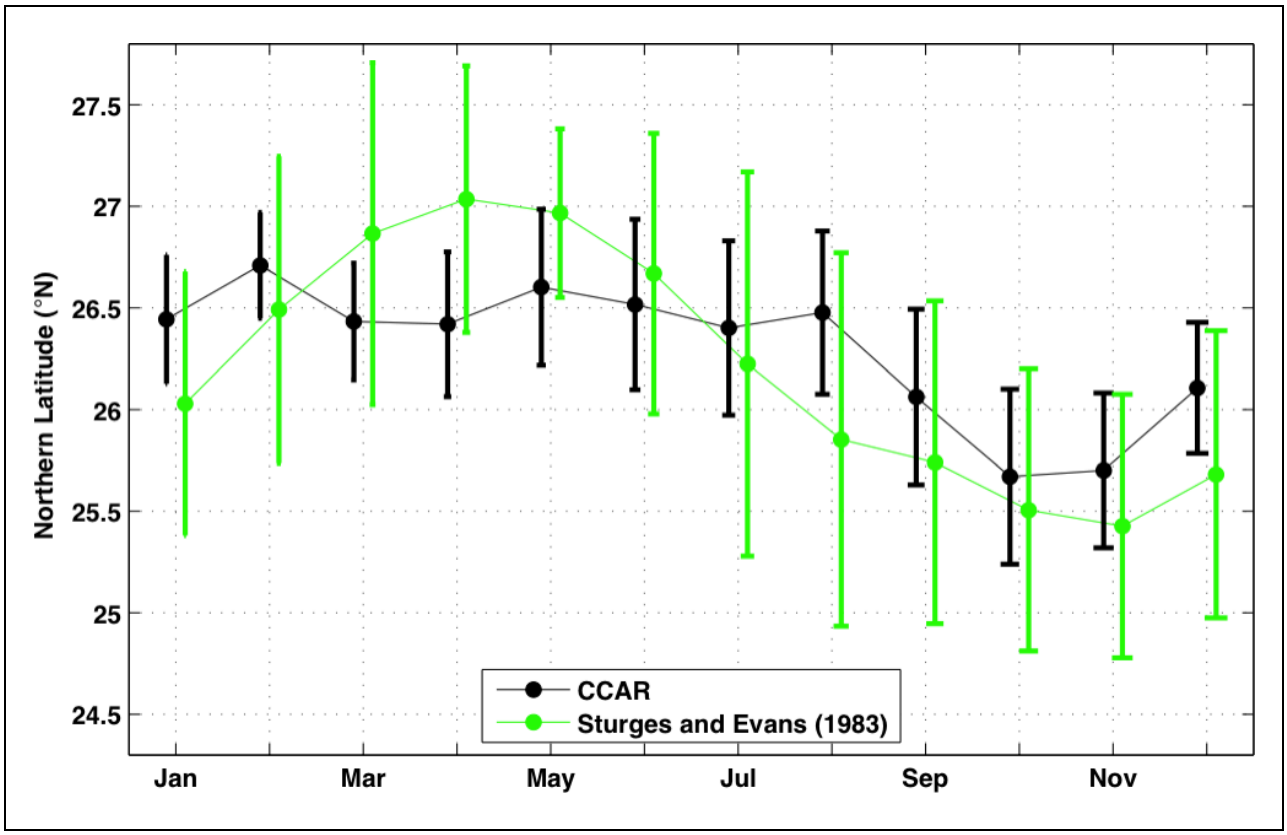

Fig. 15. Composite annual cycle plots with monthly 95% confidence intervals of Loop Current northernmost latitude derived from the CCAR satellite sea surface height dataset (N = 20, t-score = 2.093 for each month) and from the Sturges and Evans (1983) in situ dataset (N = 12, t-score = 2.201 August only; N = 13, t-score = 2.179 all other months).

Tracking Method Variations

To highlight the effects of different tracking methods on derived separation dates, Table 7 compares the AVISO reanalysis LCE separation dates given in Table 5 with LCE separation dates published in Chang and Oey (2013b), Vukovich (2012), and Lindo-Atichati et al. (2013). All LCE separation dates listed in Table 7 were derived from altimetry data; however, only Vukovich (2012) used CCAR SSH. The AVISO dataset reanalysis dates were used in the Table 7 comparison instead of CCAR or AVISO-CUPOM reanalysis dates because two of the three publications compared, Chang and Oey (2013b) and Lindo-Atichati et al. (2013), used AVISO datasets to derive separation dates. As described earlier in this chapter, the AVISO reanalysis used 1/4° daily AVISO SSH (interpolated from the weekly AVISO delayed-time product), which was demeaned in water deeper than 200 m to remove the steric signal. Tracking of separation events was performed using the LCT.

Table 7. Comparison of altimetry record Loop Current eddy separation dates from AVISO reanalysis (from Table 5), Chang and Oey (2013b), Vukovich (2012), and Lindo-Atichati et al. (2013).

No.	Industry Name	AVISO Reanalysis	Chang and Oey (2013b)	Vukovich (2012)	Lindo-Atichati et al. (2013)
21	Whopper	08 Jul 1993	Jul 1993	Jun 1993	21 Jul 1993
22	Xtra	04 Sep 1993	[a]	[a]	08 Sep 1993
23	Yucatan	19 Aug 1994	Aug 1994	Sep 1994	31 Aug 1994
24	Zapp	17 Apr 1995	Apr 1995	Mar 1995	26 Apr 1995
25	Aggie	01 Sep 1995	Sep 1995	Sep 1995	13 Sep 1995
26	Biloxi	08 Mar 1996	Mar 1996	Feb 1996	20 Mar 1996
27	Creole	20 Jul 1996	Oct 1996	Aug 1996	21 Aug 1996
28	El Dorado	25 Sep 1997	Sep 1997	Oct 1997	24 Sep 1997
29	Fourchon	12 Feb 1998	Mar 1998	Mar 1998	04 Mar 1998
30	Juggernaut	28 Sep 1999	Oct 1999	Oct 1999	29 Sep 1999
31	Millennium	29 Mar 2001	Apr 2001	Apr 2001	11 Apr 2001
	Odessa/Nansen	[b]	Sep 2001	[b]	21 Sep 2001
32	Pelagic	24 Feb 2002	Feb 2002	Mar 2002	13 Mar 2002
33	Quick	[c]	[c]	Mar 2002	17 Apr 2002
34	Sargassum	11 Aug 2003	Aug 2003	Aug 2003	20 Aug 2003
[d]	(unnamed1)				24 Sep 2003
35	Titanic	20 Dec 2003	Jan 2004	Jan 2004	24 Dec 2003
36	Ulysses	19 Aug 2004	Sep 2004	Sep 2004	01 Sep 2004
37	Vortex	11 Sep 2005	Sep 2005	Sep 2005	03 Aug 2005
38	Walker	06 Feb 2006	Mar 2006	Feb 2006	08 Mar 2006
39	Xtreme	12 Feb 2006	[e]	[e]	19 Apr 2006
[d]	(unnamed2)			Jun 2006	
40	Yankee	15 Sep 2006	Aug 2006	Oct 2006	27 Sep 2006
41	Zorro	[f]	May 2007	[f]	11 Apr 2007
42	Albert	21 Oct 2007	Oct 2007	Nov 2007	14 Nov 2007
43	Brazos	02 Mar 2008	Mar 2008	Mar 2008	[g]
44	Cameron	27 Jun 2008	Jul 2008	Aug 2008	02 Jul 2008
[d]	(unnamed3)				03 Dec 2008
45	Darwin	14 Feb 2009	Mar 2009	Mar 2009	04 Mar 2009
46	Ekman	22 Jun 2009	Jul 2009	Jul 2009	02 Sep 2009
47	Franklin	27 Jun 2010		Aug 2010	
48	Hadal	22 Jul 2011			
49	Icarus	05 Nov 2011			
50	Jumbo	28 May 2012			

[a] Chang and Oey (2012) considered Loop Current eddy Whopper and Loop Current eddy Xtra to be one event because they separated less than two months apart and reported the separation date of the first eddy only. Vukovich (2012) may have also identified Whopper and Xtra as one event.

[b] Eddy Odessa/Nansen dissipates in less than a month in the AVISO reanalysis with little westward propagation and is, therefore, not considered a separation event. Vukovich (2012) provides no specific information on the Loop Current or Loop Current eddies during this time period.
[c] Loop Current eddy Pelagic and Loop Current eddy Quick appear as a single separation event in the AVISO reanalysis, but the eddy splits into two pieces less than a week after separation. Since the two eddies separate less than two months apart. Chang and Oey (2012) considered the two eddies to be one event and reported the date of the first eddy only.
[d] The eddy appears as a detachment event in the reanalysis AVISO dates, not a separation. Reasons for why the eddy is not a separation event in the other publications are unknown.
[e] Chang and Oey (2012) does not mention a short-period separation (less than two months) to have occurred in 2006. Due to how the SSH data were processed, Loop Current eddy Walker and Loop Current eddy Xtreme may have appeared as one eddy originally such that combining the two was not necessary. Similarly, Vukovich (2012) may have also identified Walker and Xtreme as one event.
[f] Eddy Zorro appears as a detachment event in the AVISO reanalysis. Vukovich (2012) provides no specific information on the Loop Current or Loop Current eddies during this time period.
[g] The objective tracking technique in Lindo-Atichati et al. (2013) missed this event (David Lindo-Atichati, personal communication).

Analyses of LCE separation dates derived from AVISO SSH data were presented in both Chang and Oey (2012) and Chang and Oey (2013b). Chang and Oey (2012) derived a set of monthly LCE separation dates from 1993 through 2009, but did not publish the actual dates. Instead the analyzed dates were presented in the form of a monthly histogram (Fig. 1a in Chang and Oey (2012)), from which the actual year and month of each event cannot be determined. However, Chang and Oey (2013b) showed separation dates plotted as month versus year (Fig. 9a), with Chang and Oey (2012) cited as the source of the dates. According to Yu-Lin Chang (personal communication) LCE separation months were determined by manually tracking the 1.65 m SSH contour in an animation of AVISO SSH. The animation was based on the release of AVISO data just prior to that used in the preparation of this dissertation. Comparison of the event dates from 1993 through 2009 in Chang and Oey (2013b) with the annual monthly histogram in Chang and Oey (2012) shows that the Chang and Oey (2013b) dates have one more March separation event and one less June separation event. No reason was given for this discrepancy. Since the two papers use different altimeter-derived separation dates, the two datasets will be treated independently throughout the statistical discussion of LCE separation

presented in Chapter V. In the remainder of this chapter, only the dates given graphically in Chang and Oey (2013b) will be used.

Vukovich (2012) used SST, ocean color, and in situ data from various sources in addition to satellite altimetry to derive LCE separation events. Altimeter data from TOPEX/Poseidon, JASON, and ERS missions were mentioned specifically, and altimeter data from the CCAR website were cited in the acknowledgements. Lindo-Atichati et al. (2013) used a weekly 1/4° AVISO SSH dataset, which was based on the Rio and Hernandez (2004) mean dynamic topography.

For quantification of the differences in the derived LCE separation dates in Table 7, only month and year (without day-of-month, if given) were considered for each event. The numbered events that do not have dates from all four sources (event #22, 33, 39, 41, 43, 47, 48, 49, and 50) and all the unnumbered events (Odessa/Nansen, "unnamed1", "unnamed2", and "unnamed3") are ignored because one or more of the date list sources would be otherwise unrepresented. This leaves 21 "concordant" LCEs. Of those events, all dates agreed for two events (#25 and 34); there were no events where no dates agreed; the difference between the earliest and latest dates was one month for 15 events (#21, 23, 24, 26, 28, 29, 30, 31, 32, 35, 36, 37, 38, 42, and 45); and the difference was two months for four events (#27, 40, 44, and 46). Table 8 provides a summary of separation timing information for the 21 events; that is, how frequently each of the different sources had the earliest or latest separation date. For example, AVISO reanalysis dates (first row of table) were earlier than all respective dates from the other three sources (e.g. event #27) for seven events. For another seven events, the AVISO reanalysis shared the earliest separation dates with one or two of the other sources, but at least one source had a later date (e.g. event #23). For four events, the AVISO reanalysis shared the latest separation dates with one or two of the other sources, but at least one source had an earlier date (e.g. event #21). The AVISO reanalysis dates were never later than all of the respective dates from the three other sources. The three other LCE separation date sources listed in the second, third, and fourth rows of Table 8 can be

interpreted similarly. The two events where all dates agreed (#25 and 34) were excluded from the counts in the table.

Table 8. Loop Current eddy separation timing of the 19 events where each source – the AVISO reanalysis (from Table 5), Chang and Oey (2013b), Vukovich (2012), and Lindo-Atichati et al. (2013) – reported a separation event, excluding event #25 and 34.

	Earliest Alone	Earliest Shared	Sum of Earliest	Latest Shared	Latest Alone	Sum of Latest
AVISO Reanalysis	7	7	14	4	0	4
Chang and Oey (2013b)	1	4	5	11	1	12
Vukovich (2012)	3	1	4	9	4	13
Lindo-Atichati et al. (2013)	1	4	5	10	1	11

"Earliest" and "latest" sum columns are also given. The AVISO reanalysis provided the earliest separation date 14 times, far greater than the other three sources. Likewise, the AVISO reanalysis provided the latest separation date four times, far less than the others. Chang and Oey (2013b), Vukovich (2012) and Lindo-Atichati et al. (2013) are all very comparable.

Tracking procedures in all four sources were different. As discussed previously, for the AVISO reanalysis, the LC and LCEs were defined by the 17-cm contour in deepwater-demeaned AVISO SSH fields to derive the dates. Breaking of the 17 cm contour objectively established each date. Personal communication with Yu-Lin Chang indicated that Chang and Oey (2012) also identified LCEs by tracking on a fixed contour level in AVISO data. However, the steric signal was retained in the data, eddy separation periods less than or equal to two months were ignored, and each separation date may have been somewhat determined based on expert opinion. Testing suggests that retention of the steric signal would have had the affect of advancing separation events in winter and spring and delaying separation events in summer and fall in comparison to the same event dates derived without the steric signal.

To perform the tests, separation dates were objectively derived using the AVISO reanalysis dataset with (steric) and without the steric signal (nosteric) at the 13-cm level for both. (Combining AVISO mean SSH with the steric signal caused several persistent LC and LCE

tracking issues in winter and spring months at the 17-cm level that made a 17-cm level comparison invalid.) Table 9 contains reprinted AVISO reanalysis 17-cm nosteric separation dates with 13-cm nosteric dates and 13-cm steric dates for comparison. The 13-cm nosteric dates were subtracted from the 13-cm steric dates to yield delay (last column in Table 9). To interpret the delays, the events were separated into two groups, the group where events should be delayed and the group where events should be advanced. Based on the annual peak and trough of the steric signal (Sept. 15 and Mar. 16, respectively), steric signal sinusoidal inflection points were estimated to be Jun. 15 and Dec. 15. Between Jun. 15 and Dec. 15, separation events were expected to be delayed by the steric signal. Between Dec. 15 and Jun. 15, events were expected to be advanced. Expected-delayed events are highlighted in red in Table 9, while expected-advanced events are highlighted in blue. Events that behaved as expected are highlighted in green in the last column. (Event #26 was disregarded since no separation event occurred in the 13-cm steric AVISO data.) Only event #27, 49, and 50 did not behave as expected. Event #49 and 50 were both near an inflection point. Steric heating in the GOM has some interannual variation, and so the actually inflection points can fluctuate from year to year about the estimates. If the events whose nosteric separation dates occurred within plus or minus ten days (arbitrary) of the estimated inflection points are ignored (#35, 46, 49, and 50), the rms of the remaining date differences is 3.2 days. Delays are between zero and four days. Advances are between three and eight days. Notice that event #46, eliminated in the calculation, is an outlier (42 days), showing that delays (and maybe advances) caused by the steric signal can be upwards of a month. However, it seems more likely that the effect of the steric signal on events will usually be less than one week, though this result is dependent on tracking contour level. Effects of the steric signal cannot be evaluated when comparing the AVISO reanalysis (17-cm nosteric) and Chang and Oey (2013b) dates in Table 7 because Chang and Oey (2013b) does not report separation day-of-month. Since the steric signal is expected to affect an event by less than seven days, separation day-of-month is critical information in assessing the impact on individual events. Even so, for the 21 concordant events mentioned previously based on month only,

reanalysis dates are just as early or earlier than the corresponding Chang and Oey (2013b) dates for all events but one (#40). This one event has a summer/fall date, thus, contradicting the expected trend. If we assume that each Chang and Oey (2013b) date in Table 7 corresponds to the fifteenth day of the given month, the mean delay of the 21 events between the Chang and Oey (2013b) dates and the reanalysis is 13 days. Using the ten-day window about the inflection points, the events expected to be delayed have an average delay of 10.6 days. The events expected to be advanced are actually also delayed on average by an even larger value, 13.8 days. These results also contradict the expected trend since even if the events expected to be advanced are, in fact, delayed, the events should at least be less delayed than the events expected to be delayed. It seems plausible that (subjective) judgment of Chang and Oey biased some of their reported LCE separation dates by a few weeks or more.

Table 9. Comparison of Loop Current eddy separation events derived from AVISO SSH without steric signal at the 17-cm level, without steric signal at the 13-cm level, and with steric signal at the 13-cm level from January 1993 through December 2012.

No.	Industry Name	(1) AVISO 17-cm No Steric	(2) AVISO 13-cm No Steric	(3) AVISO 13-cm Steric	(2)-(1)	(3)-(2)
21	Whopper	08 Jul 1993	11 Jul 1993	13 Jul 1993	3	2
22	Xtra	04 Sep 1993	05 Sep 1993	07 Sep 1993	1	2
23	Yucatan	19 Aug 1994	21 Aug 1994	22 Aug 1994	2	1
24	Zapp	17 Apr 1995	18 Apr 1995	15 Apr 1995	1	-3
25	Aggie	01 Sep 1995	03 Sep 1995	04 Sep 1995	2	1
26	Biloxi	08 Mar 1996	11 Mar 1996	[a]	3	
27	Creole	20 Jul 1996	24 Jul 1996	24 Jul 1996	4	0
28	El Dorado	25 Sep 1997	27 Sep 1997	29 Sep 1997	2	2
29	Fourchon	12 Feb 1998	16 Feb 1998	12 Feb 1998	4	-4
30	Juggernaut	28 Sep 1999	30 Sep 1999	04 Oct 1999	2	4
31	Millennium	29 Mar 2001	31 Mar 2001	27 Mar 2001	2	-4
32	Pelagic	24 Feb 2002	25 Feb 2002	24 Feb 2002	1	-1
33	Quick	[b]	[b]	[b]		
34	Sargassum	11 Aug 2003	13 Aug 2003	16 Aug 2003	2	3
35	Titanic	20 Dec 2003	22 Dec 2003	21 Dec 2003	2	-1
36	Ulysses	19 Aug 2004	20 Aug 2004	22 Aug 2004	1	2
37	Vortex	11 Sep 2005	12 Sep 2005	14 Sep 2005	1	2
38	Walker	06 Feb 2006	09 Feb 2006	05 Feb 2006	3	-4
39	Xtreme	12 Feb 2006	15 Feb 2006	11 Feb 2006	3	-4
40	Yankee	15 Sep 2006	17 Sep 2006	19 Sep 2006	2	2
41	Zorro	[c]	[c]	[c]		
42	Albert	21 Oct 2007	09 Nov 2007	11 Nov 2007	19	2
43	Brazos	02 Mar 2008	09 Mar 2008	01 Mar 2008	7	-8
44	Cameron	27 Jun 2008	28 Jun 2008	30 Jun 2008	1	2
45	Darwin	14 Feb 2009	17 Feb 2009	14 Feb 2009	3	-3
46	Ekman	22 Jun 2009	25 Jun 2009	06 Aug 2009	3	42
47	Franklin	27 Jun 2010	09 Aug 2010	13 Aug 2010	43	4
48	Hadal	22 Jul 2011	23 Jul 2011	26 Jul 2011	1	3
49	Icarus	05 Nov 2011	17 Dec 2011	18 Dec 2011	42	1
50	Jumbo	28 May 2012	07 Jun 2012	13 Jun 2012	10	6

General Notes: the last two columns show resulting event separation delay (in days) when changing the tracking contour from 17-cm to 13-cm and when changing from data without to data with the steric signal. The 13-cm events that were expected to be delayed by the steric signal are highlighted in red, while events that were expected to be advanced are highlighted in blue. Events that behaved as expected for either case are highlighted in green in the last column.

[a] A very small eddy separates from the Loop Current for this event on Mar. 4, too small to be considered a Loop Current eddy.

[b] In all three versions of the AVISO data, Eddies Pelagic and Quick separate from the Loop Current as one eddy, though they split from each other days after separation.
[c] Eddy Zorro appears as a detachment event in all three versions of the AVISO data.

If the AVISO reanalysis were performed on a lower tracking contour than 17 cm throughout, it would have had the affect of delaying all separation event dates. The second to last column in Table 9 shows that tracking the LC at the 13-cm level in nosteric AVISO data delayed every separation event compared to tracking at the 17-cm level. Delays ranged from one to 43 days. The mean delay is 6.1 days, and the median is 2 days. Four delays were greater than one week (#42, 47, 49, and 50). Two delays were greater than one month (#47 and 49). Unfortunately, effects of changing contour level are unpredictable and event-dependent. Even so, re-derived event dates from lower-contour tracking may be more consistent with Chang and Oey (2013b) dates.

Vukovich (2012) provided no explicit information as to how LCEs were tracked, although specified lifetime and diameter criteria were mentioned, as discussed in Chapter III. Given that GOES SST, SeaWiFS and MODIS ocean color, and CCAR altimetry were used in combination, event dates may have been derived entirely subjectively. Vukovich (2012) dates were later than reanalysis dates for 14 events and earlier for only three events. Lindo-Atichati et al. (2013) used maximum gradient in AVISO SSH fields to determine the boundaries of the LC and LCEs. Removing the steric signal would have had no affect on separation dates since a constant offset applied to a SSH field would not affect the gradient calculation. Lindo-Atichati et al. (2013) dates were later than reanalysis dates for ten events and earlier for only one event. Combinations of the contour level and SSH gradient techniques described are likely to yield similar results. For instance, Chassignet et al. (2013) tracked the LC and LCEs in HYbrid Coordinate Ocean Model (HYCOM) data using a predictor-corrector method in which SSH contour level defined the first estimation of LC and LCE boundaries and SSH gradient improved the first estimation. Separation dates derived using the predictor-corrector routine were only slightly later than dates found using SSH contour level alone, as implemented in the LCT.

Tracking techniques applied in the LCT and in Chang and Oey (2012) and Lindo-Atichati et al. (2013) are Eulerian approaches to separation detection. The techniques use SSH or SSH gradient at specified grid points to track LC and LCE positions at every time step following streamlines or the instantaneous velocity field. Because ocean flows are quasi-geostrophic, they evolve slowly enough that streamlines well approximate pathlines of the flowfield. Since the flow is actually unsteady, pathlines do cross streamlines, and the fluid contained within a closed streamline is not conserved. Nevertheless, tracking of a SSH contour or velocity fronts can identify separation dates relatively accurately. It could be argued that the Vukovich (2012) tracking technique, although subjective, is Lagrangian through the use of the time evolving SST and ocean color patterns in the satellite images as a Lagrangian tracer. However, neither SST nor chlorophyll concentration are conserved quantities, so a subjective technique based on satellite imagery is at best a mixed Eulerian/Lagrangian approach that relies heavily on expert judgment. In contrast, explicit Lagrangian tracking focuses on specific fluid parcels moving with the flow rather than Eulerian flowfield variables specified at fixed points in space. For example, Andrade-Canto et al. (2013) presented a method for finding manifolds – Lagrangian coherent structures (LCS) – in velocity fields using finite-time Lyapunov exponents. These LCSs are material boundaries that follow parcel pathlines through a flow. In the case of the LC, LCSs can show whether the main circulation coming into the GOM through the Yucatan Channel is flowing northward around a presently detached LCE or is cutting immediately east to exit through the Florida Straits. A northward flow typically means that the detached LCE will reattach, but an eastward flow means that the LCE is separated. Whereas Eulerian methods often require more than a month of data beyond separation of an LCE to confirm that the LCE is truly separated and not just detached from the LC, the technique given in Andrade-Canto et al. (2013) confirms separation more promptly. Even so, separation dates derived using this Lagrangian technique, which is significantly more complicated to implement, are comparable to dates derived from Eulerian tracking techniques.

Closing

The information presented in this chapter and in Chapter III demonstrates the effects some of the many possible data processing and tracking methods have on ultimate LCE separation dates. LC metric results in Fig. 14 and Fig. 15 show that statistical significance is robust regardless of altimetry product. Various pre-altimetry and altimetry event date records including the records shown in Tables 3, 5, and 7 will be examined in Chapter V to determine what impact those methods have on seasonal manifestation. However, steric signal and tracking contour level findings in this chapter will not be further investigated. Though it was necessary to examine steric signal effects to better understand results in Chang and Oey (2013b), Table 9 results suggest that the steric signal will typically have minimal impact on separation dates. Small variations in objective tracking contour level may have a greater impact on separation dates, though still likely minimal in most cases. Therefore, steric signal and contour level variation effects are excluded from Chapter V analyses. Detachment events (Table 6) are excluded as well since their interpretation is unclear, though they may exhibit seasonality in some way. It was not my intent in the current chapter to present a comprehensive survey of data processing and tracking techniques but rather to justify the methods used in this dissertation to show that the LC has seasonal preference.

CHAPTER V

STATISTICAL ANALYSIS OF LOOP CURRENT SEASONALITY

Recent studies (Alvera-Azcárate et al., 2009; Forristall Ocean Engineering, 2009a; 2009b; Leben and Hall, 2010; Chang and Oey, 2012; Lindo-Atichati et al., 2013) have suggested that the LC may exhibit seasonality in the timing of LCE separation. The 95% confidence intervals in Fig. 14 of this dissertation similarly support that there are two distinct LC seasons, one of maximums and one of minimums, though the extents of the two are not clearly defined. In the current chapter, a number of pre-altimetry, altimetry, and combined (both pre-altimetry and altimetry) datasets were compared to assess seasonality and the statistical significance and boundaries of seasons when LCE separation is most likely.

Loop Current Eddy Separation Event Statistical Significance Testing

Statistical χ^2 tests were performed on the reanalysis pre-altimetry dates (N=20) shown in Table 3 to assess the null hypothesis that LCE separation dates come from a uniform distribution. Since expected bin counts using monthly binning would be too low to test for statistical significance, the data were binned quarterly (not shown) to increase expected counts in each three-month bin to five. Bins larger than three months, e.g. four months or six months, can begin to conceal seasonality and are, therefore, undesirable. Quarterly binning proceeded in three different ways: first with the bins Feb-Apr, May-Jul, Aug-Oct, and Nov-Jan (binning1), second with the bins Jan-Mar, Apr-Jun, Jul-Sep, and Oct-Dec (binning2), and third with the bins Mar-May, Jun-Aug, Sep-Nov, and Dec-Feb (binning3). Results from the χ^2 tests indicate that at the 95% confidence level, the null hypothesis is rejected for binning1 and binning2 (Ott and Longnecker, 2001), implying that separation timing is seasonal. The tests of binning3 did not yield statistical significance at the 95% confidence level. Statistical significance can be a function of bin boundaries and size; therefore, suppression of seasonality in at least one of the three-month binning schemes is expected. There are too few pre-altimetry dates from Vukovich (2012) in Table 3 (N=16) to statistically determine whether the separation dates are from a uniform distribution. The χ^2 distribution is not well approximated whenever 20% or more of the bins have expected values less than five (Ott and Longnecker, 2001). Vukovich (2012) LCE separation dates fail this requirement since all four bins have an expected value of four. However, Table 3 contains only a portion of the pre-altimetry dates given in Vukovich (2012) from 1978 through 1992. If all pre-altimetry separation dates from Vukovich (2012) from 1972 through 1992 are tested (N=23), the expected bin counts are sufficient, but none of the three binnings show statistical significance of seasonality.

Monthly-binned histograms of the pre-altimetry reanalysis dates and the pre-altimetry dates from Vukovich (2012) listed in Table 3 are shown in Figs. 16a and 16b, respectively. The blue dashed line in each subplot represents the average number of LCEs to separate per month, per year. Randomization tests were performed on both datasets to determine which peaks in the

histograms, if any, were significant. Reanalysis LCE separation event testing proceeded as follows. The events were randomly reordered 100,000 times, forming 100,000 separation date sequences. Each sequence used each original separation event exactly once (selection without replacement) so that every sequence had exactly 20 events, just as the original sequence, and the separation periods and duration of the record were preserved. The initial day of the year to start each sequence was also randomized. Then all 100,000 sequences were binned by month to produce a distribution of LCE separation counts for each month. Significance was determined from the random outcomes. For example, if there were no seasonal signal in the original reanalysis LCE separation sequence, then each of the 12 monthly counts represented by bars in the original histogram (Fig. 16a) would be frequently replicated among the 100,000 random sequences. However, Fig. 16a shows that the count in August is significant. The value 1.7% above the bar means that of all 100,000 sequences, only 1.7%, or 1,700, of the randomized sequences contained, in this case, five or more separation events in August. Any count with a value of 5% or less was considered significant at the 95% confidence level. The only significant month of separation in the reanalysis dates is August. Even so, one month is enough to indicate that there is some seasonal preference in the reanalysis pre-altimetry dates. The same randomization testing was performed on the pre-altimetry Vukovich (2012) dates in Fig. 16b and on the complete pre-altimetry record from 1972 through 1992 in Vukovich (2012) (not plotted as histogram). There were no significant months found, indicating no seasonality in the Vukovich (2012) pre-altimetry dates. Traditional histograms of Figs. 16a and 16b are shown in Figs. 17a and 17b for comparison.

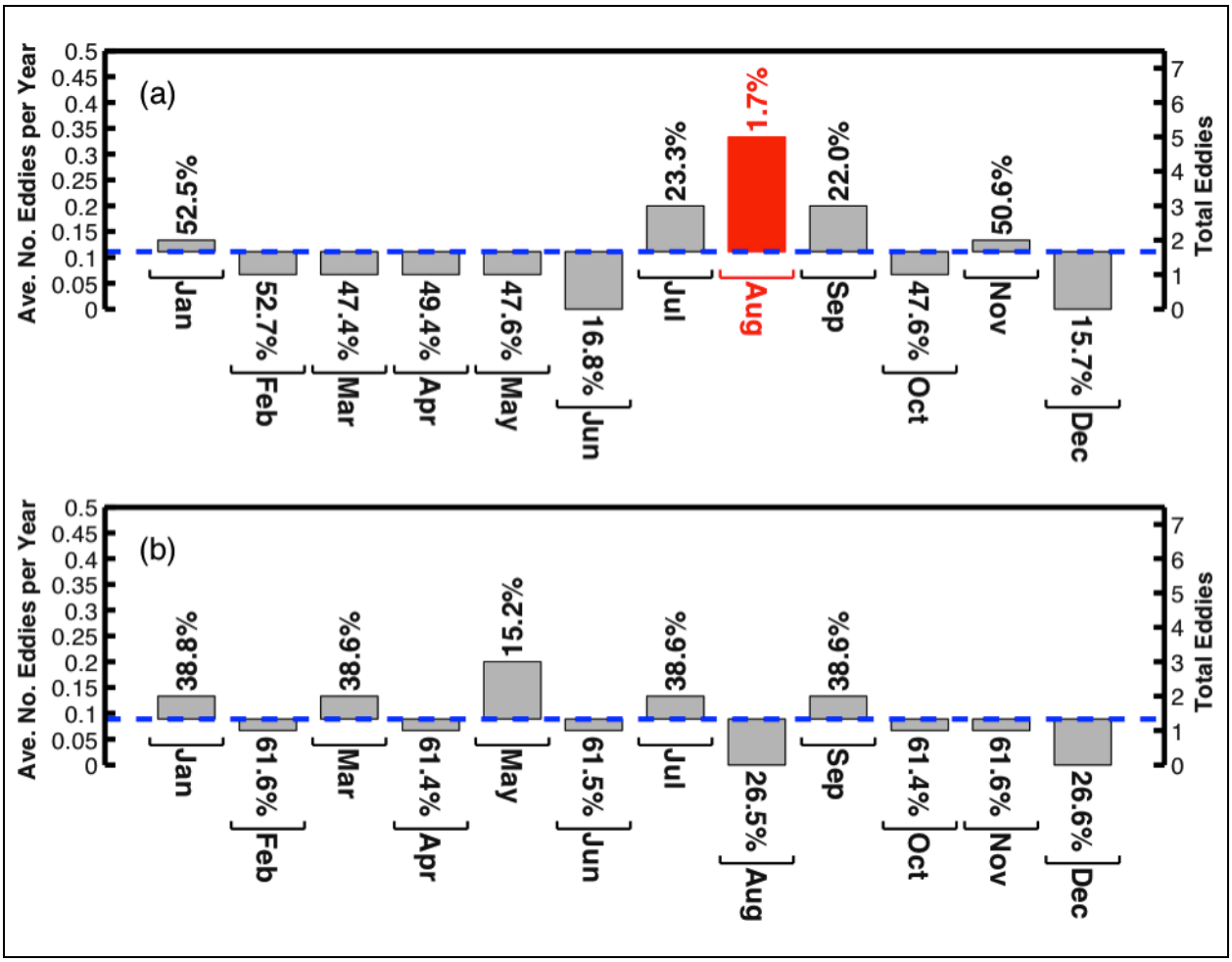

Fig. 16. Loop Current eddy separation dates (Table 3) binned monthly from (a) reanalysis and (b) Vukovich (2012) pre-altimetry (1978-1992). Blue dashed lines show the average number of Loop Current eddies to separate per month, per year. The percent likelihood of observing a Loop Current eddy count as extreme or more extreme by chance is displayed for each monthly bar. All bars at 5% or less are considered significant at the 95% confidence level and colored red.

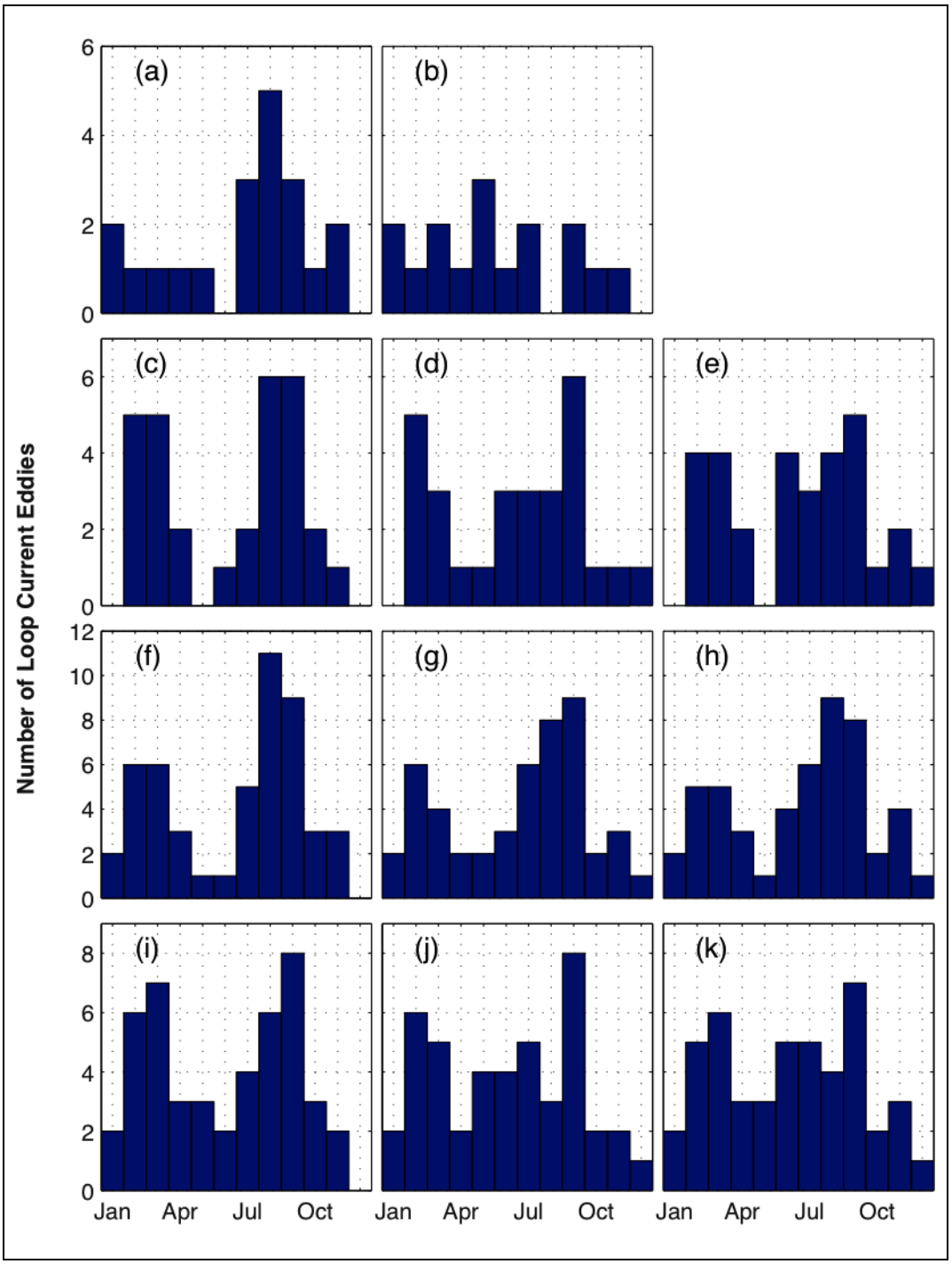

Fig. 17. Monthly binned histograms of pre-altimetry, altimetry, and combined Loop Current eddy separation date datasets. First row: (a) reanalysis and (b) Vukovich (2012) pre-altimetry separation dates (1978-1992) from Table 3. Second row: (c) CCAR, (d) AVISO, and (e) AVISO-CUPOM altimetry (1993-2012) from Table 5. Third row: reanalysis pre-altimetry (1978-1992) and (f) CCAR, (g) AVISO, and (h) AVISO-CUPOM altimetry (1993-2012) combined. Fourth row: Vukovich (2012) pre-altimetry (1978-1992) and (i) CCAR, (j) AVISO, and (k) AVISO- CUPOM altimetry (1993-2012) combined.

These two types of statistical tests, χ^2 and randomization, complement each other. The χ^2 test indicates whether a distribution of LCE separation dates exhibits statistically significant seasonality; if the dates are not from a uniform distribution, then the distribution exhibits seasonality. However, the χ^2 test does not indicate in which month or season LCE separation is more likely or less likely to occur. Conversely, if the randomization test shows any months as being significant, the test not only indicates that the respective dates exhibit seasonality, but also provides information on the seasonal preference. If no months are significant, then the randomization test is a null result, and no information on seasonality is obtained. Table 10 summarizes results of the χ^2 and randomization tests on the pre-altimetry reanalysis and Vukovich (2012) datasets along with results of the same tests performed on additional datasets. Of all pre-altimetry datasets shown, the reanalysis LCE separation date list is the only one to show a statistically significant peak and is one of two lists to show significant χ^2 test results. The other list with a significant χ^2 test is given in Sturges (1994). Sturges (1993), Sturges (1994), and Vukovich (2012) dates were all based on dates in Vukovich (1988), which had too few events to make the χ^2 test valid. Vukovich (2012) continued the list presented in Vukovich (1988) through the pre-altimetry time period. Note that the dates in Vukovich (2012) over the longer time period from 1972 though 1992 exhibited no statistically significant seasonality by either test. Because seasonality was not evident in Vukovich (1988), seasonality was indiscernible until the altimetry record became sufficiently long to overcome the lack of seasonality in these earlier published pre-altimetry LCE separation dates.

Table 10. Results of significance testing of various sources of Loop Current eddy separation event dates.

	χ^2 Test			Randomization Test
Source	bin1	bin2	bin3	Significant Months
PRE-ALTIMETRY				
Reanalysis, 1978-1992	x	x		Aug(+)
Sturges (1993), 1965-1990				None
Sturges (1994), 1973-1993[a]		x	x	None
Vukovich (1988), 1973-1987	N/A			None
Vukovich (2012), 1972-1992				None
Vukovich (2012), 1978-1992	N/A			None
ALTIMETRY				
CCAR, 1993-2012	x	x		Aug(+), Sep(+)
AVISO, 1993-2012[b]	x	x		Sep(+)
AVISO-CUPOM, 1993-2012	x	x		None
Alvera-Azcárate et al. (2009), 1993-2006[c]	x	x		Mar(+), Sep(+)
Chang and Oey (2012), 1993-2009[d]	x	x		Sep(+)
Chang and Oey (2013b), 1993-2009	x	x	x	Mar(+), Sep(+)
Leben (2005), 1993-2004	N/A			Sep(+)
Lindo-Atichati et al. (2013), 1993-2009	x	x	x	Sep(+)
Vukovich (2012), 1993-2010	x	x		Mar(+)
COMBINED				
Reanalysis, 1978-1992+CCAR, 1993-2012	x	x	x	Aug(+), Sep(+), Dec(-)
Reanalysis, 1978-1992+AVISO, 1993-2012[e]	x	x	x	Aug(+), Sep(+)
Reanalysis, 1978-1992+ AVISO-CUPOM, 1993-2012	x	x	x	Aug(+), Sep(+)
Vukovich (2012), 1978-1992+CCAR, 1993-2012	x	x		Sep(+), Dec(-)
Vukovich (2012), 1978-1992+ AVISO, 1993-2012[f]	x	x		Sep(+)
Vukovich (2012), 1978-1992+ AVISO-CUPOM, 1993-2012		x		None
Chang and Oey (2012), 1974-2009[d]	x	x	x	Dec(-)
Chang and Oey (2013b), 1974-2009	x	x	x	Mar(+), Dec(-)
Sturges and Leben (2000), 1973-1999	x	x		None
Vukovich (2012), 1972-2010	x	x		Mar(+), Dec(-)

General Notes: for the χ^2 tests, binning1 (bin1) used month groupings Feb-Apr, May-Jul, Aug-Oct, and Nov-Jan, binning2 (bin2) used Jan-Mar, Apr-Jun, Jul-Sep, and Oct-Dec, and binning3 (bin3) used Mar-May, Jun-Aug, Sep-Nov, and Dec-Feb. "x" means the distribution was not uniform at the 95% confidence level. "N/A" means there are not enough separation events for the test to be valid. For the randomization tests, months with "+" signs are peaks, and months with "-" signs are troughs.

[a] Sturges (1994) presented one separation event occurring in 1993, beyond the limits of the pre-altimetry "era" ending in 1992. Even so, most of the dates in Sturges (1994) are pre-altimetry dates, and so Sturges (1994) is placed in the pre-altimetry category. Sturges (1994) was submitted before the end of 1993. Thus, the study year 1993 was not completed.
[b] In the AVISO date list (Table 5), two LCEs shed in February 2006. However, if those two events are combined into one, the results of the χ^2 tests and randomization test remain the same.
[c] Alvera-Azcárate et al. (2009) analyzed data ending in February 2006. Thus, the study year 2006 was not completed. Alvera-Azcárate et al. (2009) noted two separation events to have occurred on the same day, Mar. 6, 2002. If those two events are combined into one, the results of the χ^2 tests remain the same, but the March peak is no longer significant.
[d] No dates were explicitly given in Chang and Oey (2012), but I know the dates are very similar to dates in Chang and Oey (2013b). All dates in Chang and Oey (2013b) were taken to be dates in Chang and Oey (2012) "as is", with the exception of three: Chang and Oey (2013b) dates in March 1996, April 1995, and May 2007 were included in Chang and Oey (2012) after each being shifted forward a month to ultimately match the altimetry histogram in Chang and Oey (2012). See further explanation in Chapter IV. Since the estimated Chang and Oey (2012) dates can be binned monthly to match the histogram in Chang and Oey (2012), the χ^2 test results included herein are valid even if the exact estimated dates are wrong. However, the corresponding randomization test will be impacted by incorrect dates.
[e] In the AVISO date list (Table 5), two LCEs shed in February 2006. However, if those two events are combined into one, the results of the χ^2 and randomization tests on the combined reanalysis/AVISO date set remain the same.
[f] In the AVISO date list (Table 5), two LCEs shed in February 2006. However, if those two events are combined into one, the results of the χ^2 and randomization tests on the combined Vukovich (2012)/AVISO date set remain the same.

Figure 18a, Fig. 18b, and Fig. 18c display, respectively, the CCAR (N=30), AVISO (N=28), and AVISO-CUPOM (N=30) altimetry separation dates from Table 5, binned monthly. (The same separation date lists are plotted as traditional histograms in Fig. 17c, 17d, and 17e, respectively.) All three histograms have bimodal distributions. The CCAR histogram is strongly bimodal, while the AVISO-CUPOM shows weak bimodality, with one peak in the late winter/early spring (February/March) and the other in late summer/early fall (August/September). Henceforth, these peaks will be called the "spring" and "fall" seasons since they represent time periods of preferred LCE separation and reach maximums near the spring and fall equinoxes. Randomization tests performed on the three datasets show that August and September are significant months in the CCAR dataset, and August is significant in the AVISO dataset. None of the other months' eddy counts in any of the three histograms are significantly

different from the mean. There are no significant months in the AVISO-CUPOM dataset. These results indicate that the spring peak is not significant; although, it may become significant with a longer satellite altimeter-derived time series based on more observations of separation events if the statistics remain stationary. The fall peak is likely significant; however, Fig. 18c demonstrates that different versions of SSHA and mean SSH do affect the significance of the fall peak. Although CCAR and AVISO-CUPOM datasets both use the same mean SSH, the fall season is significant in the CCAR seasonal distribution but not in the AVISO-CUPOM seasonal distribution. Differences in SSHA processing methods between CCAR and AVISO resulted in smaller and larger spreads, respectively, of separation dates around the center of the fall season. In addition, AVISO dates were clustered closer to the fall center than the AVISO-CUPOM dates, indicating that both SSHA processing and mean SSH impact the overall spread of the distribution. If the AVISO-CUPOM dates were the only dates available for analysis, there would have been insufficient evidence to prove seasonality based on the randomization test. With the null hypothesis that the counts come from a uniform distribution, χ^2 tests show that the null hypothesis can be rejected at the 95% confidence level for all three subplots with binning1 and binning2, indicating a seasonal preference. Thus, seasonality is also confirmed in the AVISO-CUPOM dataset although the preferred seasons cannot be identified.

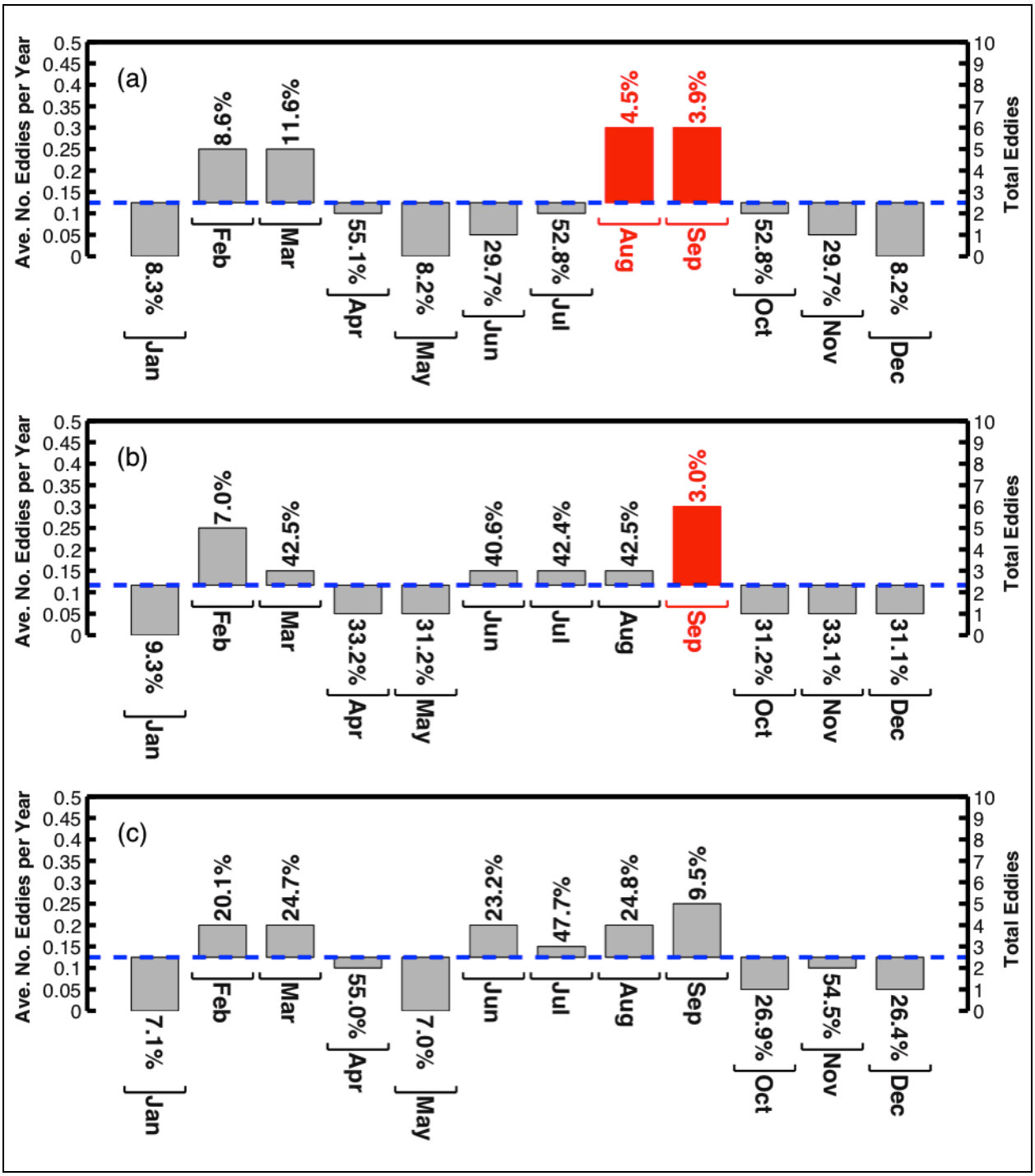

Fig. 18. Loop Current eddy separation dates (Table 5) binned monthly from (a) CCAR, (b) AVISO, and (c) AVISO-CUPOM altimetry (1993-2012). Blue dashed lines show the average number of Loop Current eddies to separate per month, per year. The percent likelihood of observing a Loop Current eddy count as extreme or more extreme by chance is displayed for each monthly bar. All bars at 5% or less are considered significant at the 95% confidence level and colored red.

Results of the statistical tests performed on the CCAR, AVISO, and AVISO-CUPOM datasets are given in Table 10 along with results of testing on additional LCE separation dates derived from altimetry. September is a significant month in all date sets except for AVISO-CUPOM, as mentioned before, and the Vukovich (2012) dates from 1993 through 2010. Vukovich (2012) was the only source in the Table 10 altimetry list to rely also on SST and ocean color data besides altimetry to derive dates during the altimetry time period, which may have resulted in event dates different enough from other sources to suppress fall season significance. However, March was a significant month in the Vukovich (2012) altimetry dates. This month was also significant in Alvera-Azcárate et al. (2009) and Chang and Oey (2013b), but not Chang and Oey (2012). Lack of significance of the March peak in Chang and Oey (2012) illustrates the extreme sensitivity of significance testing to small changes in separation dates. (Please refer to Chapter IV and Table 10 notes for details on the Chang and Oey (2012) dates.)

The pre-altimetry reanalysis date list is nearly consistent with the majority of the altimetry date lists because of its significant peak in August, close to the significant altimetry September peak. This rough agreement serves as additional evidence that the LCE separation dates determined by the reanalysis presented in this dissertation are likely more accurate than the Vukovich (2012) dates. Overall, the Vukovich (2012) list should be considered an "outlier" in the presence of the statistical stationarity exhibited by the reanalysis over the available satellite record since 1978.

Figure 19 displays the three altimetry date sets CCAR, AVISO, and AVISO-CUPOM paired with the pre-altimetry reanalysis dates. (Traditional histograms of the three combined lists are in Figs. 17f, 17g, and 17h, respectively.) All three combined lists have significant peaks in August and September including the combined list using the AVISO-CUPOM dates shown in Fig. 19c. December has become a significant trough in the pre-altimetry/CCAR combined histogram (Fig. 19a). Figure 20 displays the three altimeter-derived LCE separation date sets paired with the Vukovich (2012) pre-altimetry dates from 1978 through 1992. (Traditional histograms of the three combined lists are in Figs. 17i, 17j, and 17k, respectively.) The August

peak that appeared in the CCAR altimetry dates alone (Fig. 18a) is no longer significant in the combined date list in Fig. 20a. However, December has become a significant trough. Other months besides March, August, September, and December may also become significant as more separation events occur and are added to the record. The September peaks in the CCAR and AVISO altimetry lists, Figs. 18a and 18b, are still significant in the combined lists, Fig. 20a and 20b. No peaks are significant in the AVISO-CUPOM combined list, Fig. 20c, which is not unexpected since neither the Vukovich (2012) pre-altimetry dates (Fig. 16b) nor the AVISO-CUPOM altimetry dates (Fig. 18c) had any significant peaks. The Vukovich (2012) pre-altimetry dates tend to suppress seasonal preference when combined with the altimeter record, whereas the pre-altimetry reanalysis dates tend to accentuate seasonality. Table 10 presents significance testing results for all six combinations of LCE separations dates along with results from published dates by other studies.

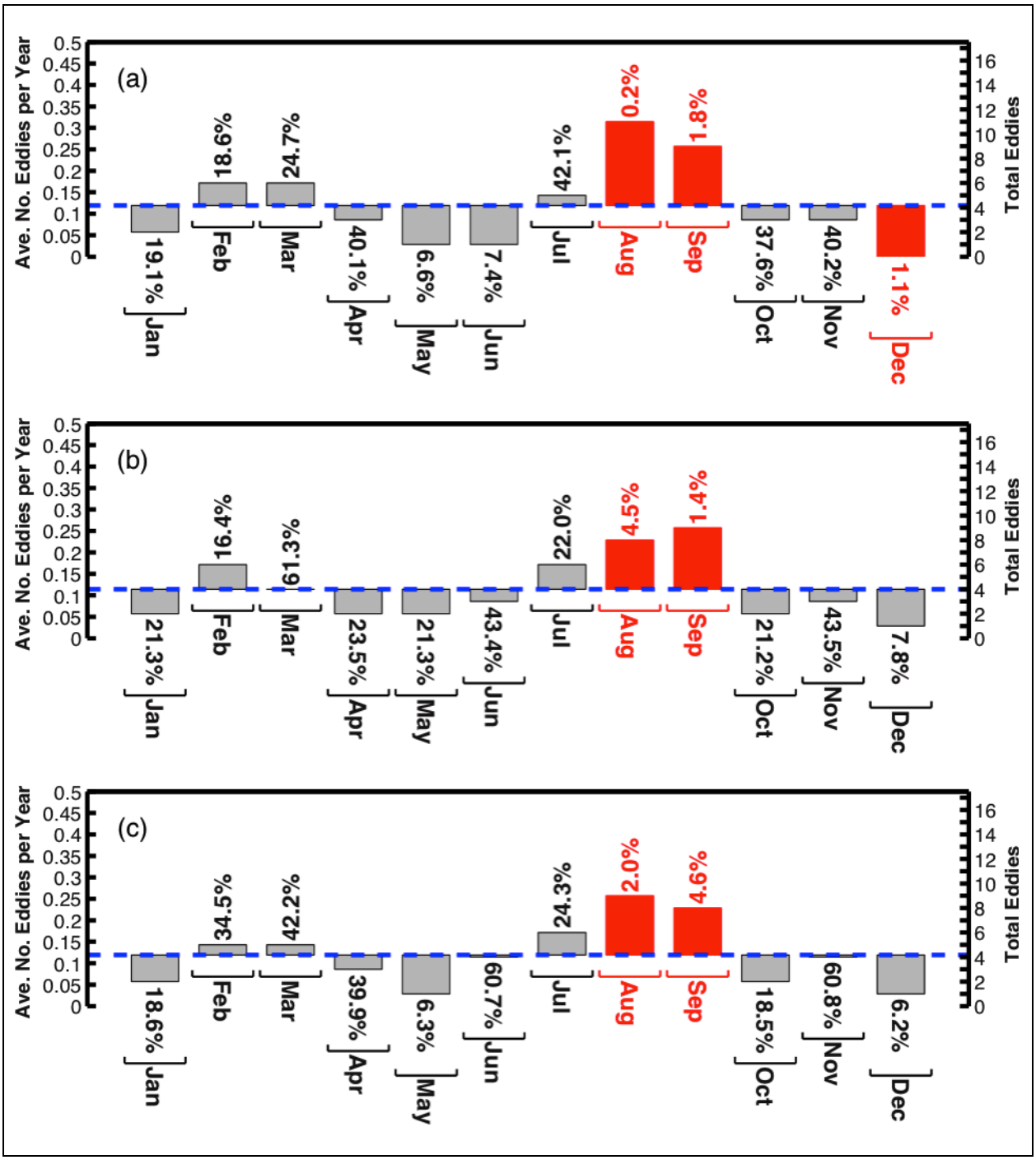

Fig. 19. Loop Current eddy separation dates binned monthly from combined pre-altimetry reanalysis (1978-1992) and (a) CCAR, (b) AVISO, and (c) AVISO-CUPOM altimetry (1993-2012). Blue dashed lines show the average number of Loop Current eddies to separate per month, per year. The percent likelihood of observing a Loop Current eddy count as extreme or more extreme by chance is displayed for each monthly bar. All bars at 5% or less are considered significant at the 95% confidence level and colored red.

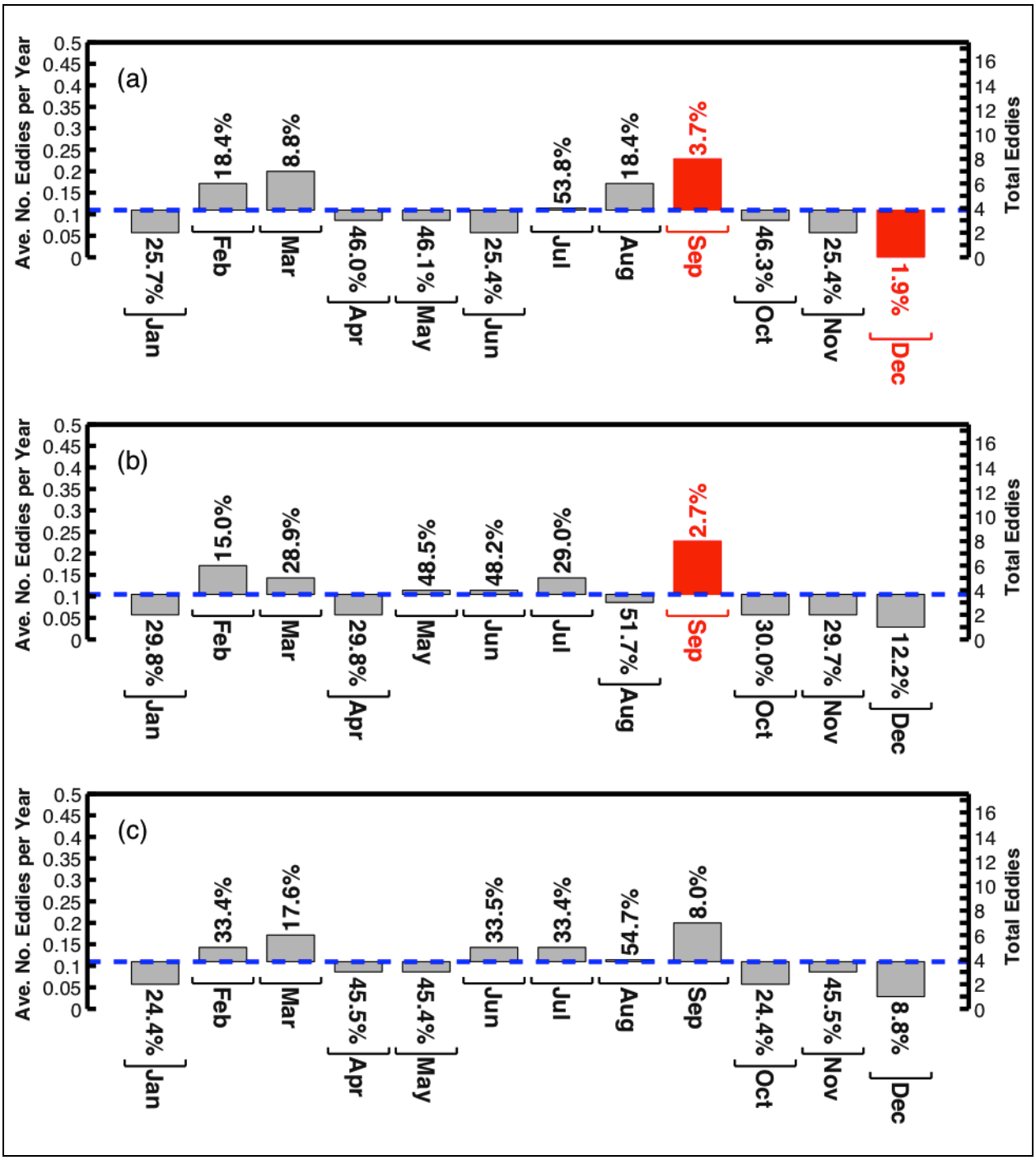

Fig. 20. Loop Current eddy separation dates binned monthly (1978-2012) from combined Vukovich (2012) pre-altimetry (1978-1992) and (a) CCAR, (b) AVISO, and (c) AVISO- CUPOM altimetry (1993-2012). Blue dashed lines show average number of Loop Current eddy separations per month, per year. The percent likelihood of observing a Loop Current eddy count as extreme or more extreme by chance is displayed for each monthly bar. All red bars at 5% or less are considered significant at the 95% confidence level and colored red.

Loop Current Eddy Separation Event Seasonal Centers and Boundaries

Significance testing indicates that the annual cycle of LCE separation has a strong significant peak in September, with a less distinct peak suggested in March. Therefore, it is natural to divide the cycle into the two seasons introduced before, the spring and the fall, respectively peaking near the spring (March) and fall (September) equinoxes. Though the peaks of the two seasons are evident, the centers and boundaries are not. The seasonal centers (means), which account for all events within the respective season, may not necessarily match the seasonal peaks determined by significance testing of the distribution. To precisely define the boundaries of the seasons, it is useful for separation events to be arranged in a "circular" sense. "Linear" annual histograms, such as in Figs. 16 through 20, show the existence of seasonality well, but poorly represent the cycle of the seasons from year to year. Some publications such as Chang and Oey (2012) concatenate two identical annual cycles to illustrate the flow of one year into the next. However, regardless of how the data are plotted, January and December observations are often kept separate for statistical analyses. Since it is possible that a separation season can begin at the end of one year and end at the beginning of the next, it is imperative that all events have connectivity with each other mathematically so that seasonal boundaries can be objectively defined.

As an alternative to traditional "number-line" representations, separation event dates can be represented in a circular manner around the unit circle on a complex plane. First, the corresponding day-of-year (DOY) for each separation event date is converted to an angle with units of radians using Eq. (1).

$$\alpha = \frac{2\pi(DOY)}{365} \tag{1}$$

Since DOY can be at most equal to 365 days and at least one day, α is always greater than zero and less than or equal to 2π. (Note that for a separation date falling in a leap year, the leap day is ignored, and the DOY is calculated as for a non-leap year. In the case that a separation occurs on

the leap day, Feb. 29, the DOY for Feb. 28 is used to keep the separation event in the correct month.) Then each angle α is transformed into a complex number:

$$z = \cos(\alpha) + i\sin(\alpha). \tag{2}$$

Separation dates in the form of complex numbers can then be plotted around the unit circle.

Figure 21 displays the pre-altimetry reanalysis date list from Table 3 plotted around the unit circle. Similar plots for the CCAR, AVISO, and AVISO-CUPOM altimetry date lists in Table 5 are shown in Fig. 22, and plots of the combined pre-altimetry and altimetry date lists are shown in Fig. 23. A k-means clustering algorithm was applied to each date list (seven altogether) to divide the events in each list into two distinct groups per plot, the spring (red dots) and fall (blue dots) seasons. (The results of a k-means scheme are dependent on the initialization of the algorithm; different initializations can result in different clusterings and, thus, different standard deviations of the two clusters in this situation. The k-means algorithm was semi-randomly initialized many times to identify the two event groups yielding the minimum rms of their standard deviations.) For each date list, the complex numbers corresponding to all dates in a season were averaged with Eq. (3) to find the geometric center or centroid of each season,

$$\bar{z} = \frac{1}{N}\sum_{j=1}^{N} z_j \,, \tag{3}$$

where the variable N represents the total number of events in the season. Then the mean angle was found as

$$\bar{\alpha} = \arg(\bar{z}), \tag{4}$$

where

$$0 < \bar{\alpha} \le 2\pi \,.$$

(Equation (1) can be used to calculate the DOY corresponding to the center of the season.) The colored triangles in each subplot of Figs. 21 through 23 represent the centers of the two seasons. The spring and fall equinoxes occur after the respective centers of the separation seasons are reached during the year (moving counterclockwise around the circle). The dashed lines plotted between the seasonal means each nearly pass through the origin of the corresponding unit circle, meaning that the centers of the two seasons are about six months apart in all seven date lists. (In fact, the dashed line in the pre-altimetry reanalysis figure, Fig. 21, crosses through the origin almost exactly.) Notice that the triangles do not lie on the unit circles as the dots do. The distance between each triangle and the unit circle is a measure of dispersion (standard deviation) in the dates in each season. The approximate circular analogue of the basic linear standard deviation is given by the following equation:

$$\alpha_{std} = \sqrt{2\left(1-\left|\bar{z}\right|\right)} \,. \tag{5}$$

The angle α_{std} in Eq. (5) can be substituted into Eq. (1) to yield standard deviation in units of days (Berens 2009; Jammalamadaka and SenGupta 2001).

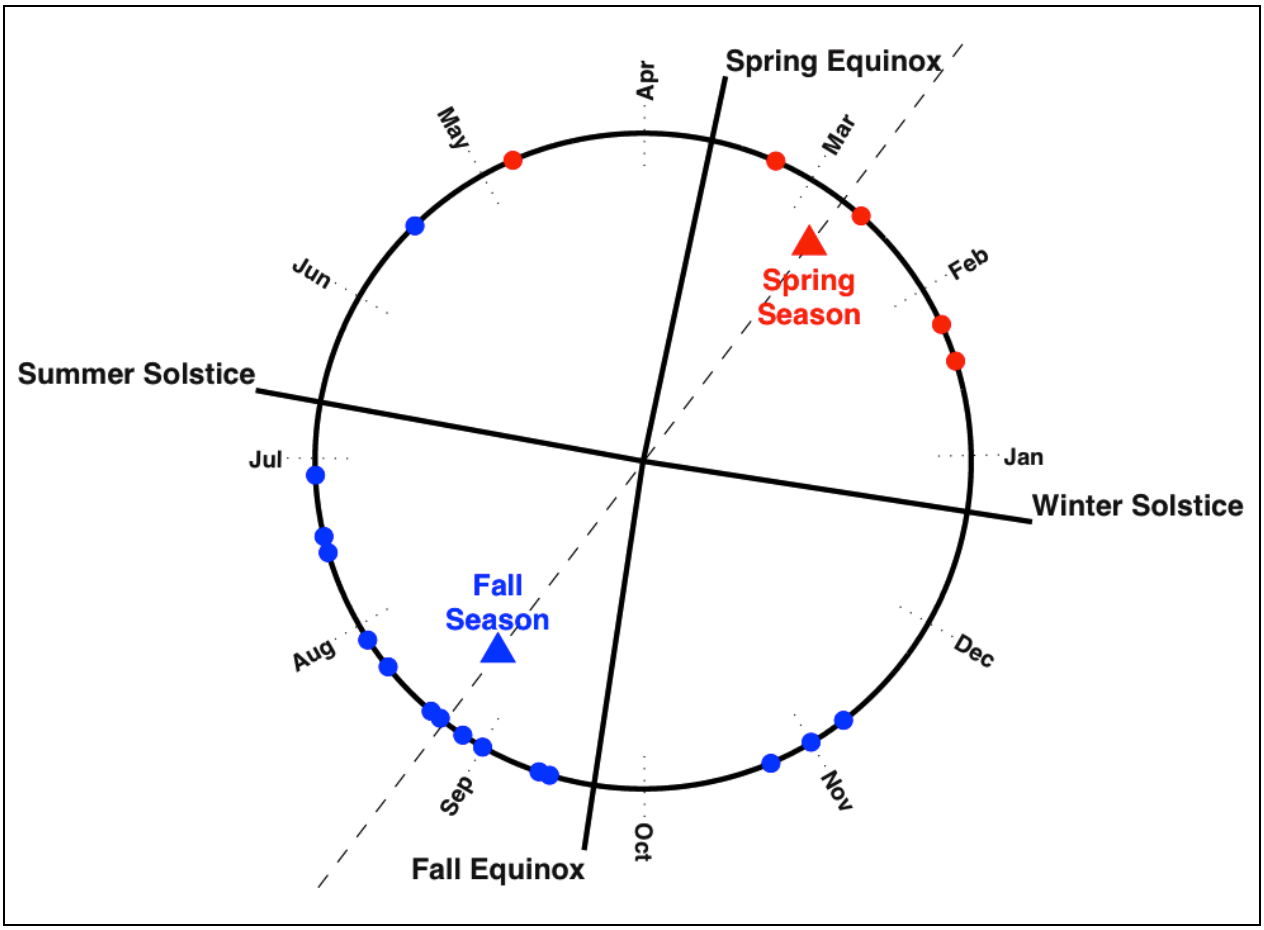

Fig. 21. Pre-altimetry reanalysis Loop Current eddy separation dates from 1978-1992 (Table 3) plotted as days-of-year on the unit circle in the complex plane, divided into spring (red) and fall (blue) seasons. Each dot represents a separation event. The triangles represent the means of the two seasons.

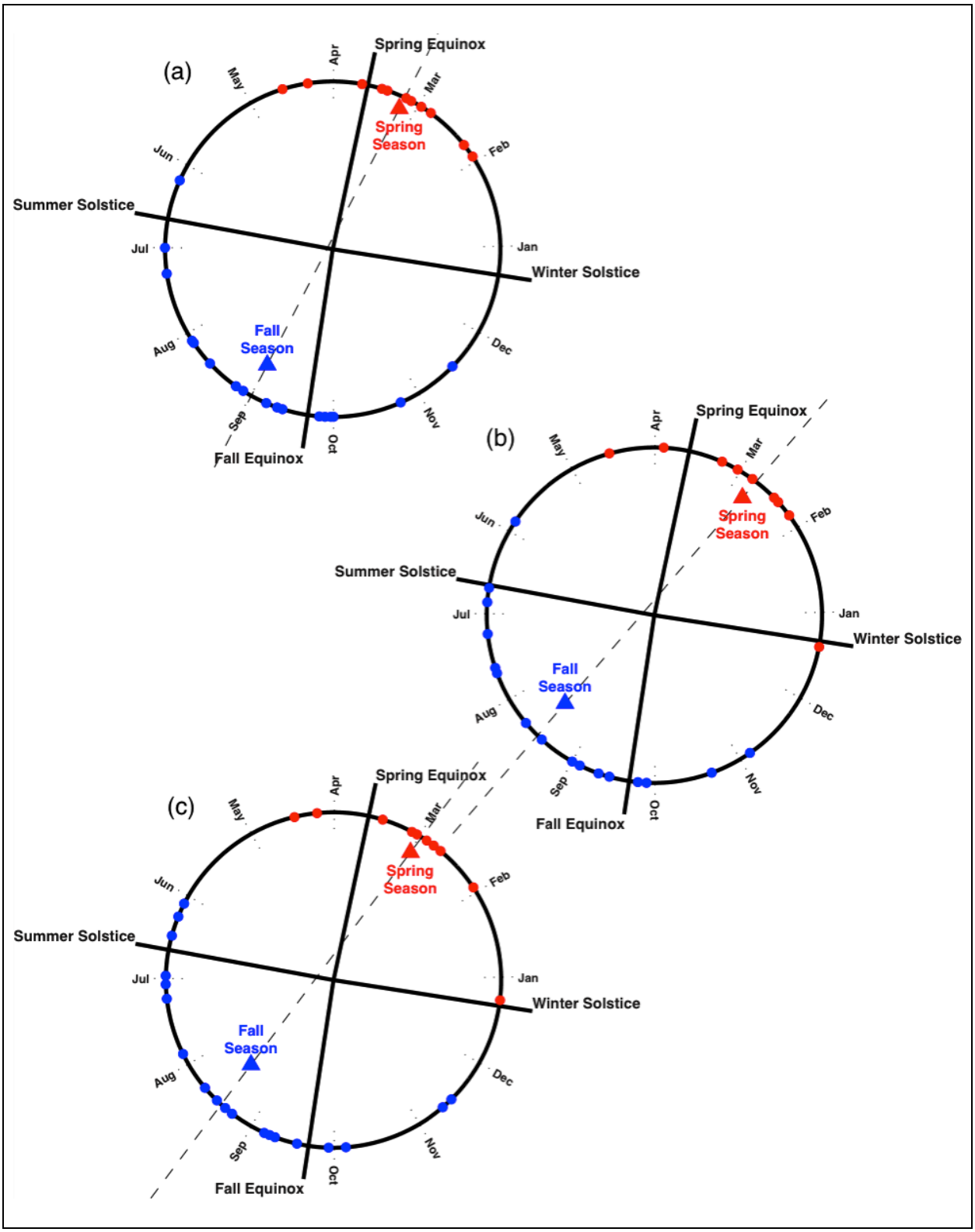

Fig. 22. Loop Current eddy separation dates (Table 5) from (a) CCAR, (b) AVISO, and (c) AVISO- CUPOM altimetry (1993-2012) plotted as days-of-year on the unit circle in the complex plane, and divided into spring (red) and fall (blue) seasons. Each dot represents a separation event. The triangles represent the means of the two seasons.

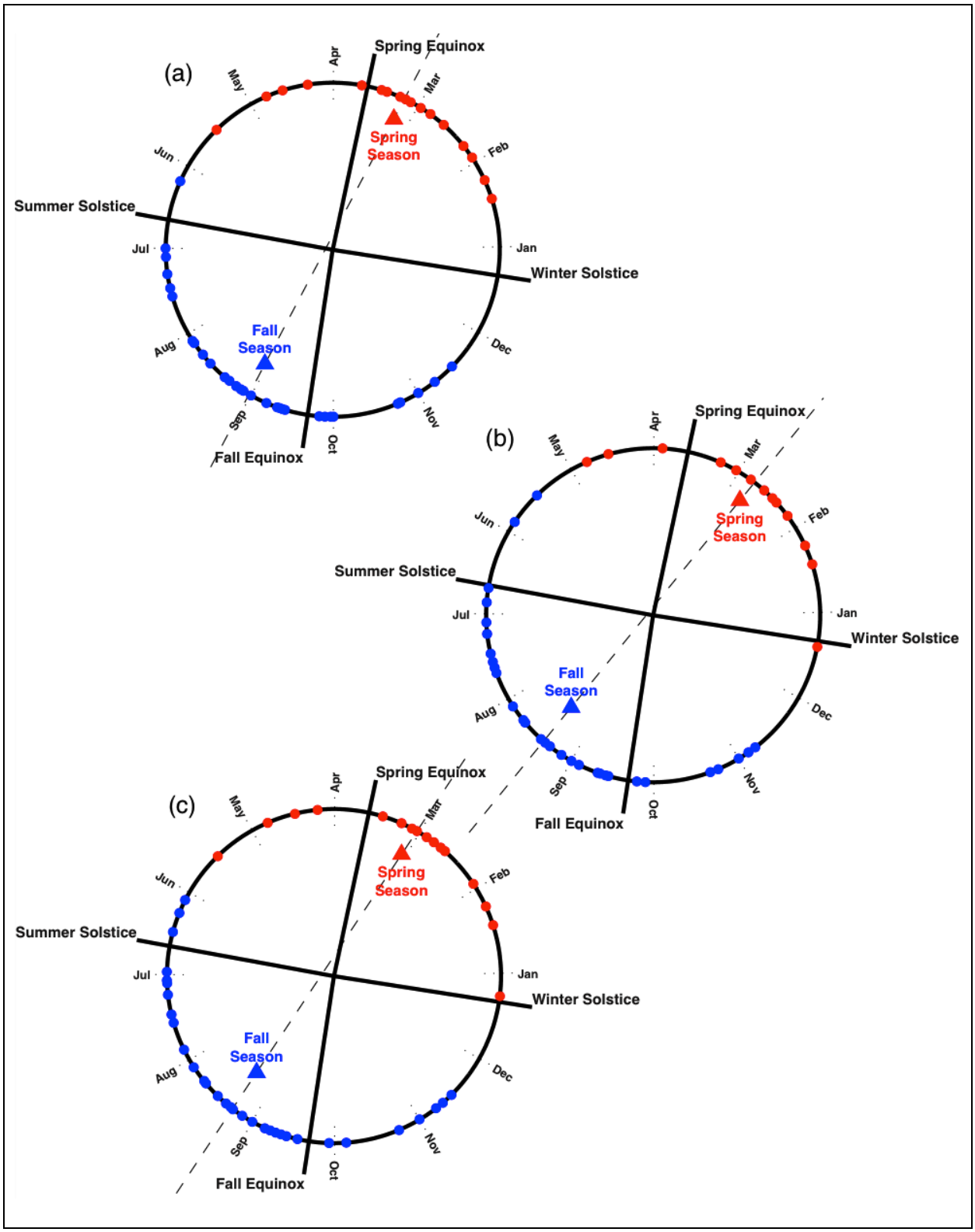

Fig. 23. Loop Current eddy separation dates (1978-2012) combining the reanalysis pre-altimetry with (a) CCAR, (b) AVISO, and (c) AVISO- CUPOM altimetry dates plotted as days-of-year on the unit circle in the complex plane, and divided into spring (red) and fall (blue) seasons. Each dot represents a separation event. The triangles represent the means of the two seasons.

The centers and standard deviations obtained from circular statistical methods are given in Table 11. Linear means and standard deviations calculated using DOYs instead of complex numbers are also presented in the table for comparison. Considering all seven date lists, circular results indicate that the spring mean lies within approximately a two-week period from Feb. 22 through Mar. 7 (~Mar. 1); standard deviations are between 22 and 34 days. Linear results are much less reliable. They indicate that the spring mean lies within a period larger than a month, from Feb. 24 through Apr. 2; standard deviations are between 23 and 96 days. The fall mean according to circular methods lies within approximately a two-week period from Aug. 16 through Sep. 01 (~Aug. 24); standard deviations are between 37 and 45 days. Linear methods also indicate the mean lies in a two-week window from Aug. 16 through Aug. 31; standard deviations are between 39 and 49 days. Mean circular and linear method results for the fall season are comparable. However, circular methods have a clear advantage for estimating the spring mean. The reason for this is because the AVISO and AVISO-CUPOM altimetry spring seasons start in December according to the clusterings in Figs. 22b and 22c. In Table 11, the CCAR spring circular mean is very similar to its corresponding linear mean, but the AVISO and AVISO-CUPOM spring linear means are significantly different than their respective circular means. Also, in comparison to the CCAR spring linear standard deviation, the standard deviations of the other two date lists are very large. This discrepancy is caused by the DOY bias of LCE Titanic, which separated in December in AVISO and AVISO-CUPOM but is part of the spring cluster. The Titanic DOY is high in the AVISO (354) and AVISO-CUPOM (358) date sets and low in the CCAR (39) dataset. LCE Titanic not only has a noticeable impact on spring linear AVISO and AVISO-CUPOM altimetry statistics, but also the linear combined AVISO and AVISO-CUPOM statistics in Table 11 and Figs. 23b and 23c.

Table 11. Centers (means) and standard deviations (std.) of Table 1 and Table 5 separation events analyzed separately and combined, separated into spring and fall seasons and presented circularly and linearly. Centers are given in day-of-year (DOY), and standard deviations in days.

	circular		**linear**	
	spring	*fall*	*spring*	*fall*
PRE-ALTIMETRY				
	Reanalysis, 1978-1992			
center (DOY)	53.2 (22 Feb)	236.0 (24 Aug)	54.8 (24 Feb)	235.5 (24 Aug)
std. (days)	33.6	42.5	38.9	47.3
ALTIMETRY				
	CCAR, 1993-2012			
center (DOY)	65.6 (07 Mar)	243.8 (01 Sep)	65.8 (07 Mar)	242.9 (31 Aug)
std. (days)	22.0	37.4	23.3	40.6
	AVISO, 1993-2012			
center (DOY)	53.9 (23 Feb)	227.7 (16 Aug)	90.0 (31 Mar)	227.8 (16 Aug)
std. (days)	28.9	41.3	95.4	44.7
	AVISO-CUPOM, 1993-2012			
center (DOY)	59.8 (01 Mar)	228.9 (17 Aug)	92.3 (02 Apr)	229.7 (18 Aug)
std. (days)	27.4	44.6	90.4	48.7
COMBINED				
	Reanalysis, 1978-1992+**CCAR**, 1993-2012			
center (DOY)	65.8 (07 Mar)	242.6 (31 Aug)	66.7 (08 Mar)	242.8 (31 Aug)
std. (days)	30.3	37.2	32.1	39.6
	Reanalysis, 1978-1992+**AVISO**, 1993-2012			
center (DOY)	53.7 (23 Feb)	231.5 (20 Aug)	78.3 (19 Mar)	231.3 (19 Aug)
std. (days)	30.6	42.0	81.1	45.3
	Reanalysis, 1978-1992+**AVISO-CUPOM**, 1993-2012			
center (DOY)	61.8 (03 Mar)	234.5 (23 Aug)	83.8 (25 Mar)	235.2 (23 Aug)
std. (days)	33.5	41.9	77.3	45.0
	Reanalysis, 1978-1992+**CCAR**+**AVISO**+**AVISO-CUPOM**, 1993-2012			
center (DOY)	61.0 (02 Mar)	235.3 (23 Aug)	79.9 (21 Mar)	235.2 (23 Aug)
std. (days)	29.5	40.9	70.2	43.5

Circular statistics account for relative positioning of the events better than standard linear (number-line) statistics, resulting in superior mean estimates. Note that each circular standard deviation in Table 11 is lower than the corresponding linear standard deviation, indicating that circular statistics have higher reliability. Linear statistics in Vukovich (2012) should be interpreted in light of the statistical discussion above. Instead of grouping separation events into two seasons, Table 2 of Vukovich (2012) reports that the average separation month of all events

for three different year ranges is June, with a standard deviation of three months. The standard deviation was likely calculated assuming a normal distribution. However, none of the histograms in Fig. 17 appear normally distributed. The mean of a normal distribution is equal to the most likely value, which Vukovich (2012) indicates is June, but most of the histograms in Fig. 17 show that LCEs are unlikely to separate in that month. Table 4 of Vukovich (2012) lists 48 LCE separation events from 1972 through 2010, only three (6%) of which were June events. Because the series of 12 calendar months repeats in a perpetual cycle, giving an "average" separation month on a number line, such as June, is meaningless and misleading since one might be led to believe that June events happen frequently. To the author's credit, Vukovich (2012) also provides separation month mode, March, which has more statistical significance.

Seasonal clusterings of the pre-altimetry reanalysis and CCAR, AVISO, and AVISO-CUPOM altimetry LCE separation date sets separately are somewhat sensitive to changes in event dates. The addition of a single new event to a list can cause events to be reclustered into opposite seasons, shifting seasonal means by weeks. A larger number of events in each season must be observed before the seasons will "stabilize" and seasonal boundaries can be estimated. However, this number is not known a priori and depends on the stationarity of the process being observed. Even with the combined date sets, which include more separation events than do the pre-altimetry or altimetry date sets separately, the seasonal boundaries are not well isolated. In Fig. 23a, one boundary is between mid-May and early June, and the other between mid-November and mid-January. In Fig. 23b, the boundaries are sometime in early May and between mid-November and mid-December. In Fig. 23c, the boundaries are sometime in late May, and between mid-November and mid-December. For the best possible estimate of seasonal boundaries, the pre-altimetry reanalysis dates and the CCAR, AVISO, and AVISO-CUPOM dates were all combined together into one date list and clustered as before (not shown). The results indicate that the boundary between spring and fall is between May 16 and May 28 (~May 22), and the boundary between fall and spring is between Nov. 16 and Dec. 20 (~Dec. 3). Center and standard deviation statistics for this combined date list are included in Table 11. The spring center is Mar. 2, and the fall center is Aug. 23.

CHAPTER VI

INVESTIGATION OF DYNAMICS CONTRIBUTING TO LOOP CURRENT SEASONALITY

In the present study, statistically significant seasonality has been identified not only in the annual cycle of LC metrics (Chapter IV), but also in the bimodal distribution of LCE separation events (Chapter V). Somewhat differently, recent publications Chang and Oey (2012; 2013a) discussed *biannual* variations. Chang and Oey (2012) conjectured that the biannually varying combination of GOM and Caribbean winds affect GOM and Caribbean transports, which cause more LCEs to shed in summer and winter and less LCEs to shed in spring and fall based on a series of process oriented modeling experiments. Chang and Oey (2013a) further stated that the LC shows biannual, asymmetric intrusion/retreat captured by the first two empirical orthogonal function (EOF) modes of SSH in the eastern GOM/northern Caribbean Sea, with the more dominant intrusion/retreat from summer to fall and the less dominant from winter to spring. In this chapter, EOF analyses will be used to explore the primary cause of the seasonal characteristics described earlier in this dissertation and to revisit the findings determined from the process modeling studies and preliminary altimetric data analysis performed by Chang and Oey.

Deepwater EOF Analysis

EOFs are a powerful tool for identifying the dominant variability in a dataset and are useful for exploring seasonal variations in the LC as well. The following analysis 1) uses EOFs to capture the dominant LC variability in the 20-year altimeter time series, 2) shows that the dominant LC variability also contains seasonal variability, 3) extracts the seasonal EOF modes containing the annual variability, and 4) evaluates proposed physical mechanisms causing the seasonal modes and the annual LC variability.

Monthly SSH fields from 1993 through 2012 were generated from delayed-time weekly ¼° AVISO mapped SSH fields. A small amount of daily near real-time data was included to complete the dataset through the end of the year 2012. The monthly data were demeaned in the deepwater by subtracting the averaged values of SSH from the monthly maps in GOM waters deeper than 200 m to remove the steric signal associated with seasonal heating of the mixed layer. The steric signal is removed since it is an annual signal in the GOM that would otherwise dominate the first mode of an EOF decomposition of SSH, but does not contribute to the dynamical variability of the LC. All data over the shelf were masked so that the EOF decomposition would reflect LC variability, which is predominately confined to the deep waters of the GOM. This also prevents mode mixing (Kim and Wu, 1999) of the deepwater and shelf variability in the EOF analyses. An EOF decomposition was calculated over the domain 98°W-80°W, 18°N-31°N. This is different than the EOF domain used by Chang and Oey (2013a) for analysis of the AVISO data, which covered 92°W-80°W, 15°N-31°N and included the continental shelf. In all deepwater EOF analyses shown in this dissertation the spatial signal over the shelf was reconstructed for each spatial EOF loading vector by regressing the corresponding principal component time series (PCTS) onto the original SSH time series over the shelf to map shelf signal correlated with the deepwater SSH variability.

The first two EOF loading vectors are shown in Fig. 24 and account for 24.6% and 16.6% of the deepwater SSH variance. Gray dashed lines plotted on the loading vectors define the data masking boundaries of the EOF decomposition. With the exception of the lines that transect the

Yucatan Channel and Florida Straits, the lines follow the 200 m isobath. In comparison to the first two loading vectors, corresponding EOF modes shown in Fig. 10 of Chang and Oey (2013a) accounted for 29.5% and 17.2% of the variance, higher in both cases. This is due to differences in steric signal removal procedures, to differences in EOF decomposition domains, and likely to other differences not described in their methods (see below). The third and forth EOF loading vectors are shown in Fig. 25 and account for 11.1% and 6.6% of the deepwater variance. All together, the first four modes account for 58.9% of the variance in the monthly averaged data. EOF mode 1 leads EOF mode 2 by 55 days (EOFs derived from daily data were used to improve lag estimation only) based on a cross-correlation between PCTS 1 and 2. Further cross-correlation testing shows that mode 3 leads mode 4 by 65 days (see Fig. 26).

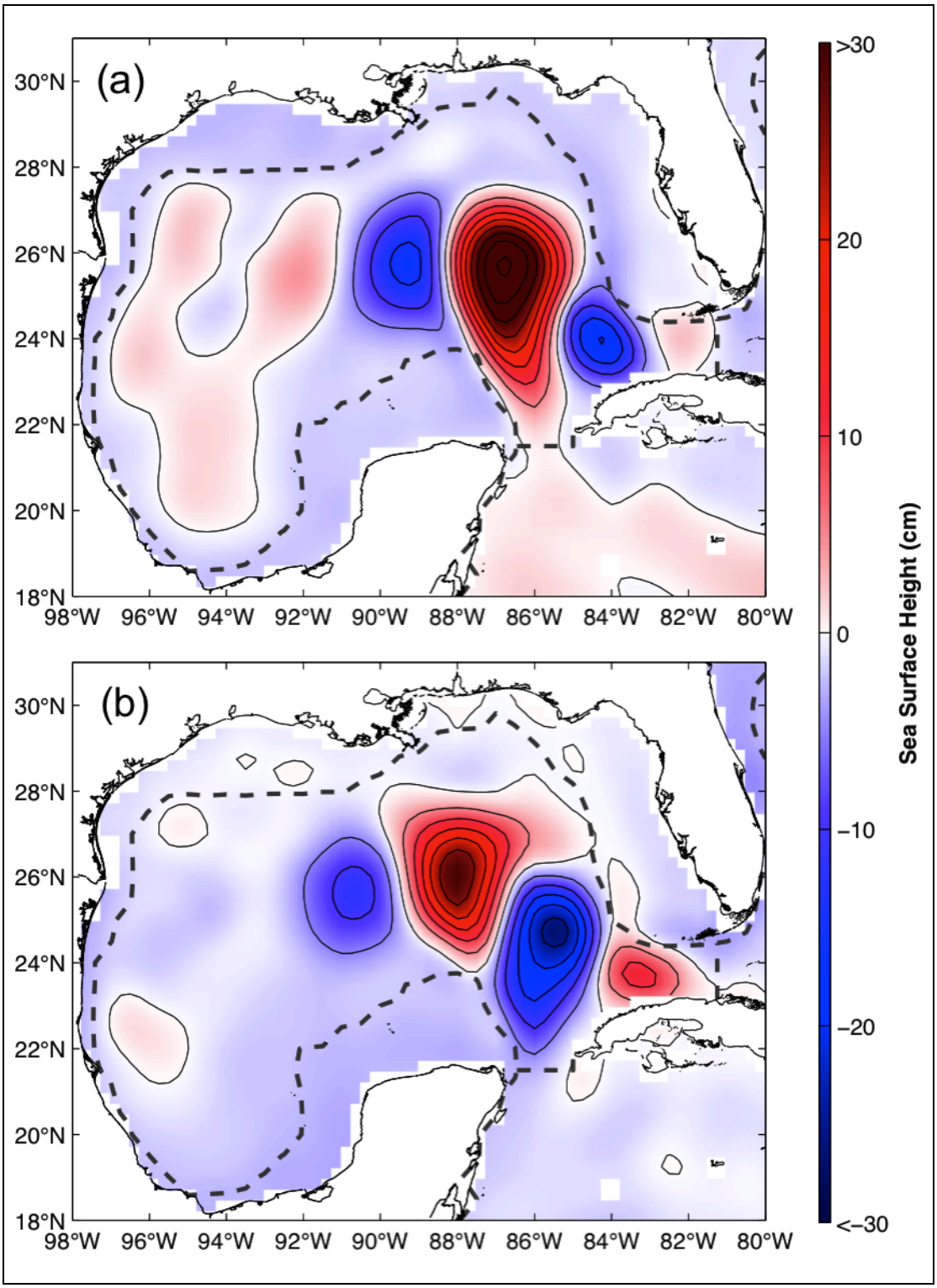

Fig. 24. Deepwater (a) EOF mode 1 and (b) EOF mode 2 loading vectors, derived from monthly AVISO sea surface height with the steric signal removed. Mode 1 explains 24.6% of the variance, and mode 2 explains 16.6%. Black contours are at 5 cm intervals. Gray dashed lines signify the boundaries of the EOF decomposition. The lines follow the 200 m isobath everywhere except across the Yucatan Channel and Florida Straits.

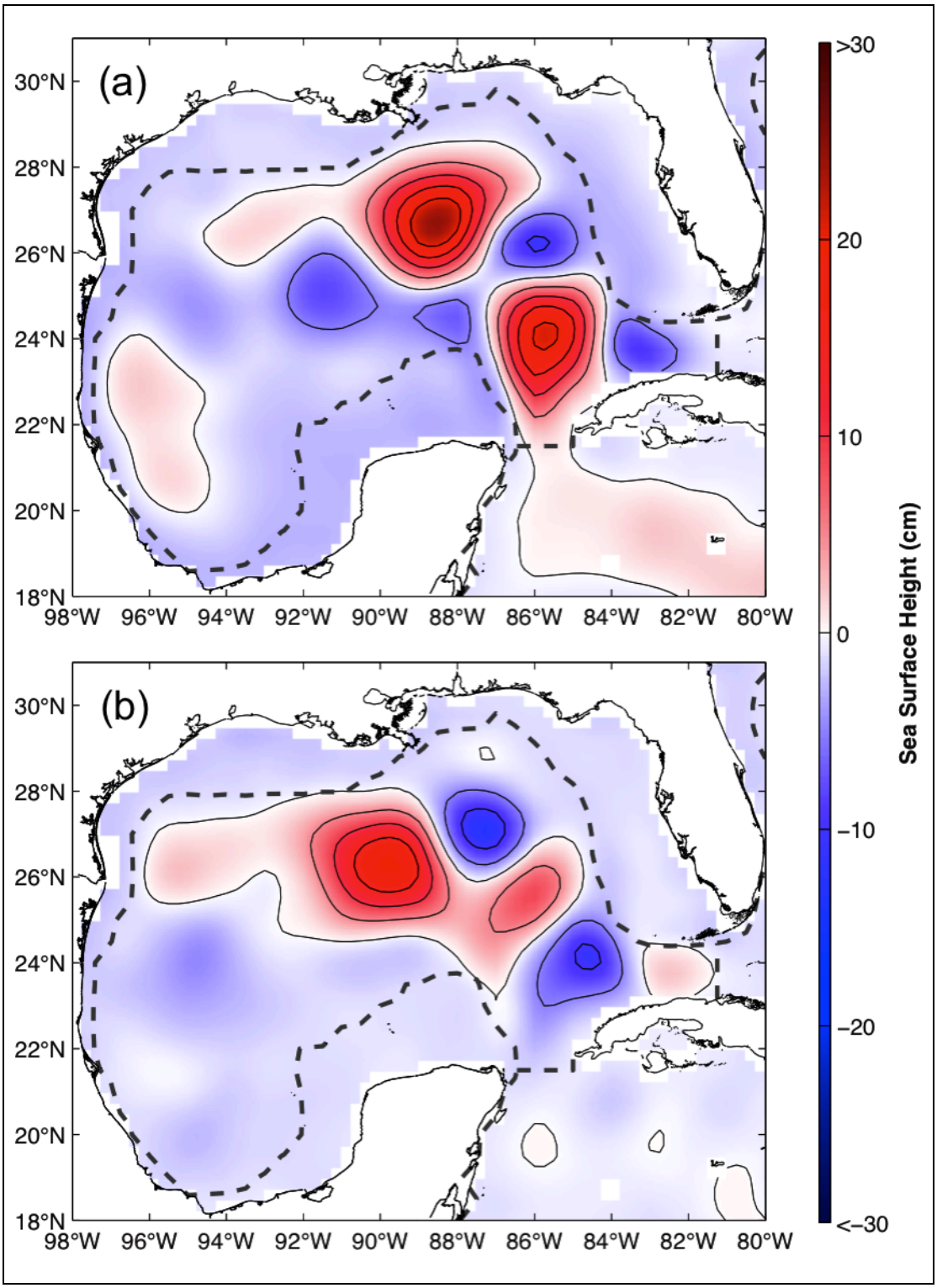

Fig. 25. Deepwater (a) EOF mode 3 and (b) EOF mode 4 loading vectors, derived from monthly AVISO sea surface height with the steric signal removed. Mode 3 explains 11.1% of the variance, and mode 4 explains 6.6%. Black contours are at 5 cm intervals. Gray dashed lines signify the boundaries of the EOF decomposition. The lines follow the 200 m isobath everywhere except across the Yucatan Channel and Florida Straits.

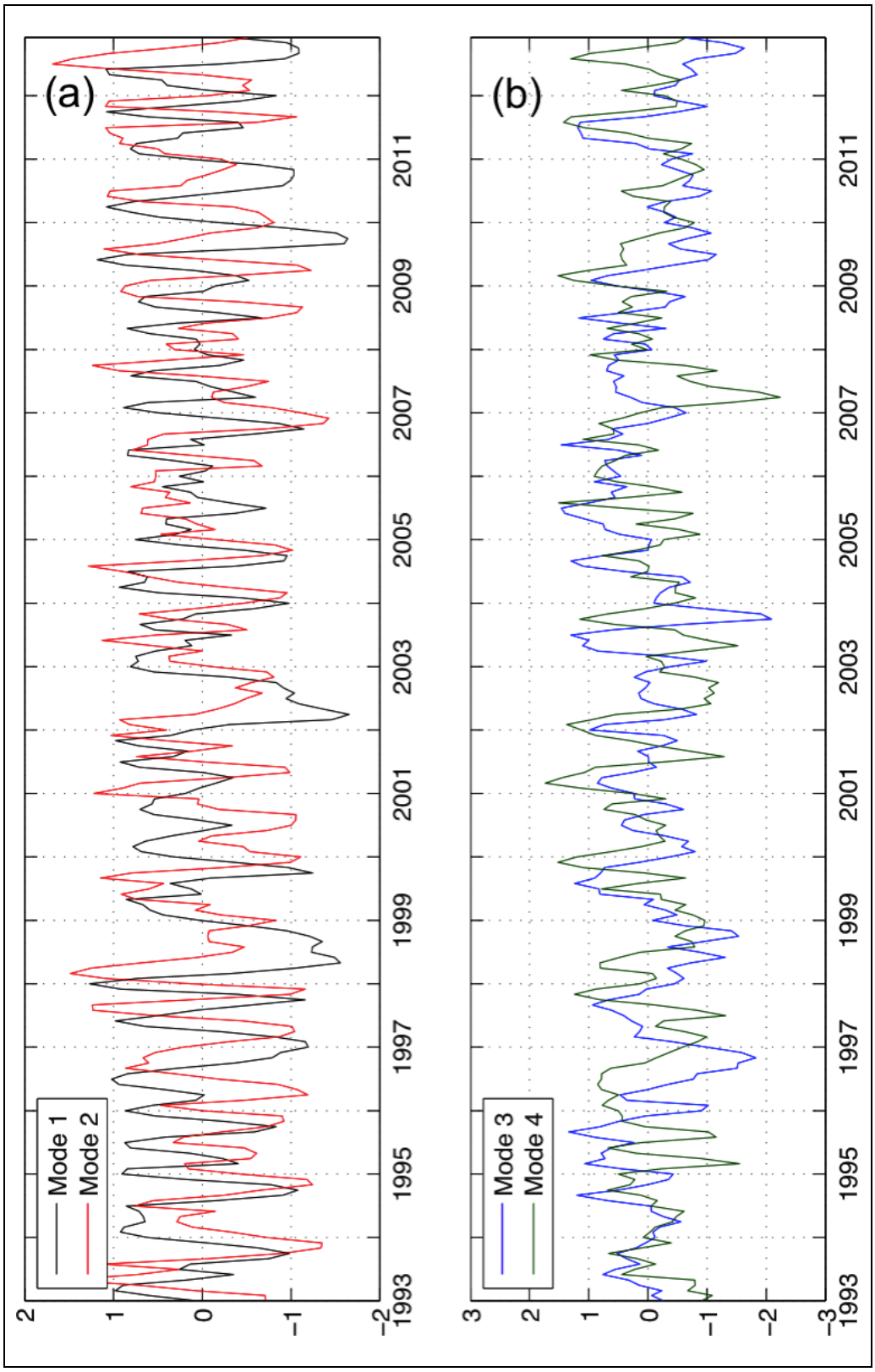

Fig. 26. Deepwater EOF principal component time series for (a) Mode 1 and Mode 2 and (b) Mode 3 and Mode 4, derived from monthly AVISO sea surface height with the steric signal removed.

When combined with the PCTS modes shown in Fig. 26, the spatial patterns in Fig. 24 and Fig. 25 blend into a continuous three-event sequence: LC penetration, LCE separation, and westward LCE propagation. Table 5 shows that there were 28 LCEs detected in the 20-year AVISO altimetry record. This averages out to about one LCE separation every 8.6 months. An approximate count of local peaks is 27 in PCTS 1 (using monthly EOFs); 26 in PCTS 2; 25 in PCTS 3; 29 in PCTS 4. There are about as many peaks in the PCTS as there are separation events, meaning that on average the propagating LCE pattern in the first four EOF modes repeats about as frequently as LCEs separate in the AVISO data, between eight and nine months. This is approximately commensurate with the periods associated with the two quadrature pairs formed by the first four EOF modes, which are 7 1/3 months (4*55 days) for modes 1 and 2 and 8 2/3 months (4*65 days) for modes 3 and 4. The four deepwater EOFs in Figs. 24 and 25 represent most of the LC and LCE SSH variability in the eastern GOM.

These results are in contrast to the 3-month lagged correlation found between the first two EOF PCTS by Chang and Oey (2013a) in their EOF analysis of the monthly AVISO data. A 3-month lagged correlation corresponds to an annual period for the dominant quadrature pair. Why is there such a discrepancy, 7 1/3 months versus 12 months, between the periods of the dominant quadrature pairs from these two EOF analyses of AVISO monthly data? An attempt was made to duplicate the EOF decomposition performed by Chang and Oey to confirm the 3-month lag. Chang and Oey used monthly 1/3° AVISO mapped SSH fields from January 1993 through December 2010. Yu-Lin Chang (personal communication) indicated that the steric signal was removed by averaging over the GOM and northwestern Caribbean Sea (98°W-80°W, 15°N-31°N). Then EOFs were computed over the domain 92°W-80°W, 15°N-31°N. Using these details, the resulting "duplicate" EOF decomposition I performed showed that the variance explained by the first EOF mode was 25.4%, and by the second EOF 15.9%, both still lower than the values quoted by Chang and Oey (2013a). Also curiously, the lag computed between the first and second "duplicate" mode PCTS was two months, not three. Yet another EOF decomposition on the monthly AVISO dataset prepared for this dissertation (not shown) was performed over the

domain 92°W-80°W, 18°N-31°N, ignoring the western GOM. Mode 1 led mode 2 by 54 days, and mode 3 led mode 4 by 65 days, comparable in both instances to the original lagged analysis results of 55 and 65 days, respectively. Including the western GOM or northwestern Caribbean Sea variability does not significantly affect the decomposition of the dominant LC variability modes.

Returning again to the original EOF decomposition, Fig. 27 shows the composite annual cycle (CAC) of the PCTS computed by averaging all PCTS values shown in Fig. 26 for each month, with 95% confidence intervals (N = 20, t-score = 2.093) included. The CAC of PCTS 1 is dominantly annual, with the trough in October being statistically different than the months January, February, March, May, and June. The CAC is weakly biannual with two small peaks in February and May, though this biannual signal is not significant. The CAC of PCTS 2 has no statistically significant monthly variance, but does exhibit some biannual variation with one peak in February and the other in July. February peaks in the CACs of both PCTS 1 and PCTS 2 are indicative of LC northward penetration and westward spreading. In contrast, the two-month delay between the May and July peaks of the first and second CACs, respectively, indicates LC northward penetration and LCE detachment or separation. The CAC of PCTS 3 is mainly annual with a significant trough in November, while the CAC of PCTS 4 is nondescript.

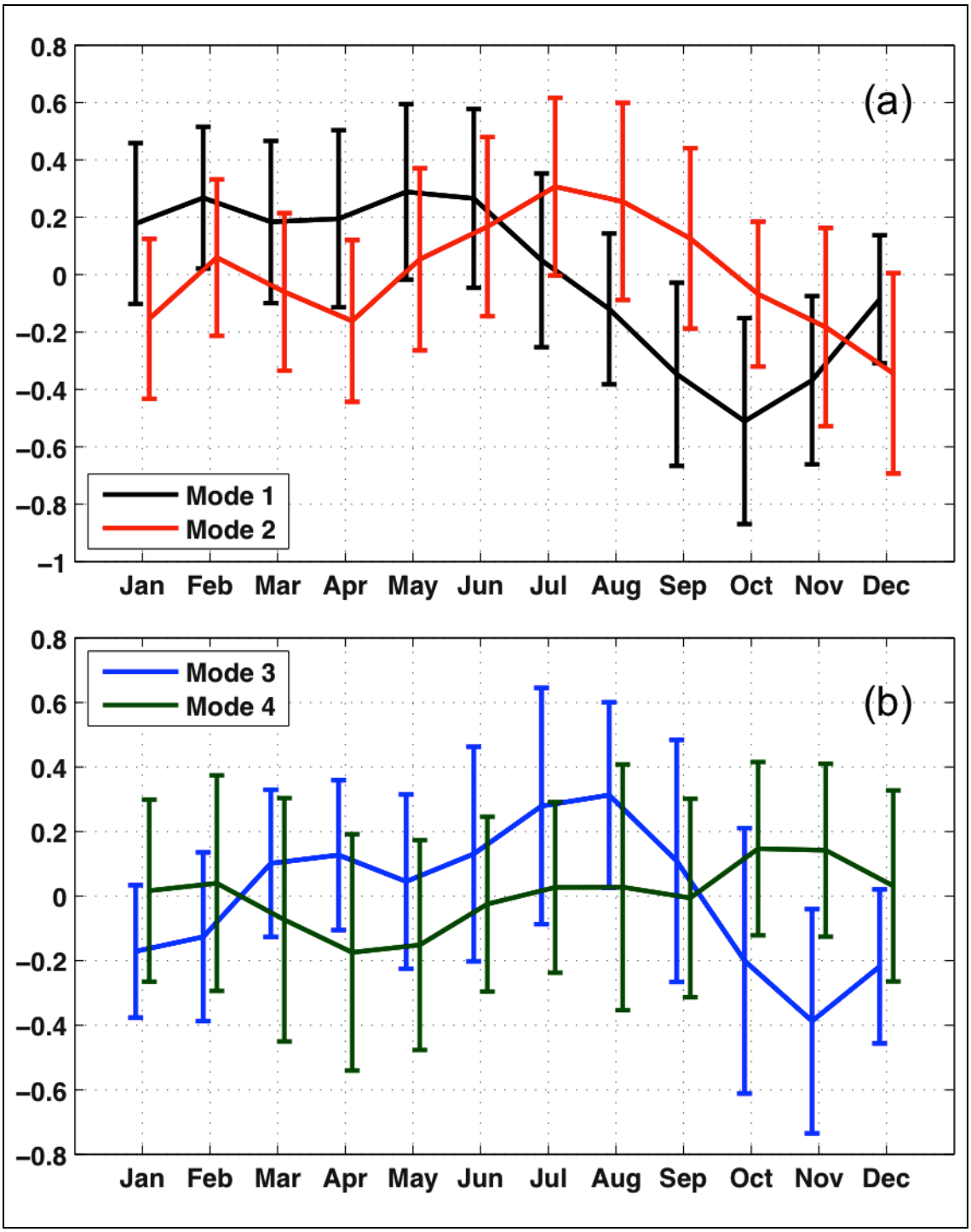

Fig. 27. Composite annual cycles generated from deepwater EOF principal component time series (a) Mode 1 and Mode 2 and (b) Mode 3 and Mode 4. Error bars are 95% confidence intervals (N = 20, t-score = 2.093).

Figure 28a shows the sum of monthly variance of the AVISO data in the GOM and northwestern Caribbean Sea, and Fig. 28b provides the fraction of that variance contained within a monthly reconstruction of the first four deepwater EOF modes. The map shows that LC variance has been largely isolated and is upwards of 80% represented by the four modes. Notably, SSH variations along parts of the shelf are correlated with LC variations since the four EOF modes account for more than 30% of the variance in some areas of the Texas-Louisiana Shelf and more than 40% over some areas of the Campeche Bank. The map also shows that the variations in the western GOM and northwestern Caribbean deepwater are uncorrelated with the dominant LC variability. The deepwater EOF modes beyond the first four describe western GOM variations more than LC variations. Since a primary objective of the deepwater EOF analysis was to isolate LC variability, the remaining EOF modes were excluded from further analysis.

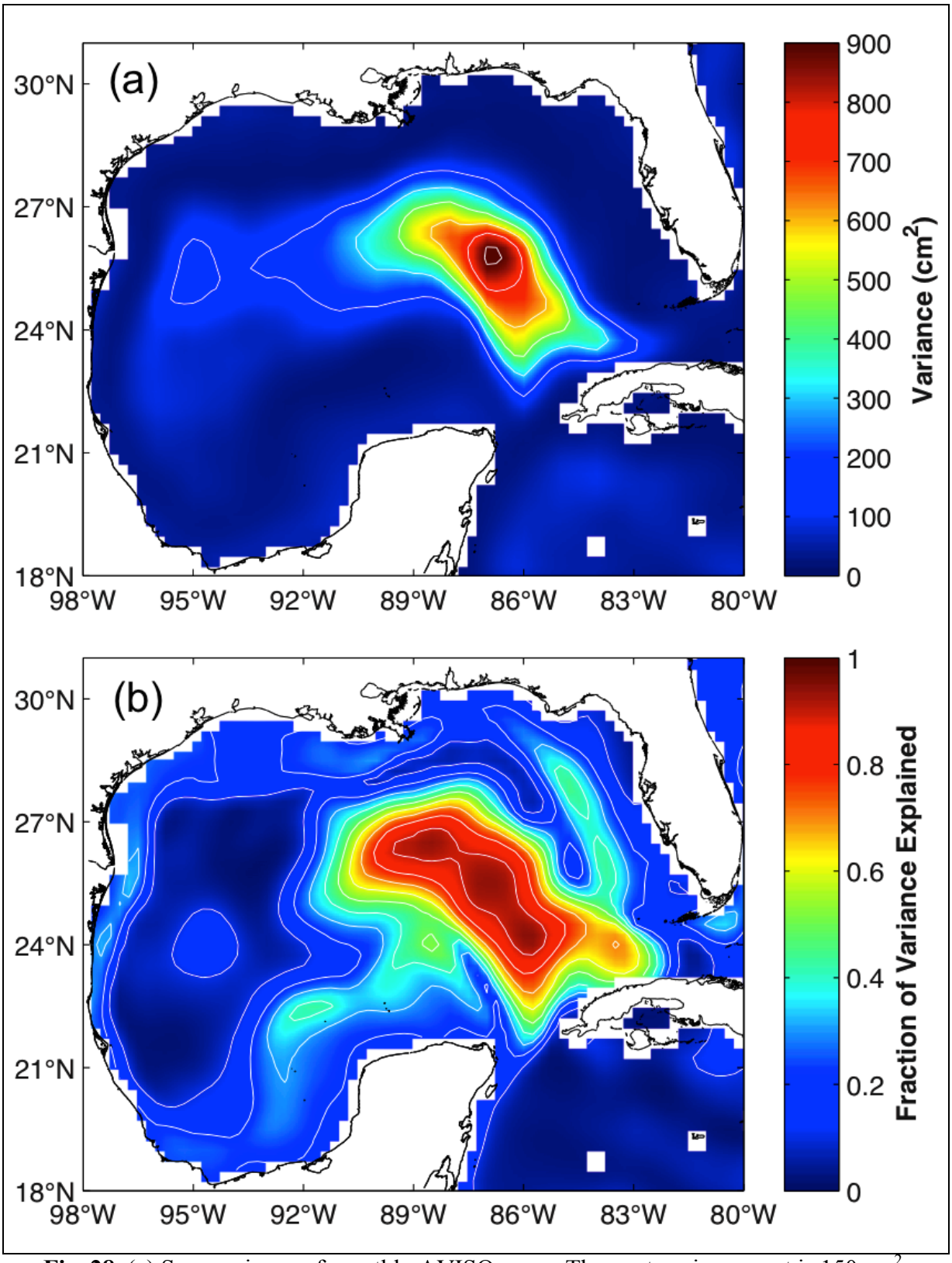

Fig. 28. (a) Sum variance of monthly AVISO maps. The contour increment is 150 cm^2. (b) Fraction of total variance captured by first four deepwater EOF modes including correlated signals at depths less than 200m. The contour increment is 0.1.

The CACs of the LC metrics shown in Fig. 14, derived from the complete 20-year AVISO monthly SSH dataset, capture the annual variability of the LC in the AVISO dataset very well. The CACs were computed by averaging all LC metric values for each month and each LC metric (area, area including detachments, volume, anticyclonic circulation, northernmost latitude, and westernmost longitude) to create a monthly mean time series for each metric. Using a different technique, CACs of the same LC metrics mentioned were computed from CAC SSH map sets derived from various monthly reconstructions using the first four deepwater EOF loading vectors shown in Figs. 24 and 25 to verify that the EOF modes contribute the majority of LC seasonal variability. Note that the LC metric CACs shown in Fig. 14 were generated by averaging monthly LC metric values. The LC metric CACs discussed here (Figs. 29 and 30) were created by generating an "average year" map set and then computing the corresponding LC metrics from that set. The first CAC SSH map set was calculated from the monthly-reconstructed deepwater EOF mode 1. SSH maps from each specific month were averaged to create a composite sequence of twelve maps, January through December, corresponding to the annual cycle, called CAC1. The second CAC SSH map set was calculated from the monthly reconstruction of modes 1 and 2 together and is CAC12. Similarly, two more EOF CAC map sets were calculated called CAC123 and CAC1234, and a final reference CAC map set was calculated from the original monthly AVISO SSH data called CAC_raw. The six listed LC metrics were calculated from each of the five CAC map sets. The names CAC_raw, CAC1, CAC12, CAC123, and CAC1234 will be used to refer to each respective twelve-month map sequence as well as individual LC metric CACs depending on the context. Since the LC metrics exhibit similar trends, only the maximum northern latitude and area are shown in Fig. 29 and Fig. 30, respectively. Figure 29a and Fig. 30a show CAC_raw (metrics) compared to CAC1 and CAC12. Figure 29b and Fig. 30b show CAC_raw compared to CAC123 and CAC1234.

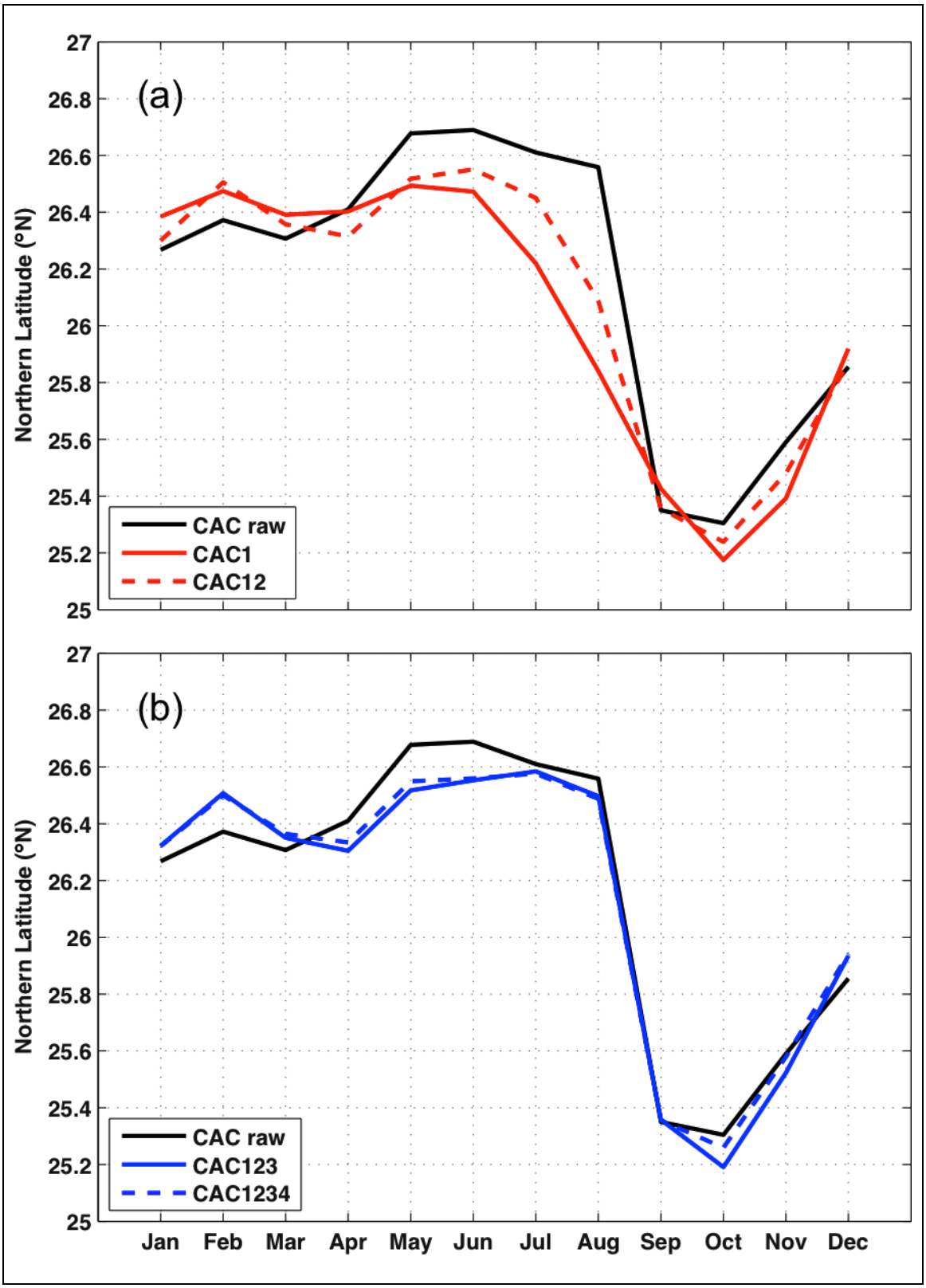

Fig. 29. Composite annual cycle of Loop Current northern boundary latitude. CAC_raw is plotted with (a) CAC1 and CAC12; (b) CAC123 and CAC1234.

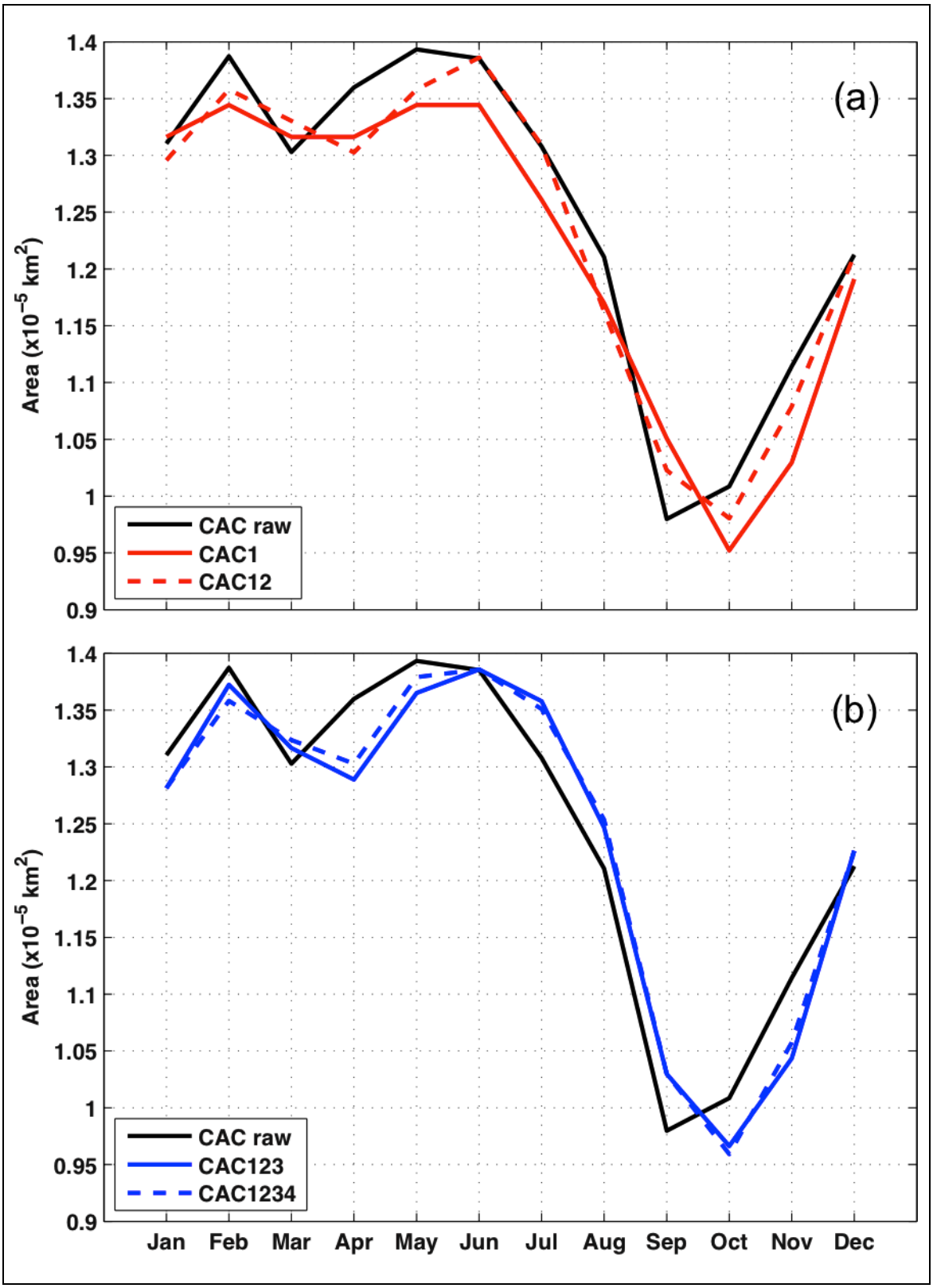

Fig. 30. Composite annual cycle of Loop Current area. CAC_raw is plotted with (a) CAC1 and CAC12; (b) CAC123 and CAC1234.

Figures 29 and 30 both show that CAC1 reproduces the dominant LC metric variability: relatively high values from January through June, low values during September and October, and then a rise to the end of the year. The next two EOF modes added in the CAC12 and in the CAC123 reconstructions additionally improve the metric approximation. Variance values are given in Table 12 for CACs and for the corresponding monthly-reconstructed time series for comparison. Area CAC variance explained reaches a maximum with only the first two modes. In contrast, monthly variance explained by the first two modes computed from the entire monthly time series is at a minimum for both northern latitude and area. The impact of the fourth EOF mode in CAC1234 is minimal. Minor improvements to the northern latitude approximation are found in April, May, and October of Fig. 29b, and minor improvements to the area approximation are found in April and May of Fig. 30b. The metric approximation will converge to the actual metric time series, CAC_raw, slowly as more EOF modes are added, though some EOF modes will "locally" make the approximation worse. Since approximation adjustments caused by the fourth EOF mode were so slight and since the fifth EOF mode (not shown) appeared to be more of a central/western GOM mode than an eastern GOM mode, it is likely that the dominant LC variability was captured by the first four EOF modes, so no further modes were added. In terms of fit, the LC northern latitude correlation between CAC_raw and CAC1234 is 0.9871 (variance 0.9744). The LC area correlation is 0.9632 (variance 0.9277). Between the 20-year complete AVISO dataset and the 20-year reconstruction of the first four EOF modes, the LC northern latitude correlation is 0.7842 (variance 0.6149), and the LC area correlation is 0.7980 (0.6367).

Table 12. Proportion of Loop Current northern latitude and area variance explained by first four deepwater EOF modes reconstructed as monthly time series and as composite annual cycles (CAC1, CAC12, CAC123, and CAC1234) with reference to complete monthly time series and composite annual cycle of original AVISO data (CAC_raw).

	LC Northern Latitude Variance		LC Area Variance	
	Monthly	CAC	Monthly	CAC
EOF 1	0.2643	0.7668	0.2263	0.9212
EOF 1,2	0.1374	0.9084	0.1457	0.9574
EOF 1,2,3	0.5921	0.9662	0.6099	0.9179
EOF 1,2,3,4	0.6149	0.9744	0.6367	0.9277

EOF modes of monthly data, as in Figs. 24 and 25, capture LC variability very well, but are not optimal for describing seasonal signals. For instance the CAC of PCTS 2 in Fig. 27 indicates that the corresponding loading vector in Fig. 24 has biannual power within a monthly context. However, the same biannual signal may not appear in an average year since the signal averages out. Additional EOF decompositions were performed on CAC_raw and CAC1234 for further insight into the LC variability. Figure 31 shows the deepwater mode 1 and mode 2 loading vectors of the CAC_raw EOF decomposition. Mode 1 in Fig. 31a accounts for 43.0% of the SSH variance within CAC_raw, and mode 2 in Fig. 31b accounts for 30.2%. Most of this variance is in the eastern GOM. CAC_raw mode 3 and mode 4 loading vectors in Fig. 32 account for 10.7% (Fig. 32a) and 8.6% (Fig. 32b) of the variance, respectively. The eight remaining EOF modes account for 7.5% total. PCTS corresponding to the first four EOF modes are shown in Fig. 33. The PCTS of mode 1 and mode 2 are both mainly annual signals. Mode 1 has one main trough in October, which is associated with the fundamental variation of the LC metric CACs shown in Fig. 14. The dominant peak in mode 2 is in August. Mode 2 also exhibits some weakly biannual signal associated with a small peak in March. In comparison, the monthly deepwater EOF mode 2 PCTS CAC in Fig. 27 shows two noteworthy peaks in February and July (though the second one is larger), each occurring one month earlier than the respective peaks in March and August of the present CAC in Fig. 33. The biannual variation mechanism present in the monthly AVISO data is mostly averaged away in CAC_raw with other inseparable variation mechanisms and noise. The CAC_raw EOF mode 2 loading vector in Fig. 31b shares little in

common with the monthly EOF mode 2 loading vector in Fig. 24b except for a strong anticyclone at 88°W. Additionally, CAC_raw EOF mode 3 and mode 4 loading vectors in Fig. 32 look nothing like monthly EOF mode 3 and mode 4 loading vectors in Fig. 25. Contrarily, the CAC_raw EOF mode 1 loading vector in Fig. 31a closely resembles the monthly EOF mode 1 loading vector in Fig. 24a. Both the CAC PCTS in Fig. 33a and the CAC of PCTS 1 in Fig. 27a follow an annual cycle remaining relatively stable from January through June, dropping to a minimum in October, and increasing to the end of the year. Since the first EOF mode of the monthly AVISO data and of the CAC of the monthly data (CAC_raw) are very similar and strongly annual, Loop Current intrusion and retreat is a mainly annual – not biannual – process.

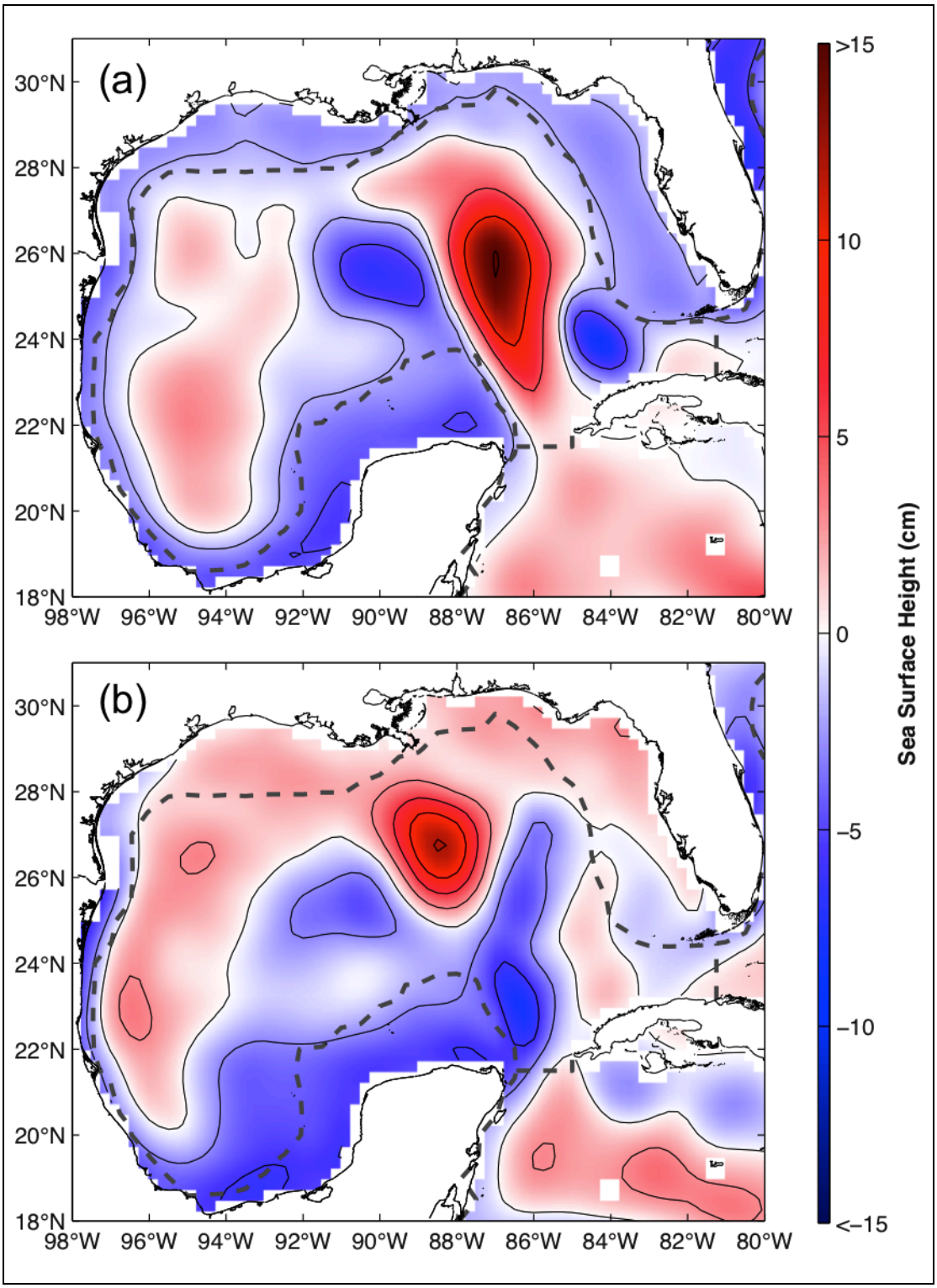

Fig. 31. CAC_raw deepwater (a) EOF mode 1 and (b) EOF mode 2. Mode 1 explains 43.0% of the variance. Black contours are at -5, -2, 0, 5, 10, and 15 cm. Mode 2 explains 30.2% of the variance. Black contours are at 3 cm intervals. Gray dashed lines signify the boundaries of the EOF decomposition. The lines follow the 200 m isobath everywhere except across the Yucatan Channel and Florida Straits.

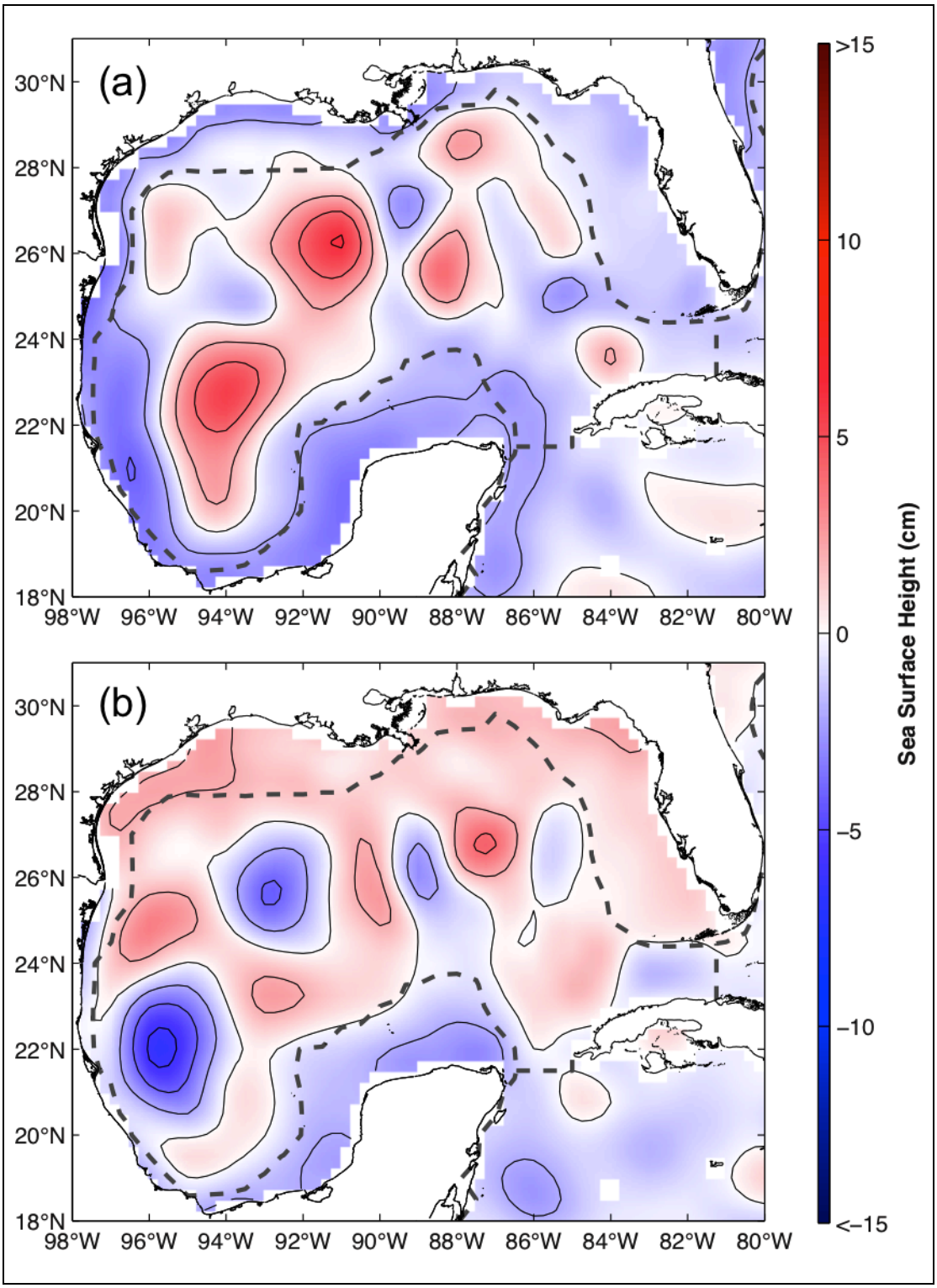

Fig. 32. CAC_raw deepwater (a) EOF mode 3 and (b) EOF mode 4. Mode 3 explains 10.7% of the variance, and mode 4 explains 8.6%. Black contours are at 2 cm intervals. Gray dashed lines signify the boundaries of the EOF decomposition. The lines follow the 200 m isobath everywhere except across the Yucatan Channel and Florida Straits.

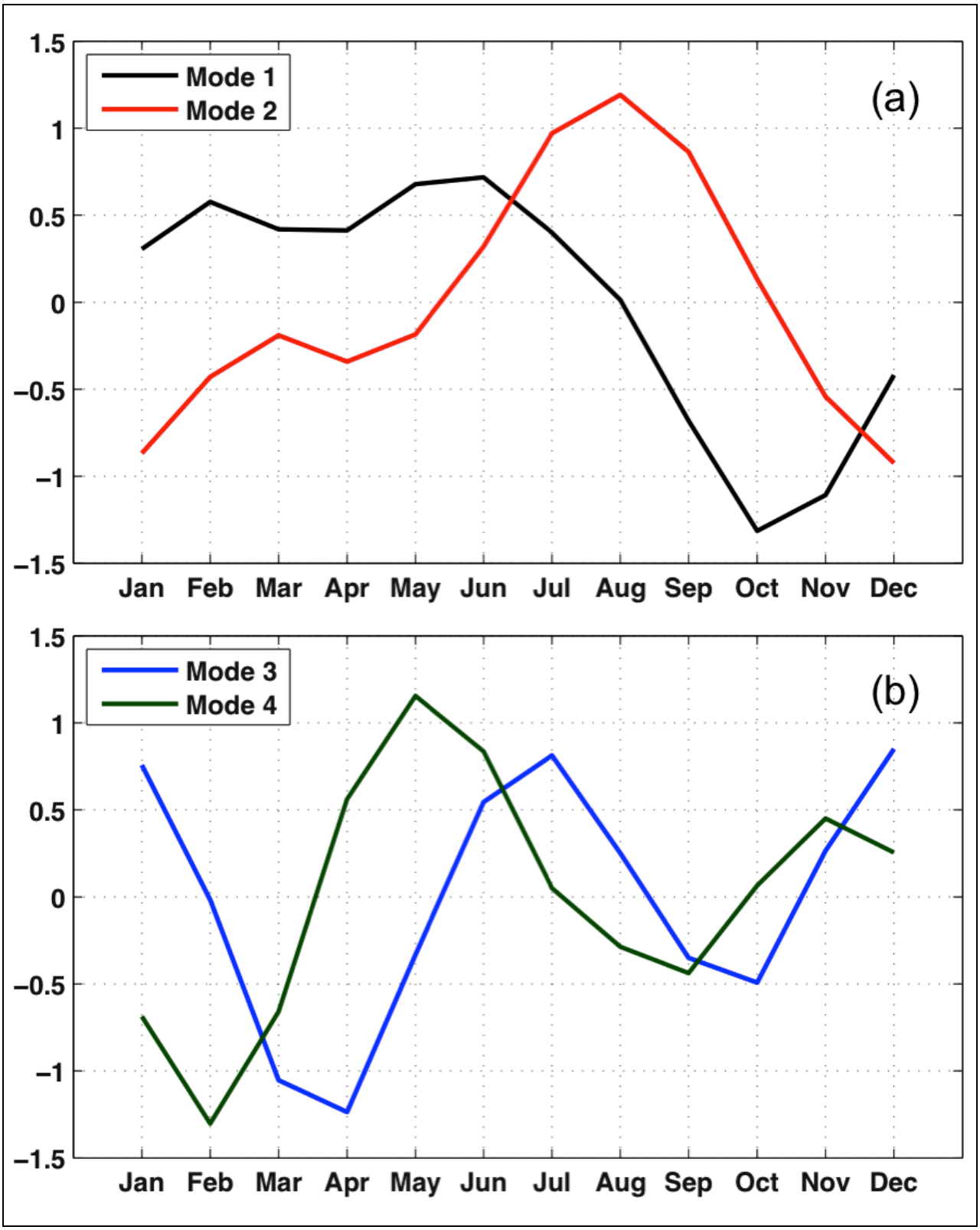

Fig. 33. CAC_raw deepwater principal component time series for EOF (a) Mode 1 and Mode 2 and (b) Mode 3 and Mode 4.

The LC metrics plotted in Figs. 29b and 30b demonstrate that the CAC of the first four EOF modes (CAC1234) captures most of the annual LC variability. Loading vectors of an EOF decomposition of CAC1234 are shown in Figs. 34 and 35. The CAC1234 EOF decomposition captures 100% of CAC1234 variability as expected in the first four modes: 66.4%, 28.9%, 4.3%, and 0.4%, respectively. Note, however, that these modes do not capture 100% of the variability in CAC_raw. Figures 36 and 37 show, respectively, LC northern latitude and area CAC metrics of different reconstructions of the first three EOF modes of CAC1234 in comparison to CAC_raw and CAC1234. For both northern latitude and area, CAC1234 is almost perfectly reproduced by the reconstruction of the first three modes only, which is not surprising since the fourth mode captures only 0.4% of the variance in CAC1234. The contribution of mode 4 to the seasonal signal is insignificant. The corresponding loading vector in Fig. 35b reflects minimal impact on the LC. Table 13 lists proportions of variances explained using different reconstructions of the first four EOFs of CAC1234 in comparison to CAC1234 and CAC_raw. The first three modes explain about 97% of the northern latitude and 93% of the area variance in the annual cycle of the original AVISO data (CAC_raw). Note that the EOF 1 loading vector in Fig. 34a closely resembles the CAC_raw EOF 1 loading vector in Fig. 31a. However EOF 2, 3, and 4 loading vectors in Figs. 34b and 35 do not match their CAC_raw EOF 2, 3, and 4 counterparts in Figs. 31b and 32. The EOF loading vectors corresponding to CAC1234 have much less extraneous variations and are, spatially, much less complex. The EOF processing and monthly averaging required to produce and decompose CAC1234 have reduced the degrees of freedom required to separate the dominant LC variability at seasonal time scales from the original monthly time series.

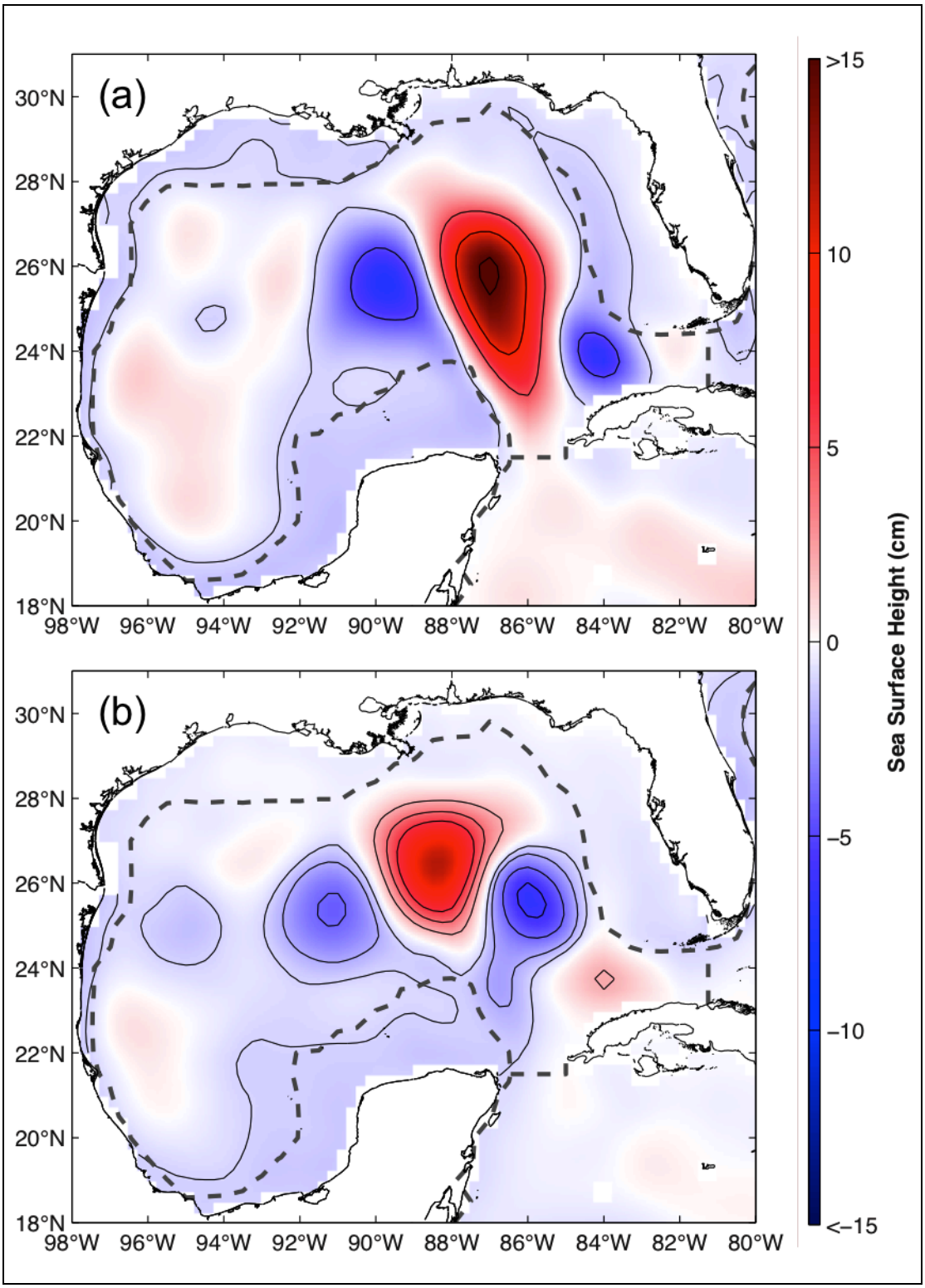

Fig. 34. CAC1234 deepwater (a) EOF mode 1 and (b) EOF mode 2. Mode 1 explains 66.4% of the variance. Black contours are at -5, -0.9, 5, 10, and 15 cm. Mode 2 explains 28.9% of the variance. Black contours are at -6, -4, -2, -1, 2, 4, and 6 cm. Gray dashed lines signify the boundaries of the EOF decomposition. The lines follow the 200 m isobath everywhere except across the Yucatan Channel and Florida Straits.

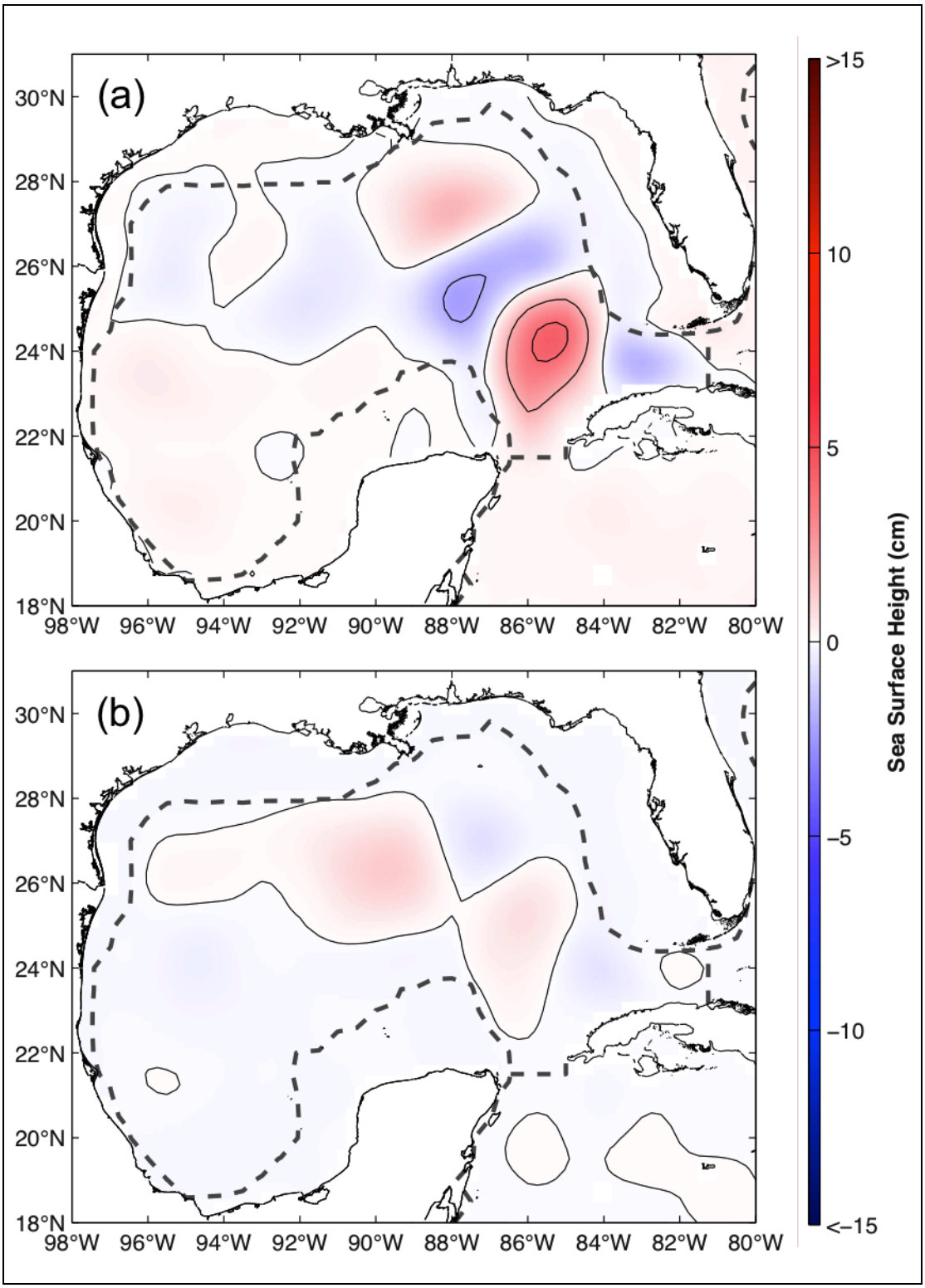

Fig. 35. CAC1234 deepwater (a) EOF mode 3 and (b) EOF mode 4. Mode 3 explains 4.3%, and mode 4 explains 0.4%. Black contours are at 2 cm intervals. Gray dashed lines signify the boundaries of the EOF decomposition. The lines follow the 200 m isobath everywhere except across the Yucatan Channel and Florida Straits.

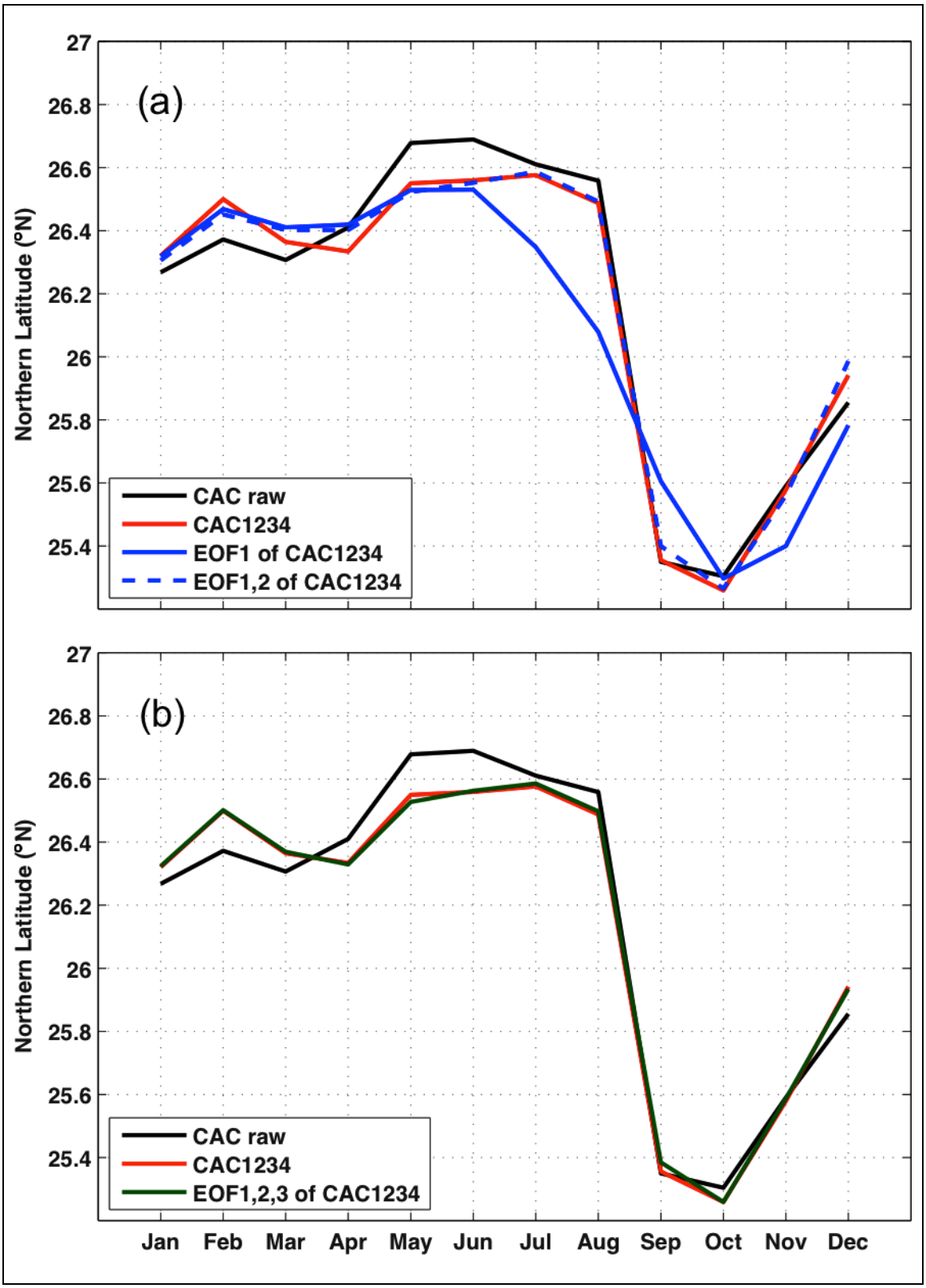

Fig. 36. Composite annual cycle of Loop Current northern boundary latitude. CAC_raw and CAC1234 are plotted with (a) CAC1234 EOF mode 1 and EOF modes 1 and 2 combined; (b) CAC1234 EOF modes 1, 2, and 3 combined.

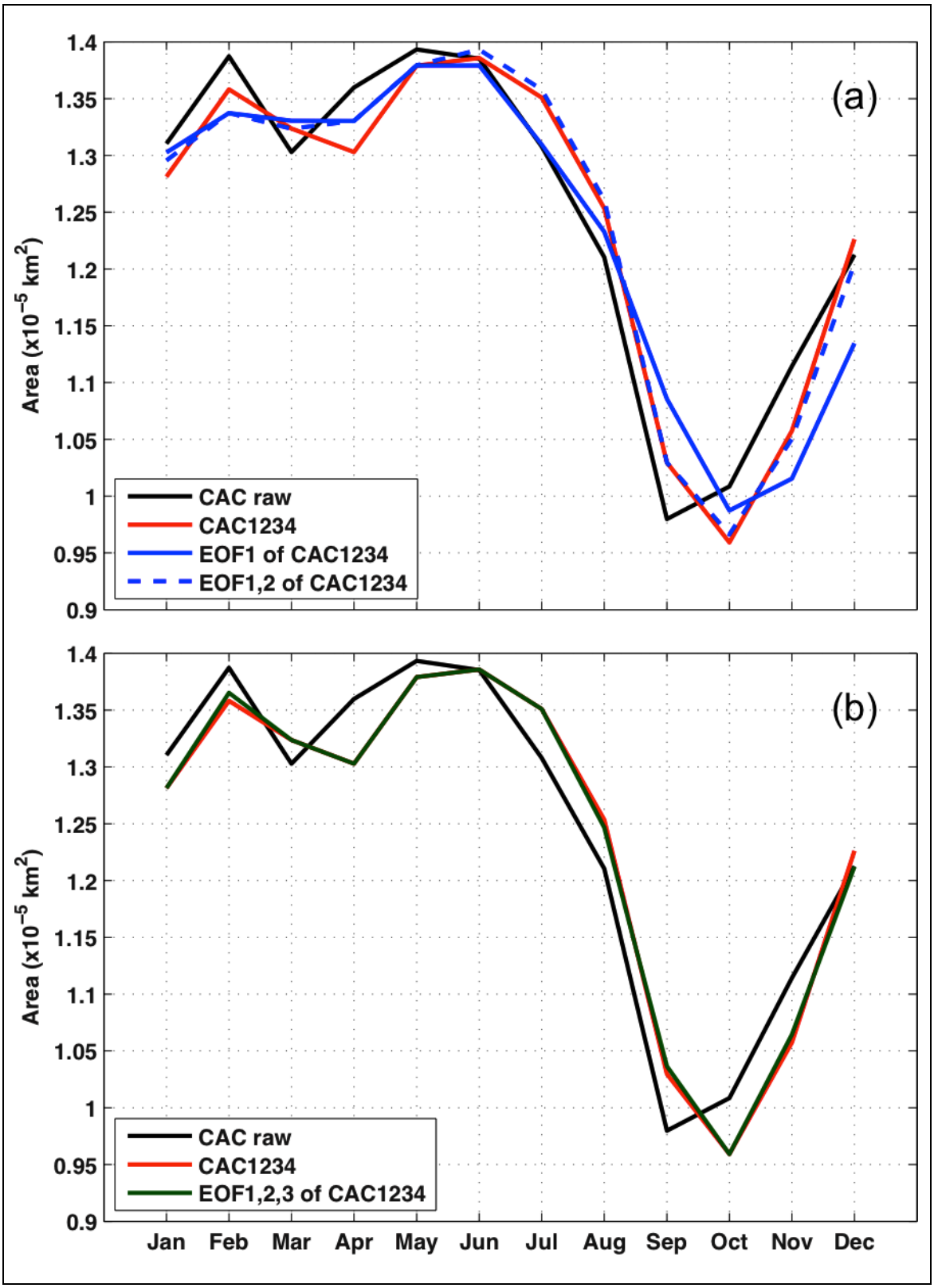

Fig. 37. Composite annual cycle of Loop Current area. CAC_raw and CAC1234 are plotted with (a) CAC1234 EOF mode 1 and EOF modes 1 and 2 combined; (b) CAC1234 EOF modes 1, 2, and 3 combined.

Table 13. Proportion of CAC_raw and CAC1234 Loop Current northern latitude and area variance explained by reconstructions of first four deepwater EOF modes of CAC1234.

	LC Northern Latitude Variance		LC Area Variance	
	CAC_raw	CAC1234	CAC_raw	CAC1234
EOF 1	0.8532	0.8801	0.8703	0.9265
EOF 1,2	0.9711	0.9952	0.9276	0.9915
EOF 1,2,3	0.9725	0.9994	0.9317	0.9984
EOF 1,2,3,4	0.9744	1.0000	0.9277	1.0000

The evidence presented so far of annual LC variability can be compared with the results published by Chang and Oey. Similar to Fig. 27, Chang and Oey (2013a) also shows CACs of EOF mode 1 and mode 2 PCTS (Fig. 10) derived from monthly AVISO data over the 18-year time period from 1993 through 2010. The authors describe the CACs as annual signals. Inconsistently, however, Chang and Oey (2013a) states in the abstract of that paper that a biannual signal is contained within the first two observational EOF modes. In Fig. 4 of Chang and Oey (2013a), the authors show the first two EOF modes of an ocean model, with the CACs of the PCTS showing clear biannual signals. Chang and Oey provide no explanation of why the model CACs are biannual but the observational CACs are annual. Figure 8c of Chang and Oey (2013a) shows six CAC monthly LC fronts, indicating relatively steady LC shape from January to March, LC intrusion from March to July, LC retreat from July to November, and LC intrusion again from November to January. All together, the fronts create an annual – not biannual – cycle with a maximum in July and minimum in November. Figure 8d is a Hovmöller CAC plot of SSH along the latitude 26.5°N (crossing the northern tip of the LC). Then Fig. 8e shows a CAC of maximum SSH along 26.5°N, based on Fig. 8d. Figure 8e is biannual and would be convincing if the results presented were achieved at a constant longitude. This would suggest that SSH and, thus, the LC varies biannually at a fixed point in space. However, the "maximum SSH" criterion enables capturing of the center of the January and June SSH peaks in Fig. 8d, though they occur at different locations. Therefore, the SSH line plotted in Fig. 8e is a function of latitude and "best" longitude. What does that mean? For the sake of argument, most LC metrics in Fig. 14 exhibit some biannual signal with local troughs in March or April and in October or November.

However, the error bars show that the troughs in March or April are not significant. Assuming stationarity, these spring troughs may become statistically significant with more observations but will still amount to only a small portion of seasonal LC variability.

Modeling methods in Chang and Oey (2013a) are ambiguous and questionable in several other respects. The authors explain that their GOM-Caribbean model incorporated "idealized" wind forcing. The modeled Caribbean wind is a biannual sinusoid, maximum westward in December and June and minimum westward in March and September. In contrast, observational wind data in Fig. 8a of Chang and Oey (2013a) show that Caribbean wind is biannual but asymmetric, maximum westward in January and July and minimum westward in May and September. The September minimums are consistent with observations. The modeled GOM winds were 180° out of phase with modeled Caribbean winds, with westward peaks in March and September and westward minimums in December and June. The modeled westward maximums do not match observed GOM wind peaks in either May or October. The modeled minimum in December matches the observed December/January minimum, but the modeled June minimum does not match the observed August minimum. Table 2 of Chang and Oey (2013a) indicates that the model run chosen for most of the analyses in the paper, "Exp.Carib" (or just "Carib"), showed most LCEs separating in the months of June, December, and January, times when LCEs are unlikely to separate in reality. The model is not only inconsistent with the results and various published LCE separation date lists mentioned in Chapter V, but also with the authors' own seasonal histogram shown in Fig. 1a of Chang and Oey (2012). Chang and Oey (2013a) attributes the discrepancy between the peak LCE separation months in the model and observations to both the misalignment of the modeled wind peaks with the observed wind peaks and the symmetry of the modeled wind signal in comparison to the asymmetry of the observed wind data. In a separate comparison the authors also attribute some of the discrepancy between modeled and observed north Caribbean CAC monthly maps (Fig. 9) to the "idealized" wind forcing in the model. It would have been "more ideal" if the authors had made modeled winds in Chang and Oey (2013a) as realistic as possible, incorporating the observational winds they

already had on-hand (Fig. 8a). This way, any discrepancies between modeled results and observations could not be easily dismissed because of discrepancies in the wind forcing.

Chang and Oey (2013a) also notes that two of the four model runs the authors performed, "Exp.Carib" and "Exp.GOMCarib," show similar results. Peak eddy shedding months are June, December, and January for both. The results of these two model runs contradict previous findings in Chang and Oey (2010), which argued that strong GOM easterlies delay eddy separation. Both "Exp.Carib" and "Exp.GOMCarib" incorporate winds over the northwestern Caribbean Sea, but only "Exp.GOMCarib" incorporates winds over the GOM also. If the same peak shedding times can be achieved with and without GOM winds, the GOM winds must not be causing any significant delay. The other two model runs the authors performed in Chang and Oey (2013a), "Steady22Sv," with only far-field forcing, and "Exp.GOM," incorporating GOM winds as well, show no seasonal preference for eddy separation. "Steady22Sv" eddy separation periods are seven and eight months, while "Exp.GOM" separation periods are *six*, seven, and eight months. The authors state that though the GOM winds in "Exp.GOM" do not cause seasonal preference, they still have the effect of delaying separation. How can the authors make this assertion when eddy separation periods of the model run "Steady22Sv" (without GOM winds) yield the same or even longer separation periods than "Exp.GOM"? If anything, it seems that the GOM winds accelerate separation.

Both Chang and Oey (2012) and Chang and Oey (2013a) use a Yucatan Channel transport CAC from Rousset and Beal (2010) to support their modeling result that the biannual LCE shedding is caused by biannual transport variations in the Yucatan Channel. Chang and Oey (2013a) says that Rousset and Beal (2010) found a "significant biannual transport variation," which is misleading since Rousset and Beal actually said that the "statistical significance of these [transport] results is marginal" and never specifically described a biannual variation of any kind anywhere in the paper. Figure 9e of Chang and Oey (2013a) presents a biannually varying CAC of SSHA within a specific domain capturing the Yucatan Channel and northern Caribbean Sea (17.5°N-22.5°N, 87°W-80°W), which the authors use to imply that SSHA variations in the

region force biannual Yucatan Channel variations. The SSHA CAC does look somewhat like the Yucatan transport CAC in Fig. 4b of Rousset and Beal (2010). However, the SSH anomalies that appear in the northern Caribbean Sea do not seem to propagate through the Channel in the corresponding CAC map set in Figs. 9b and 9d. Evidence of a connection between SSHA and transport requires more extensive transport studies and more rigorous analyses. Overall, the evidence that Chang and Oey have presented for a biannually varying LC is not very convincing. There may, in fact, be some biannual transport through the Yucatan Channel forcing the LC, but that variation must account for only a small fraction of LC variability. Note that even the eddy separation events associated with the LC (Chapters II, III, IV, and V) do not strictly show biannual power – only seasonal– since they often occur only once a year either in the spring or the fall.

In stark contrast to Chang and Oey's results, all of the EOF analyses presented in this chapter indicate that variations of the LC itself are dominantly annual. Further inspection of the first two EOF loading vectors shown in Fig. 34 indicates that annual LC variability is linked to coastal anomalies. The EOF 1 loading vector shows a nearly continuous low SSH anomaly around the entire GOM shelf. The EOF 2 loading vector also shows a strong anomaly on the Campeche Bank. In the following section, I show results from a *coastal* EOF analysis to independently verify the result that the LC covaries with shelf signals and to identify coastal forcing as the likely dynamical source of the dominant LC annual variability.

Coastal EOF Analysis and Kelvin Wave Dynamics

Sea level measurements from coastal tide gauges and satellite altimetry show that interannual sea level signal extends all around the GOM and may be both remotely and locally forced (Li and Clarke, 2005). Remotely forced interannual sea level signal propagates along the U.S. Atlantic coast and into the GOM as coastal Kelvin waves. Some of the coastal signal is forced by interannual Rossby waves that form in the Atlantic, propagate westward, cross the Gulf Stream, and impinge on the coast. Coastal Kelvin waves are generated as the Rossby waves reflect off of the southeast U.S. Atlantic coast. This proposed mechanism is consistent with observations that show that the interannual sea level signal on the coast is driven by wind stress curl over the Atlantic and oceanic Rossby wave propagation to the coast (Hong et al., 2000) and with the high correlation found between U.S. east coast annual mean sea level and sea level along the northern coast of the GOM (Maul and Hanson, 1991). Along the northern GOM shelf the remotely forced interannual coastal signal is amplified from Pensacola to the Louisiana-Texas shelf by interannual alongshore wind forcing (Li and Clarke, 2005).

Li and Clarke (2005) identified what appeared to be interannual coastal Kelvin signals in the first EOF mode of historical monthly tide gauge data (1986-2002) collected at 12 locations along the U.S. coast from Wilmington, North Carolina to Port Isabel, Texas. The first EOF mode captured 70% of the variance in the tide gauge measurements, indicating an in-phase (at monthly resolution) signal spanning nearly 4500 km along the coast. Coastal EOF analyses were performed using monthly gridded ¼° AVISO SSH from 1993 through 2012 and compared with the tide gauge results in Li and Clarke (2005) to ensure that the AVISO data in shallow waters were reliable in the GOM. Near-coast SSH measurements are often excluded from gridded altimeter data products since wet tropospheric, high-frequency oceanographic, tidal, and other corrections applied to the altimetric range measurement tend to cause errors in the SSH values within 25 to 50 km of the coast (Saraceno et al., 2008). Consistent with the Li and Clarke (2005) analysis, the CAC was removed from the AVISO time series, and the data were low-pass-filtered using the Lanczos filter described in Trenberth (1984) to retain only interannual frequencies. After additionally detrending the data, all data in waters deeper than *500 m* were masked to

isolate the sea level variations on the shelf and continental slope, and an EOF decomposition was then performed over the domain 98°W-70°W, 18°N-35°N. The EOF bounds were sufficiently far north to include the zone where the Kelvin waves originate along the U.S. east coast and sufficiently far south to allow detection of Kelvin waves along the Gulf and northwestern Caribbean Sea coasts. The resulting PCTS and original SSH were used to project the signal into the deepwater, yielding the monthly "low-passed" coastal EOF mode 1 loading vector shown in Fig. 38a. A second coastal EOF decomposition was performed on the monthly AVISO data without removing the CAC or low-pass filtering the data. This "raw" monthly coastal EOF mode 1 (CM1) loading vector is shown in Fig. 38b for comparison. The low-passed EOF mode 1 explains 60.4% of the low-frequency coastal AVISO variance, whereas CM1 explains 70.6% of the unfiltered coastal AVISO variance. Gray dashed lines in the Fig. 38 maps designate the 500 m isobath. Loading vector sea level at the 12 tide gauge coastal locations from Fig. 3 of Li and Clarke (2005) are plotted with corresponding loading vector sea surface heights in Fig. 39a. The low-passed loading vector SSH closely approximates the tide gauge loading vector from Wilmington, North Carolina to about Pensacola, Florida, 2550 km down the coast. Beyond that point, the two loading vectors decorrelate. Figure 39b shows the PCTS of the first tide gauge and AVISO coastal EOF modes. Note that though Li and Clarke (2005) used tide gauge data from 1986 through 2002, only tide gauge PCTS results from roughly June of 1993 into October 2001 were given. The correlation between the tide gauge PCTS and the low-passed AVISO PCTS is 0.5941, which is quite good considering the differences in the processing of the two datasets. There are several key differences: 1) EOF decompositions of the altimetry were not performed over the same time period as the tide gauge data since reliable gridded satellite altimetry products cannot be made prior to late 1992; 2) the AVISO analysis includes both shelf and slope variability; and 3) altimetry-derived values in the AVISO maps at the tide gauge locations are extrapolated from altimeter measurements further offshore. Given these processing differences and possible sources of error, the similarity of the two EOF analyses indicates that coastal AVISO data analyses are able to resolve most of the dominant signal observed by the coastal tide gauges.

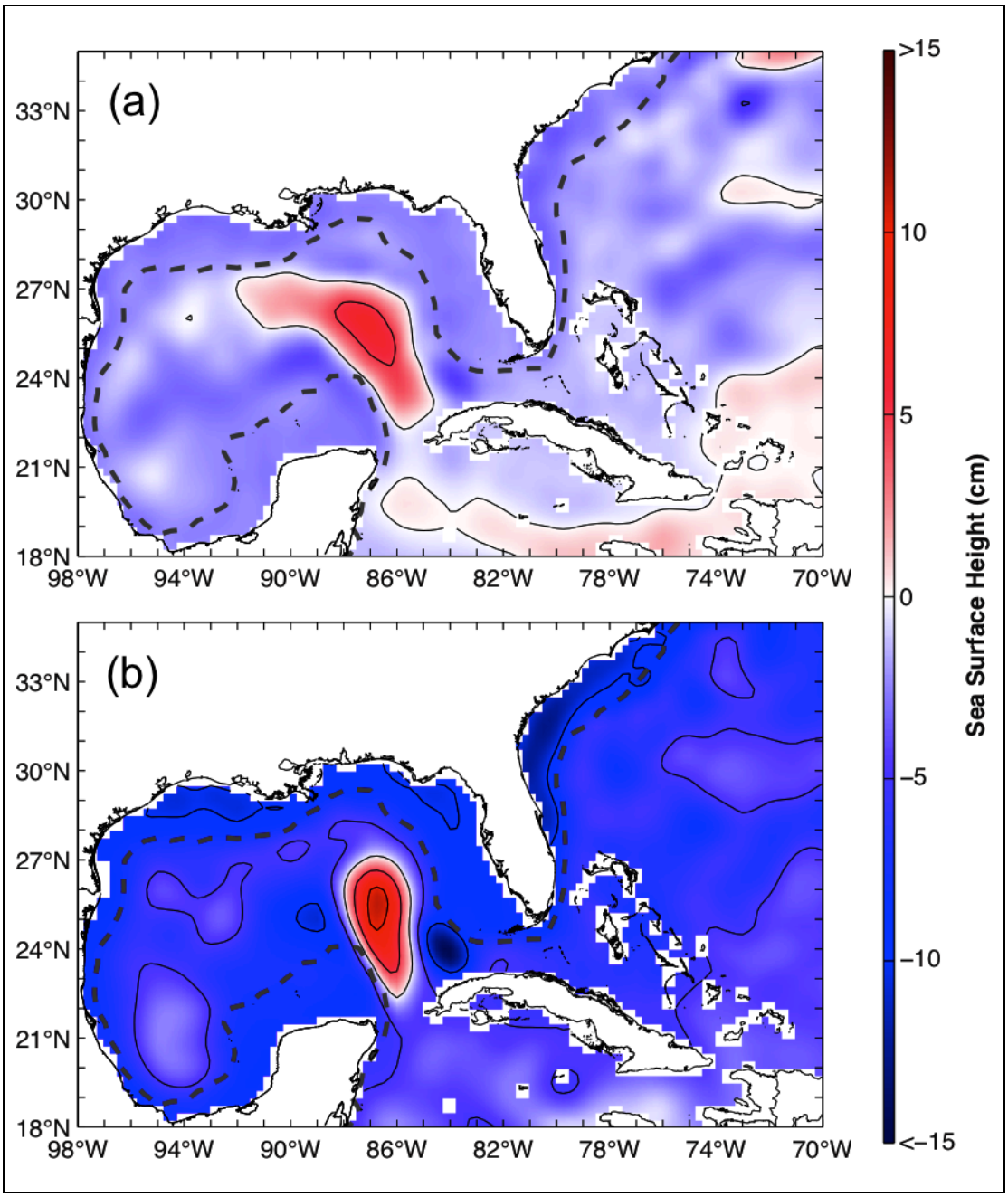

Fig. 38. Coastal EOF mode 1 loading vector derived with monthly AVISO data from 1993 through 2012 (a) with composite annual cycle removed, low-pass-filtered using Lanczos filter design presented in Trenberth (1984), and detrended; (b) unfiltered (CM1). Black contours are at 5 cm intervals. Gray dashed lines follow the 500 m isobath and signify the boundaries of the EOF decomposition.

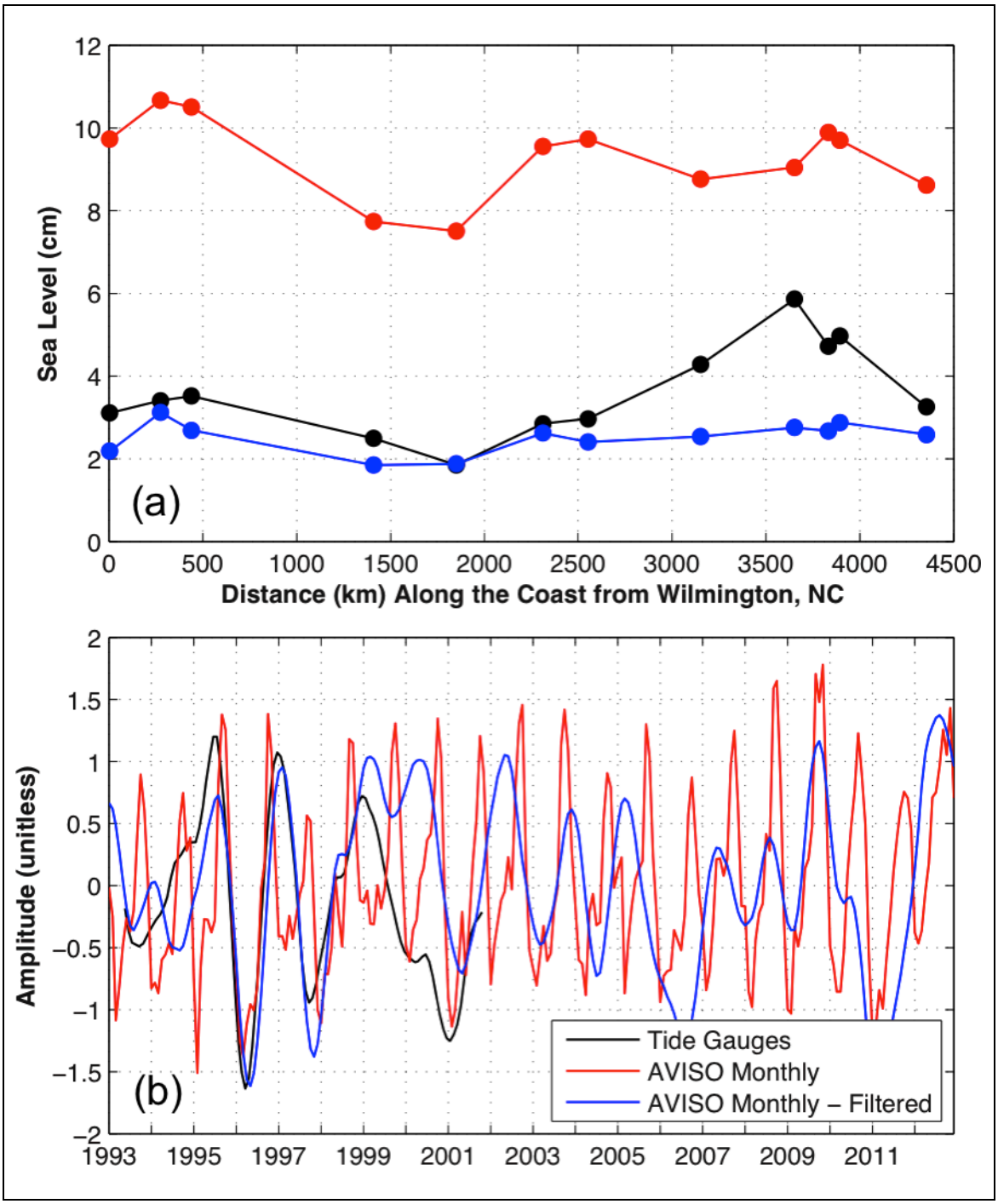

Fig. 39. Interannual EOF mode 1 (black) from monthly tide gauge sea surface height data for June 1993 through October 2001 (Li and Clarke, 2005) compared to EOF mode 1 derived from coastal AVISO sea surface height data low-pass-filtered with composite annual cycle and linear trend removed (blue) and unfiltered (red). (a) shows loading vector sea levels at specific distances along the coast south of Wilmington, North Carolina. (b) shows corresponding principal component time series.

Veracity of the near-coast AVISO data was also tested by analysis of the northward boundary current speeds using the CAC_raw SSH dataset. Note that CAC_raw was created from unmasked monthly AVISO data and possesses no intrinsic deepwater or coastal characteristics associated with the various EOF decompositions presented herein. Northward geostrophic speed anomalies were computed in the GOM Western Boundary Current at 25.25°N between 97.5°W and 95.5°W using CAC_raw and were compared with Western Boundary Current ship drift speed anomalies from Sturges (1993) in Fig. 40a. Ship drift speeds fall within the 95% confidence interval (N = 20, t-score = 2.093) error bars for all months except February and April, indicating that the near-shore geostrophic speeds derived from CAC_raw coastal SSH are reliable. Figure 40b plots the derived GOM Western Boundary Current northward geostrophic speed anomaly CAC with CACs derived from Florida Current speed anomalies at 27.0°N between 80°W and 79°W and from Yucatan Current speed anomalies at 21.75°N between 86.75°W and 84.75°W. The CACs are consistent among the three currents in both speed and annual variation. Note that there is very little biannual variability in any of the western boundary currents.

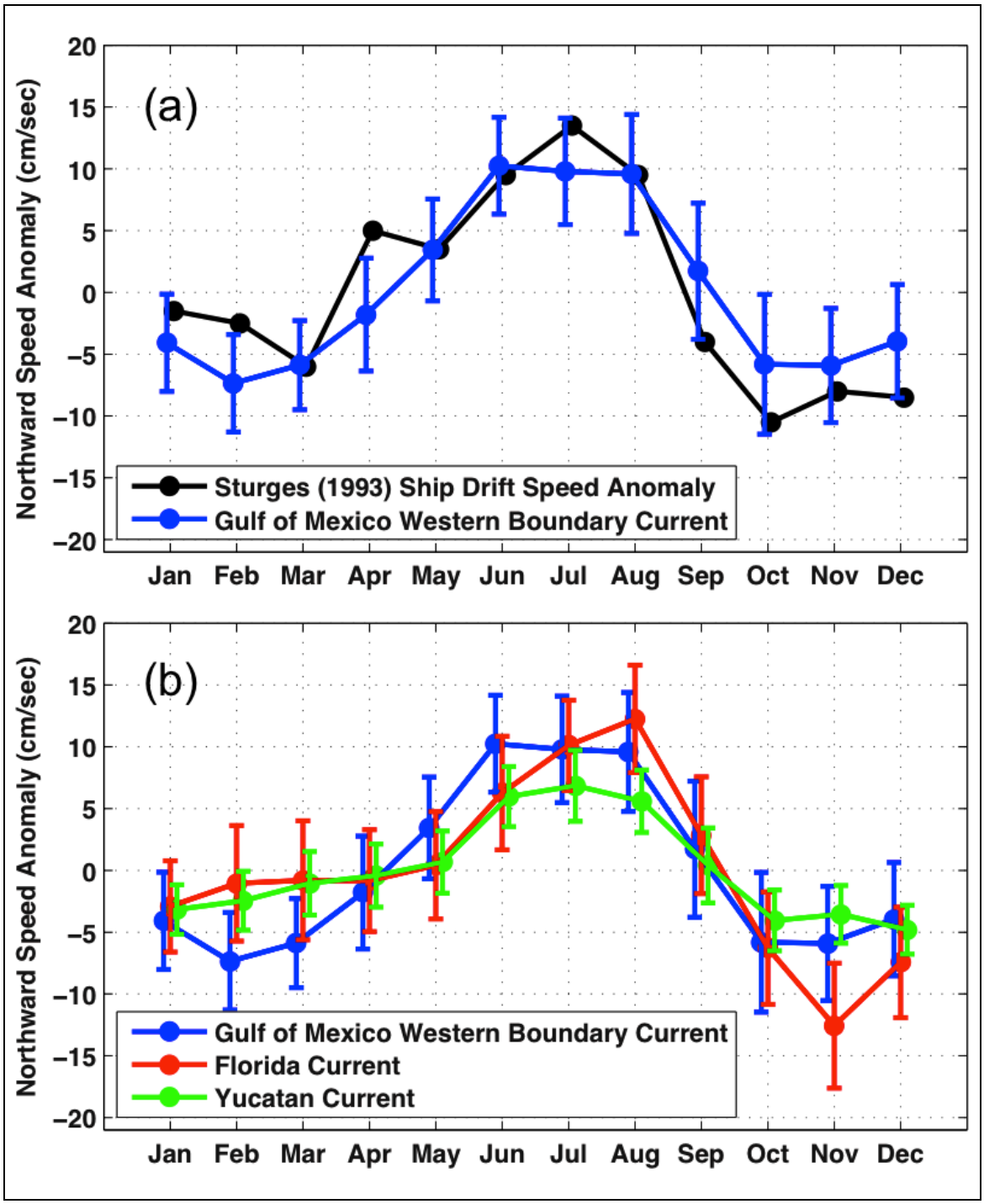

Fig. 40. (a) GOM Western Boundary Current ship drift speed anomaly composite annual cycle (Sturges, 1993) as compared to the northward geostrophic speed anomaly derived from CAC_raw. (b) Northward geostrophic speed anomalies derived from CAC_raw within the GOM Western Boundary Current, the Florida Current, and the Yucatan Current. Speed anomalies were computed in the GOM Western Boundary Current at 25.25°N between 97.5°W and 95.5°W, in the Florida Current at 27°N between 80°W and 79°W, and in the Yucatan Current at 21.75°N between 86.75°W and 84.75°W. Error bars are 95% confidence intervals (N = 20, t-score = 2.093).

Since comparison of the AVISO SSH with independent datasets indicates that coastal AVISO SSH data are valid, CM1 shown in Fig. 41b can be compared with the first deepwater EOF loading vector derived from CAC1234 in Fig. 41a. The two loading vectors are very similar in that they both show large anticyclones over the LC and noticeable shelf signals as well, though the coastal loading vector shows a stronger coastal signal, as would be expected. The SSH correlation between the two loading vectors in the deepwater (deeper than 200 m) is 0.93 and is 0.85 overall. Figure 42 compares the CAC of deepwater EOF PCTS 1 (from Fig. 27) with the PCTS CAC of CM1. (Comparison of CAC_raw PCTS 1 with the PCTS CAC of CM1 would also be valid.) Both deepwater and coastal PCTS are relatively high from January through June and identically reach a low in October. The PCTS CAC of CM1 has a higher peak and trough than deepwater CAC of PCTS 1 likely due to the annual nature of the steric signal, present only in the coastal EOF results. Figure 43a shows the sum of monthly variance of the AVISO data, and Fig. 43b provides the fraction of that variance contained within a monthly reconstruction of CM1. Variance explained is greater than 10% on the coast all the way around the GOM from the West Florida Shelf to the Campeche Bank and within the LC. Variance explained is greater than 50% in some areas of the northern shelf.

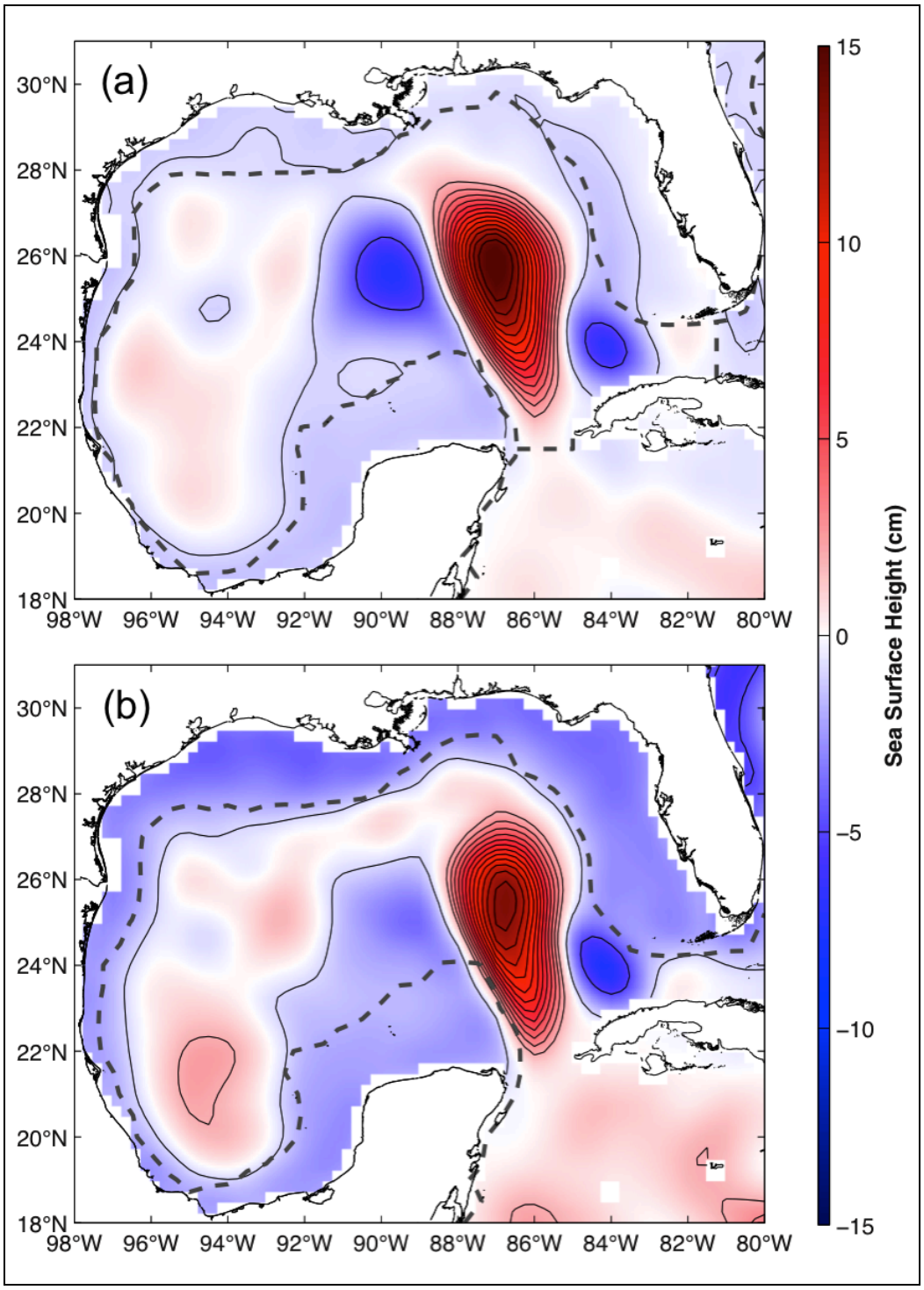

Fig. 41. (a) CAC1234 EOF mode 1 loading vector (same as in Fig. 34a). Gray dashed lines signify the boundaries of the EOF decomposition. The lines follow the 200 m isobath everywhere except across the Yucatan Channel and Florida Straits. (b) CM1 loading vector with 5.07 cm offset applied. Gray dashed lines follow the 500 m isobath and signify the boundaries of the EOF decomposition. Black contours are at -5, -0.9, and 2 cm and then upwards at an interval of 2 cm for both (a) and (b).

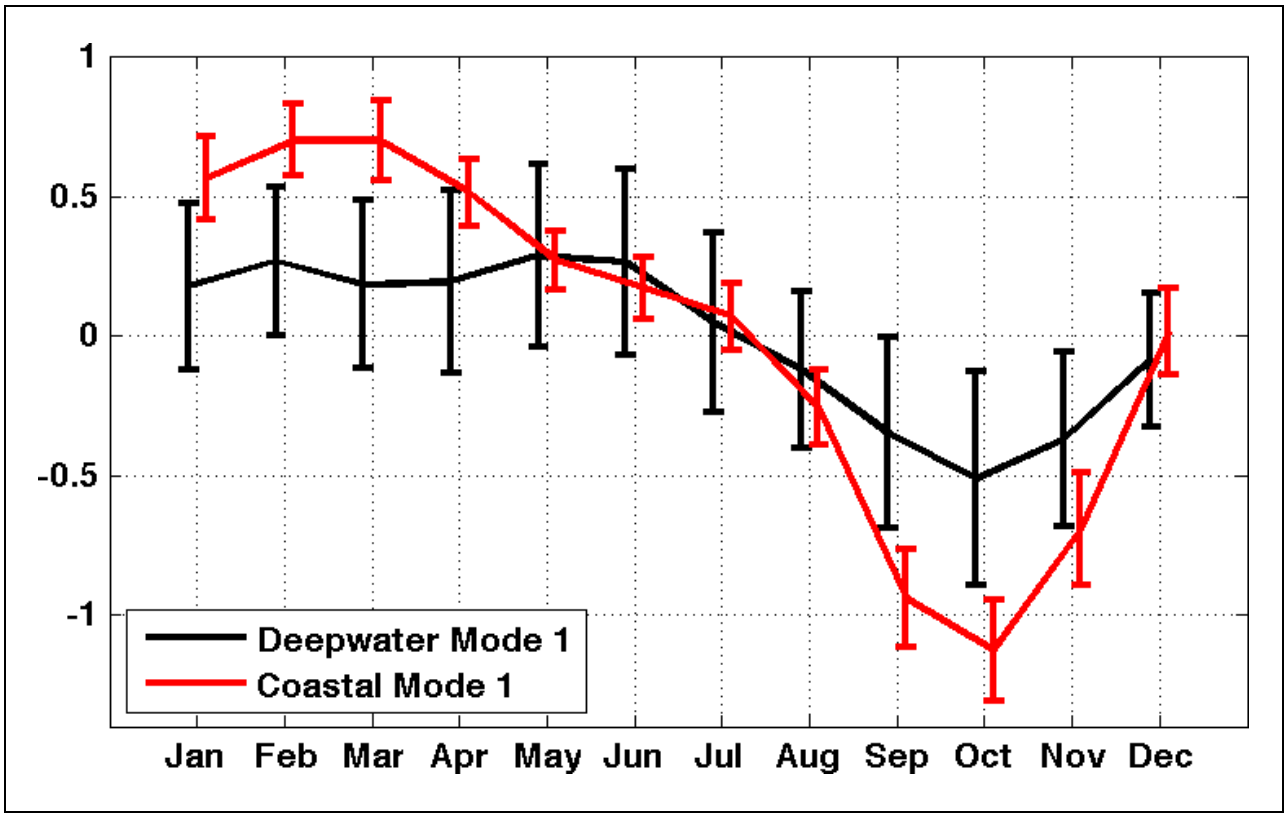

Fig. 42. Composite annual cycles generated from deepwater EOF principal component time series mode 1 and coastal EOF principle component time series mode 1 (CM1). Error bars are 95% confidence intervals (N = 20, t-score = 2.093).

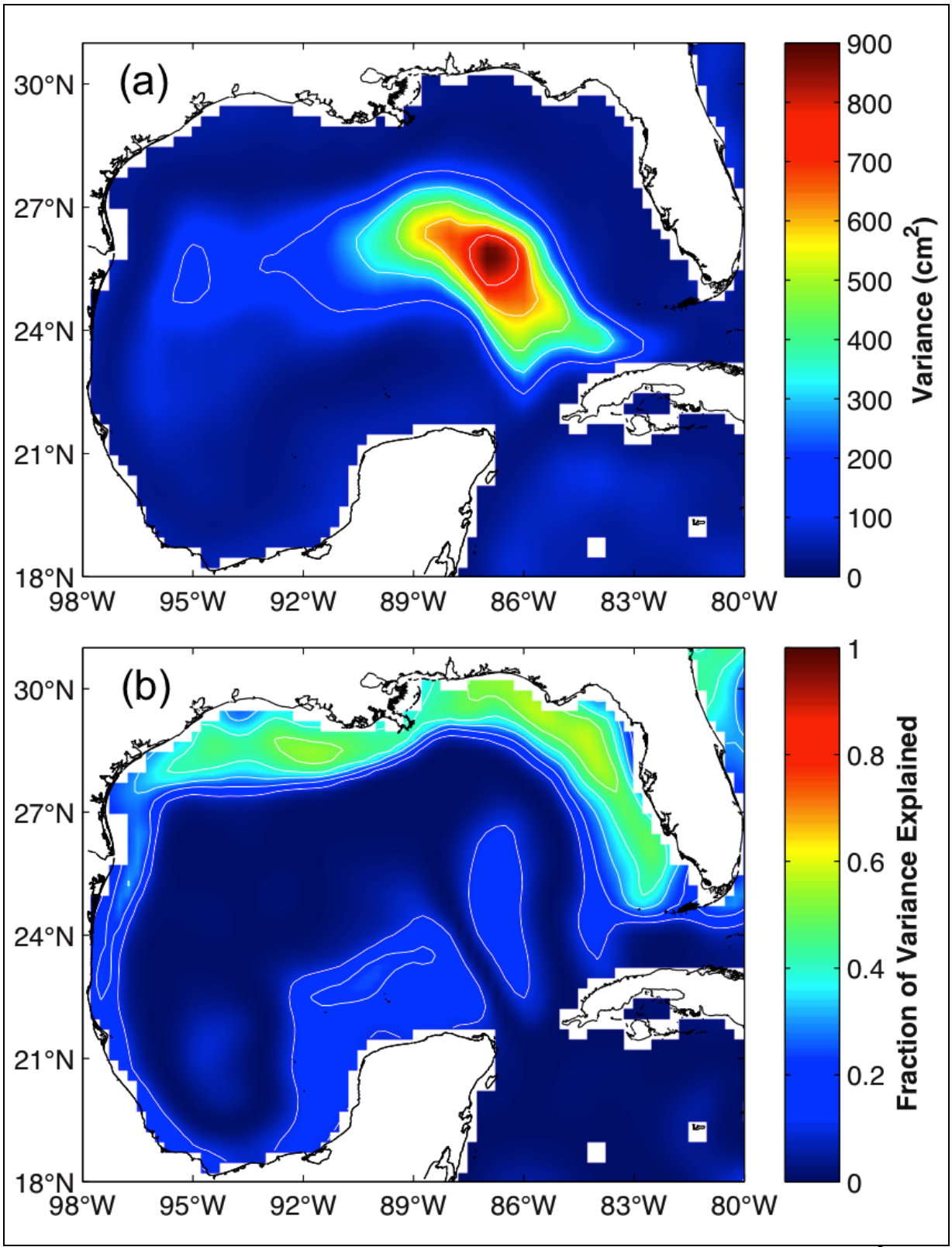

Fig. 43. (a) Sum variance of monthly AVISO maps. The contour increment is 150 cm^2. (b) Fraction of total variance generated by monthly reconstruction of CM1. The contour increment is 0.1.

Figure 44a compares the LC northern latitude metric of CAC_raw, CAC1234, and the CAC of the monthly CM1 reconstruction, while Fig. 44b shows a similar comparison with LC area. Though no LC variance was included in the coastal EOF decomposition, LC variance correlated with the coastal signal in the deepwater accounts for a large portion of the variance in the complete AVISO CAC, CAC_raw. Table 14 shows the proportion of CAC_raw and CAC1234 variance explained by the CAC of the monthly CM1 reconstruction for both LC metrics. The proportions in the table indicate that the CAC of the monthly CM1 reconstruction comes closer to approximating true LC area than LC intrusion/retreat characteristics. Minimum and maximum area values are approximately reproduced; only minimum northern latitudes are reproduced. In Fig. 44a, the CAC of CM1 remains close in magnitude to CAC_raw from January through April. Then it drops below CAC_raw, providing a poor approximation to observed northern latitude from May through August. Then from September through December, it follows true northern latitude closely. For area in Fig. 44b, the CAC of CM1 shows a similar trend as described for northern latitude from January through August. Then the CAC of the monthly CM1 reconstruction closely resembles CAC1234 for the rest of the year.

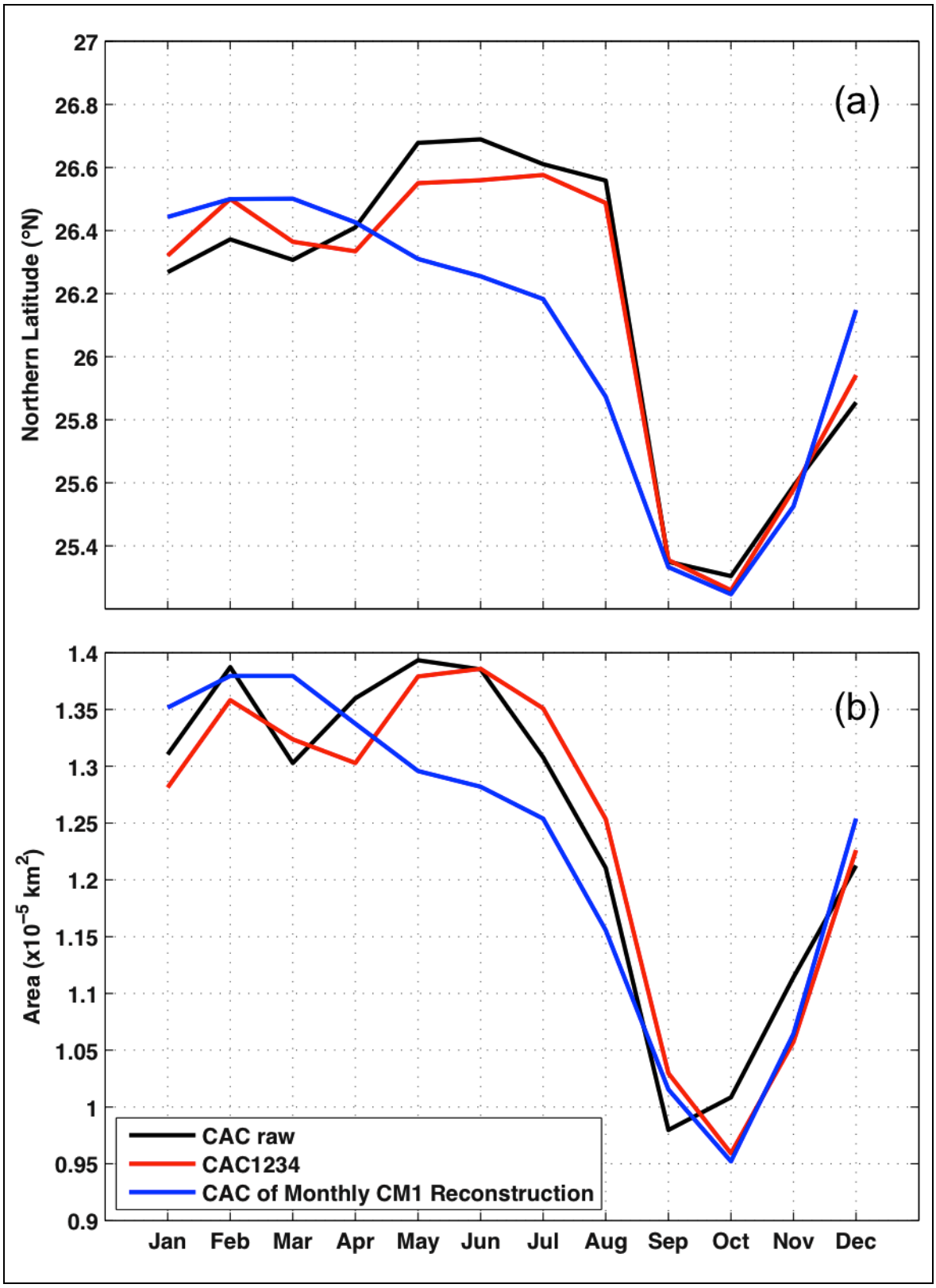

Fig. 44. (a) Composite annual cycle of Loop Current northern boundary latitude. (b) Composite annual cycle of Loop Current area. Each of the two subplots shows CAC_raw, CAC1234, and composite annual cycle of monthly CM1 reconstruction.

Table 14. Proportion of CAC_raw and CAC1234 Loop Current northern latitude and area variance explained by the monthly reconstruction of CM1.

	CAC_raw	CAC1234
LC Northern Latitude Variance	0.65	0.75
LC Area Variance	0.85	0.82

Clearly there is a close connection between CM1 and the dominant LC annual variability. The question then is why do the Kelvin waves have such a dramatic affect on the LC? At interannual time scales, flow on the shelf and at the shelf edge induces parallel flow in the adjacent deepwater as discussed by Li and Clarke (2005). Beyond the shelf break the shelf wave SSH signal decays causing seaward changes in geostrophic velocities along the continental slope. These deepwater near-shelf flow velocities vary depending on the orientation of the shelf, but western boundaries theoretically induce the highest current speeds. In the GOM the Campeche Bank acts as a western boundary for the LC, which rapidly dissipates Kelvin wave energy in the form of eastward propagating Rossby waves. The resulting changes in SSH at the shelf break induce a high velocity jet over the continental slope that can either accelerate or decelerate the LC flow depending on the sign of the waves. The dynamics involved are valid at both annual and interannual frequencies. This effect may not be directly resolvable by satellite altimetry since the shelf SSH break gradient is large over only a short distance; however, the net effect at seasonal, annual, and interannual time scales is apparent in the response of the LC in deepwater at these timescales. Reid (1972) has explained this type of LC response using a simple vorticity model that predicts the LC northern penetration as a function of current speed at the northern Campeche Bank shelf break and the departure angle of the LC at the shelf break. Greater current speed results in greater LC penetration for a fixed departure angle. Thus, Kelvin waves propagating along the GOM coast can and do affect LC variability through the generation of along-slope currents. This seems to be the dominant mechanism forcing the observed annual variably in the LC.

However, the Kelvin waves do not directly link variability in the LC to the seasonal tendency of LCE separation. The spring LCE seasonal peak (February/March) occurs when the

LC is substantially intruded. Even with fluid loss as LCEs separate, the LC on average continues to intrude in the months April, May, and June according to Fig. 44a (CAC_raw line). In contrast, the fall LCE seasonal peak (August/September) occurs when Kelvin waves are causing the LC to retreat. As such, it is unclear whether the Kelvin waves are the indirect cause of both LCE separation seasons, neither, one, or the other.

CHAPTER VII

CONCLUSIONS

Just as in the pre-altimetry era, separation dates derived from altimetry data are very much author-dependent in spite of the fact that most authors are using similar altimetry products. The pre-altimetry and altimetry time periods were compared to determine in which time period LCE separation dates were more consistent. Revisiting Table 3 pre-altimetry dates, 29% (six) of the 21 listed events (both numbered and unnumbered events) were only identified by one date list, the reanalysis or Vukovich (2012), not both. Similarly, 30% (nine) of the 30 listed altimetry events in Table 7 occurring from 1993 through 2009 (both numbered and unnumbered events) were unacknowledged by at least one of the date lists. This means that uniformity of LCE separation event identification has remained a problem regardless of GOM data used. For the pre-altimetry time period, LCE event dates vary among authors due to poor data quality and seasonal satellite data outages. Now with higher-quality altimetry data, LCE counts still differ among authors due to application of different eddy size, lifetime, and propagation criteria, allowance of short-period events, and ambiguity of separation status (detachment or separation). Of the 15 concordant pre-altimetry events, reanalysis and Vukovich (2012) dates differed by a month or less for 73% (11) of the events (ignoring day-of-month). Slightly better, 81% (17) of the 21 concordant altimetry events in Table 7 differed by one month or less. Lastly, 20% (three) of the concordant pre-altimetry dates and 0% of the concordant altimetry dates differed by three months or greater. These results indicate that the altimetry dates have better agreement overall than the pre-altimetry dates, especially since a total of four altimetry date lists exhibited more consistency than only two pre-altimetry date lists. As the use of more accurate SSH data in combination with objective tracking techniques improves, LCE separation dates will likely become more consistent in the future.

In contrast to the new pre-altimetry reanalysis dates derived for this dissertation, previously published pre-altimetry LCE separation dates do not exhibit seasonality. The reanalysis date list is thought to be more accurate than older date lists because the reanalysis is

based on a more complete observational record and a careful reanalysis of that record. In addition, reanalysis significance testing results are relatively consistent with altimetry-based results – that is, both the reanalysis dates and the dates from most altimetry lists show a significant LCE separation peak in the late summer/early fall – and most altimetry date lists are consistent with each other. Nevertheless, identification of LCE separation events in the pre-altimetry datasets (SST, chlorophyll-a, EddyWatch^{TM}) is necessarily subjective. Caution is advised when using these data in combination with the more objective and quantitative altimetric record to detect subtle changes in long-term climate trends or seasonality since changes found could be an artifact of the heterogeneous observational record.

Analyses shown indicate at the 95% confidence level that the LC follows a seasonal pattern throughout the year. Figure 14 shows with a variety of LC metrics using three separate altimetry datasets that LC characteristics are different at some times of the year (February) than at others (October and November). Statistical tests using χ^2 on most date lists indicate that there is seasonal preference to the timing of LCE separation since the distribution is not uniform. Randomization tests indicate that separations are most likely to occur in September and possibly March. Events are unlikely to happen in December. LCE separation events can be split into two seasons, the "spring" centered around Mar. 2 and the "fall" centered around Aug. 23. The boundaries between these two seasons are approximately May 22 and Dec. 3.

LC variability is mainly annual. Altimeter-derived LC northern boundary latitude and area metrics are relatively high from January through about July and low in September and October. The first three deepwater EOF modes of CAC1234 capture about 97% and 93% of the annual variability of LC northern latitude and area, respectively. Biannual LC variability is insignificant. It appears that annual and interannual GOM coastal Kelvin waves, energized mostly by wind stress curl in the Atlantic and alongshore wind in the GOM, are responsible for a large portion of LC variability. The CAC of the monthly CM1 reconstruction explains 65% of the variance in LC northern boundary latitude and 85% of the variance in LC area.

CHAPTER VIII

FUTURE WORK

Though the provided results have demonstrated LC seasonality, this study has raised several new questions. For instance, in Chapter IV, I derived LCE separation event dates for the altimetry time period (1993-2012) using only satellite altimetry data products. If I were to derive those same event dates again using SST, ocean color, and maybe other available in situ data, how would those dates compare to my altimetry dates? Would those dates show seasonal preference also? LCE separation timing seems to be bimodal, occurring in the late winter/early spring ("spring") or in the late summer/early fall ("fall"). However, LC intrusion and retreat is an annual process. Why the difference? Is LCE shedding in the spring season triggered by LC intrusion and shedding in the fall season triggered by LC retreat? The coastal EOF analysis in Chapter VI, section II discussed only the first EOF mode, CM1. What are the characteristics of the other coastal EOF modes? Do they contribute to LC seasonality? These questions will be the focus of future work.

BIBLIOGRAPHY

Alvera-Azcárate, A., A. Barth, and R. H. Weisberg, 2009: The Surface Circulation of the Caribbean Sea and the Gulf of Mexico as Inferred from Satellite Altimetry. *J. Phys. Oceanogr.*, **39** (3), 640-657, doi: http://dx.doi.org/10.1175/2008JPO3765.1.

Andrade-Canto, F., J. Sheinbaum, and L. Z. Sansón, 2013: A Lagrangian approach to the Loop Current eddy separation. *Nonlin. Processes Geophys.*, **20**, 85-96, doi: http://dx.doi.org/10.5194/npg-20-85-2013.

Behringer, D. W., R. L. Molinari, and J. F. Festa, 1977: The variability of anticyclonic current patterns in the Gulf of Mexico. *J. Geophys. Res.*, **82** (34), 5469-5476, doi: http://dx.doi.org/10.1029/JC082i034p05469.

Berens, P., 2009: CircStat: A Matlab toolbox for circular statistics. *J. Statistical Software*, **31** (10).

Casey, K. S., T. B. Brandon, P. Cornillon, and R. Evans, 2010: The Past, Present, and Future of the AVHRR Pathfinder SST Program. *Oceanography from Space: Revisited*, eds. V. Barale, J. F. R. Gower, and L. Alberotanza, Springer, doi: http://dx.doi.org/10.1007/978-90-481-8681-5_16.

Chang, Y.-L., L.-Y. Oey, 2010: Why Can Wind Delay the Shedding of Loop Current Eddies? *J. Phys. Oceanogr.*, **40** (11), 2481–2495, doi: http://dx.doi.org/10.1175/2010JPO4460.1.

Chang, Y.-L. and L.-Y. Oey, 2012: Why does the Loop Current tend to shed more eddies in the summer and winter? *Geophys. Res. Lett.,* **39** (5), L05605, doi: http://dx.doi.org/10.1029/2011GL050773.

Chang, Y.-L. and L.-Y. Oey, 2013a: Loop Current Growth and Eddy Shedding Using Models and Observations: Numerical Process Experiments and Satellite Altimetry Data. *J. Phys. Oceanogr.*, **43** (3), 669-689, doi: http://dx.doi.org/10.1175/JPO-D-12-0139.1.

Chang, Y.-L. and L.-Y. Oey, 2013b: Coupled Response of the Trade Wind, SST Gradient, and SST in the Caribbean Sea, and the Potential Impact on Loop Current's Interannual Variability. *J. Phys. Oceanogr.*, **43** (7), 1325-1344, doi: http://dx.doi.org/10.1175/JPO-D-12-0183.1.

Chassignet, E., D. Dukhovskoy, C. Hall, R. Leben, S. L. Morey, and R. Nedbor-Gross, 2013: Interannual variability of the Gulf of Mexico loop current and eddies from models and satellite observations, 2013 Gulf of Mexico Oil Spill and Ecosystem Science Conference, New Orleans.

Cheney, R. E., J. G. Marsh, and B. D. Beckley, 1983: Global mesoscale variability from collinear tracks of SEASAT altimeter data. *J. Geophys. Res.*, **88** (C7), 4343–4354, doi: http://dx.doi.org/10.1029/JC088iC07p04343.

Cochrane, J. D., 1965: The Yucatan Current. Oceanography and Meteorology of the Gulf of Mexico. Progress Report, June 1965, Dept. of Oceanography and Meteorology, Texas A. & M. University, Ref. (65-17T).

Coholan, P. D., J. W. Feeney, and S. P. Anderson, 2008: Life and Times of Eddy Zorro: A Review of the 2007 Gulf of Mexico Loop Current Activity. Offshore Technology Conference, 5-8 May 2008, Houston, Texas, USA, Paper OTC-19413-MS, 9 pp., doi: http://dx.doi.org/10.4043/19413-MS.

Evans-Hamilton, Inc., 1992: The Climatology and Simulation of Eddies, Final Report to Exxon Prod. Res. Co., 216 pp.

Forristall, G. Z., R. R. Leben, and C. A. Hall, 2010: A Statistical Hindcast and Forecast Model for the Loop Current. Offshore Technology Conference, 3-6 May 2010, Houston, Texas, USA, Paper OTC-20602-MS, 12 pp., doi: http://dx.doi.org/10.4043/20602-MS.

Forristall Ocean Engineering, 2009a: "Development of Synthetic Time Series for the Loop Current and Associated Eddies: Phase 3, Simulations Including Seasonality", prepared by George Z. Forristall (FOE), Robert R. Leben(UCB/CCAR), and Cody A. Hall (UCB/CCAR), Consultant Report to Climatology and Synthesis of Eddies Joint Industry Project (CASE/JIP), 58 pp. September, 2009.

Forristall Ocean Engineering, 2009b: "Appendix: Ancillary Data Analyses Supporting LoopSim Model Development", prepared by: Robert R. Leben(UCB/CCAR) and Cody A. Hall(UCB/CCAR), Consultant Report to Climatology and Synthesis of Eddies Joint Industry Project (CASE/JIP), 38 pp. September, 2009.

Fu, L.-L. and B. Holt, 1982: Seasat Views Oceans and Sea Ice with Synthetic-Aperture Radar. JPL Publication 81-120. Jet Propulsion Laboratory, California Institute of Technology, Pasadena, CA, pp. 52-53.

Glenn, S. M., G. Z. Forristall, P. Cornillon, and G. Milkowski, 1990: Observations of Gulf Stream ring 83-E and their interpretation using feature models. *J. Geophys. Res.*, **95** (C8), 13043–13063, doi: http://dx.doi.org/10.1029/JC095iC08p13043.

Goddard Space Flight Center, cited 2011: OceanColor web. [Available online at http://oceancolor.gsfc.nasa.gov.]

Gregg, W. W., M. E. Conkright, J. E. O'Reilly, F. S. Patt, M. H. Wang, J. A. Yoder, and N. W. Casey, 2002: NOAA-NASA Coastal Zone Color Scanner Reanalysis Effort. *Applied Optics*, **41** (9), 1615-1628 (2002), doi: http://dx.doi.org/10.1364/AO.41.001615.

Hamilton, P., K. Donohue, R. R. Leben, L.-Y. Oey, H. Quian, J. Sheinbaum, and D. R. Watts, 2014: Observations and Dynamics of the Loop Current. Technical Report. U.S. Dept. of the Interior, Bureau of Ocean Energy Management, Gulf of Mexico OCS Region, New Orleans, LA. OCS Study BOEM 2014-yyy. 409 pp.

Hong, B. G., W. Sturges, and A. J. Clarke, 2000: Sea Level on the U.S. East Coast: Decadal Variability Caused by Open Ocean Wind-Curl Forcing. *J. Phys. Oceanogr.*, **30** (8), 2088–2098, doi: http://dx.doi.org/10.1175/1520-0485(2000)030<2088:SLOTUS>2.0.CO;2.

Horizon Marine, Inc. (HMI), cited 2013: Loop Current eddies. [Available online at http://www.horizonmarine.com/loop_current_Eddies.php.]

Hurlburt, H. E. and J. D. Thompson, 1980: A Numerical Study of Loop Current Intrusions and Eddy Shedding. *J. Phys. Oceanogr.*, **10** (10), 1611–1651, doi: http://dx.doi.org/10.1175/1520-0485(1980)010<1611:ANSOLC>2.0.CO;2.

Hurlburt, H. E. and J. D. Thompson, 1982: The Dynamics of the Loop Current and Shed Eddies in a Numerical Model of the Gulf of Mexico, *Hydrodynamics of Semi-Enclosed Seas*, Elsevier Oceanography Series, ed. J. C. J. Nihoul, **34**, 243-297, Elsevier, ISSN 0422-9894, ISBN 9780444420770, doi: http://dx.doi.org/10.1016/S0422-9894(08)71247-9.

Jammalamadaka, S R. and A. SenGupta, 2001: *Topics in circular statistics*. Series on Multivariate Analysis, **5**, World Scientific, Singapore, 336 pp.

Kantha, L., J.-K. Choi, K. J. Schaudt, and C. K. Cooper, 2005: A regional Data-Assimilative Model for Operational Use in the Gulf of Mexico. *Circulation in the Gulf of Mexico: Observations and Models, Geophys. Monogr.*, eds. W. Sturges and A. Lugo- Fernández, **161**, Eos, Trans. Amer. Geophys. Union, Washington, D. C., doi: http://dx.doi.org/10.1029/161GM14.

Kim, K.-Y. and Q. Wu, 1999: A Comparison Study of EOF Techniques: Analysis of Nonstationary Data with Periodic Statistics. *J. Climate*, **12** (1), 185–199. doi: http://dx.doi.org/10.1175/1520-0442-12.1.185.

Kirwan Jr., A. D., G. McNally, and J. Coehlo, 1976: Gulf Stream Kinematics Inferred from a Satellite-Tracked Drifter. *J. Phys. Oceanogr.*, **6** (5), 750–755, doi: http://dx.doi.org/10.1175/1520-0485(1976)006<0750:GSKIFA>2.0.CO;2.

Kirwan Jr., A. D., W. J. Merrell Jr., J. K. Lewis, and R. E. Whitaker, 1984: Lagrangian observations of an anticyclonic ring in the western Gulf of Mexico, *J. Geophys. Res.*, **89** (C3), 3417–3424, doi: http://dx.doi.org/10.1029/JC089iC03p03417.

Koblinsky, C. J., B. D. Beckley, R. D. Ray, Y.-M. Wang , L. Tsaoussi, A. Brenner, and R. Williamson, 1998: NASA Ocean Altimeter Pathfinder Project. Report I: Data Processing Handbook. NASA/TM-1998-208605.

Kramer, H. J., 2002: *Observation of the Earth and Its Environment: Survey of Missions and Sensors, 4th ed*. Springer-Verlag, 1510 pp.

Leben, R. R., G. H. Born, and B. R. Engebreth, 2002: Operational Altimeter Data Processing for Mesoscale Monitoring. *Marine Geodesy*, **25** (1-2), 3-18, doi: http://dx.doi.org/10.1080/014904102753516697.

Leben, R. R., 2005: Altimeter-Derived Loop Current Metrics. *Circulation in the Gulf of Mexico: Observations and Models, Geophys. Monogr.*, eds. W. Sturges and A. Lugo- Fernández, **161**, Eos, Trans. Amer. Geophys. Union, Washington, D. C., doi: http://dx.doi.org/10.1029/161GM15.

Leben, R. R. and C. A. Hall, 2010: A 30-Year Record of Loop Current Eddy Separation Events, Eos, Trans. Amer. Geophys. Union, **91** (26), Ocean Sci. Meet. Suppl., Abstract PO45E-02.

Legeckis, R. 1976. Present and planned satellite observations of the Gulf of Mexico and the Caribbean Sea (abstract). Progress in Marine Research in the Caribbean and Adjacent Regions, CICAR-II Symposium, ed. H. B. Stewart, Jr., 12-16 July 1976, Caracas, Venezuela. pp. 239.

Leipper, D. F., 1970: A sequence of current patterns in the Gulf of Mexico. *J. Geophys. Res.*, **75** (3), 637-657.

Li, J. and A. J. Clarke, 2005: Interannual flow along the northern coast of the Gulf of Mexico, *J. Geophys. Res.*, **110** (C11). C11002, doi: http://dx.doi.org/10.1029/2004JC002606.

Lindo-Atichati, D., F. Bringas, and G. Goni, 2013: Loop Current excursions and ring detachments during 1993-2009. *Int. J. of Remote Sens.*, **34** (14), 5042-5053, doi: http://dx.doi.org/10.1080/01431161.2013.787504.

Maul, G. A., 1975: An evaluation of the use of the earth resources technology satellite for observing ocean current boundaries in the Gulf Stream system. Tech. Rep. ERL 335 AOML-18:125. NOAA, NWS.

Maul, G. A., 1977: The annual cycle of the Gulf Loop Current Part I: Observations during a one-year time series. *J. Mar. Res.*, **35** (1), 29-47.

Maul, G. A., P. W. deWitt, A. Yanaway, and S. R. Baig, 1978: Geostationary satellite observations of Gulf Stream meanders: Infrared measurements and time series analysis. *J. Geophys. Res.*, **83** (C12), 6123–6135, doi: http://dx.doi.org/10.1029/JC083iC12p06123.

Maul, G. A., F. Williams, M. Roffer, and F. M. Sousa, 1984: Remotely Sensed Oceanographic Patterns and Variability of Bluefin Tuna Catch in the Gulf of Mexico. *Oceanologica Acta*, **7** (4), 469-479.

Maul, G. A. and K. Hanson, 1991: Interannual coherence between North Atlantic atmospheric surface pressure and composite southern U.S.A. sea level. *Geophys. Res. Lett.*, **18** (4), 653–656, doi: http://dx.doi.org/10.1029/91GL00141.

Maul, G. A. and F. M. Vukovich, 1993: The Relationship between Variations in the Gulf of Mexico Loop Current and Straits of Florida Volume Transport. *J. Phys. Oceanogr.*, **23** (5), 785–796, doi: http://dx.doi.org/10.1175/1520-0485(1993)023<0785:TRBVIT>2.0.CO;2.

Molinari, R. L., S. Baig, D. W. Behringer, G. A. Maul, and R. Legeckis, 1977: Winter Intrusions of the Loop Current. *Science*, **198** (4316), 505-507, doi: http://dx.doi.org/10.1126/science.198.4316.505.

Müller-Karger, F. E., J. J. Walsh, R. H. Evans, and M. B. Meyers. 1991: On the seasonal phytoplankton concentration and sea surface temperature cycles of the Gulf of Mexico as determined by satellites. *J. Geophys. Res.*, **96** (C7). 12645-12665, doi: http://dx.doi.org/10.1029/91JC00787.

National Oceanographic Data Center, cited 2011: 4 km AVHRR Pathfinder project. [Available online at http://www.nodc.noaa.gov/SatelliteData/pathfinder4km.]

Nof, D. 1981. On the β-Induced Movement of Isolated Baroclinic Eddies. *J. Phys. Oceanogr.*, **11** (12), 1662-1672, doi: http://dx.doi.org/10.1175/1520-0485(1981)011<1662:OTIMOI>2.0.CO;2.

Nowlin, W. D., Jr., A. E. Jochens, S. F. DiMarco, R. O. Reid, and M. K. Howard, 2001: Deepwater physical oceanography reanalysis and synthesis of historical data, synthesis report. U.S. Dept. of the Interior, Minerals Management Service, Gulf of Mexico OCS Region, New Orleans, LA. OCS Study MMS 2001-064. 530 pp.

Ott, R. L. and M. Longnecker, 2001: *An Introduction to Statistical Methods and Data Analysis, 5th ed*. Duxbury, 1152 pp.

Reid, R. O., 1972: A Simple Dynamic Model of the Loop Current. *Contributions on the Physical Oceanography of the Gulf of Mexico*. Texas A. & M. University Oceanographic Studies, eds. L. R. A. Capurro and J. L. Reid, **2**, Gulf Publishing Co., Houston, TX, pp. 157-159.

Rio, M.-H. and F. Hernandez, 2004: A mean dynamic topography computed over the world ocean from altimetry, in situ measurements, and a geoid model. *J. Geophys. Res.*, **109** (C12), C12032, doi: http://dx.doi.org/10.1029/2003JC002226.

Rio, M.-H. and G. Larnicol, 2010: The CNES/CLS mean dynamic topography. Proceedings of the Ocean Surface Topography Science Team Meeting, October 2010, Lisbon, Portugal.

Rousset, C. and L. M. Beal, 2010: Observations of the Florida and Yucatan Currents from a Caribbean Cruise Ship. *J. Phys. Oceanogr.*, **40** (7), 1575–1581, doi: http://dx.doi.org/10.1175/2010JPO4447.1.

Sandwell, D. T. and D. C. McAdoo, 1988: Marine gravity of the southern ocean and Antarctic margin from Geosat. *J. Geophys. Res.*, **93** (B9), 10389–10396, doi: http://dx.doi.org/10.1029/JB093iB09p10389.

Saraceno, M., P. T. Strub, and P. M. Kosro, 2008: Estimates of sea surface height and near-surface alongshore coastal currents from combinations of altimeters and tide gauges. *J. Geophys. Res.*, **113** (C11), C11013, doi: http://dx.doi.org/10.1029/2008JC004756.

Schnapf, A., 1981: TIROS-N – Operational Environmental Satellite of the 80's. *J. Spacecraft and Rockets*, **18** (2), 172-177, doi: http://dx.doi.org/10.2514/3.57800.

Sturges, W., 1992: The Spectrum of Loop Current Variability from Gappy Data. *J. Phys. Oceanogr.*, **22** (11), 1245-1256, doi: http://dx.doi.org/10.1175/1520-0485(1992)022<1245:TSOLCV>2.0.CO;2.

Sturges, W., 1993: The annual cycle of the western boundary current in the Gulf of Mexico. *J. Geophys. Res.*, **98** (C10), 18053-18068, doi: http://dx.doi.org/10.1029/93JC01730.

Sturges, W., 1994: The Frequency of Ring Separations from the Loop Current. *J. Phys. Oceanogr.*, **24** (7), 1647-1651, doi: http://dx.doi.org/10.1175/1520-0485(1994)024<1647:TFORSF>2.0.CO;2.

Sturges, W. and J. C. Evans, 1983. On the Variability of the Loop Current in the Gulf of Mexico. *J. Mar. Res.*, **41** (4), 639-653, doi: http://dx.doi.org/10.1357/002224083788520487.

Sturges, W. and R. R. Leben, 2000: Frequency of Ring Separations from the Loop Current in the Gulf of Mexico: A Revised Estimate. *J. Phys. Oceanogr.*, **30** (7), 1814-1819, doi: http://dx.doi.org/10.1175/1520-0485(2000)030<1814:FORSFT>2.0.CO;2.

Trenberth, K. E., 1984: Signal Versus Noise in the Southern Oscillation. *Mon. Weather Rev.*, **112** (2), 326–332, doi: http://dx.doi.org/10.1175/1520-0493(1984)112<0326:SVNITS>2.0.CO;2.

Vukovich, F. M., B. W. Crissman, M. Bushnell, W. J. King, 1978: Sea-surface temperature variability analysis of potential OTEC sites in the eastern Gulf of Mexico utilizing satellite data: Final Report, Research Triangle Park, N.C., Prepared for the United States Department of Energy Division of Solar Energy, DOE Contract No EG-77-C-05-5444. 153 pp.

Vukovich, F. M., B. W. Crissman, M. Bushnell, and W. J. King, 1979: Some aspects of the oceanography of the Gulf of Mexico using satellite and in situ data. *J. Geophys. Res.*, **84** (C12), 7749–7768, doi: http://dx.doi.org/10.1029/JC084iC12p07749.

Vukovich, F. M. and G. A. Maul, 1985: Cyclonic Eddies in the Eastern Gulf of Mexico. *J. Phys. Oceanogr.*, **15** (1), 105-117, doi: http://dx.doi.org/10.1175/1520-0485(1985)015<0105:CEITEG>2.0.CO;2.

Vukovich, F. M., 1986: Aspects of the Behavior of Cold Perturbations in the Eastern Gulf of Mexico: A Case Study. *J. Phys. Oceanogr.*, **16** (1), 175-188, doi: http://dx.doi.org/10.1175/1520-0485(1986)016<0175:AOTBOC>2.0.CO;2.

Vukovich, F. M. and B. W. Crissman, 1986: Aspects of warm rings in the Gulf of Mexico. *J. Geophys. Res.*, **91** (C2), 2645-2660, doi: http://dx.doi.org/10.1029/JC091iC02p02645.

Vukovich, F. M., 1988: Loop Current boundary variations. *J. Geophys. Res.*, **93** (C12), 15585–15591, doi: http://dx.doi.org/10.1029/JC093iC12p15585.

Vukovich, F. M., 2007: Climatology of Ocean Features in the Gulf of Mexico Using Satellite Remote Sensing Data. *J. Phys. Oceanogr.*, **37** (3), 689-707, doi: http://dx.doi.org/10.1175/JPO2989.1.

Vukovich, F. M., 2012: Changes in the Loop Current's Eddy Shedding in the Period 2001-2010. *International J. Oceanogr*, **2012**, 439042, 18 pp., doi: http://dx.doi.org/10.1155/2012/439042.